Development and Control of a 3-axis Stabilised Platform

by

Adolf Friedrich Ludwig Bredenkamp

Thesis presented in partial fulfilment of the requirements for the degree of Master of Science in Electronic Engineering at the University of Stellenbosch

Department of Electrical and Electronic Engineering
University of Stellenbosch
Private Bag X1, 7602 Matieland, South Africa

Supervisor: Prof W.H. Steyn

March 2007

Declaration

I, the undersigned, hereby declare that the work contained in this thesis is my own original work and that I have not previously in its entirety or in part submitted it at any university for a degree.

Signature: .....

A.F.L. Bredenkamp

Date: .....

Abstract

The successful control of a three-degree-of-freedom gyroscope is presented for the application of steering and stabilising a platform mounted underneath an airship. The end goal is to stabilise a camera for earth observation purposes.

The development of the necessary electronics, sensors and actuators along with the hardware and software to interface these components are presented. This include DC drives, torque control systems for the gimbal motors and a speed control system for the gyroscope as well as platform angle and angular rate sensors.

A mathematical model for the gyroscope, based on Euler's equations of motion, is presented. Non-linear simulations are performed and compared to measurements of the plant's behaviour to step torque commands to determine the parameters of the gyroscope. Pole placement and LQR optimal control methods are considered in the design of a MIMO controller to steer the platform in the elevation plane, along with a PI controller to steer the platform in the azimuth plane. Ground tests display the success of the steering controllers.

Opsomming

Die suksesvolle beheer van 'n giroskoop met drie grade van vryheid, om te dien as 'n stabilisasie platform gemonteer onderaan 'n lugskip, word aangetoon. Die eindoel is om 'n kamera te stuur en te stabiliseer vir aardwaarnemings doeleindes.

Die nodige elektronika, aktueerders en sensore word ontwikkel, sowel as die hardeware en sagteware wat die onderskeie komponente aan mekaar koppel. Dit sluit in GS motor aandryfelektronika, wringkrag- en spoedbeheerstelsels asook platform hoek- en hoeksnelheidsensore.

'n Wiskundige giroskoopmodel, gebaseer op Euler se wette, word aangebied. Nie-lineêre simulasies word uitgevoer en vergelyk met gemete trapweergawes van die aanleg om die nodige parameters van die giroskoop te bepaal. Beheerstrategieë gebaseer op die metodes van poolplasing en LQR optimale beheer word ondersoek om die platform te stuur in die elevasievlak. 'n PI beheerder word ontwerp om die platform te stuur in die asimutvlak. Grondtoetsresultate toon die suksesvolle beheer van die platform aan.

Acknowledgements

I would like to thank:

- Professor W.H. Steyn, for his guidance throughout this project.
- Sunspace for funding the project.
- Jackie Blom and the rest of the staff at Central Mechanical Services for seeing to the development of the mechanical aspects of this project.
- My family for their love and support. Especially my parents for giving me much more than an education. Your love and support will always accompany me.
- My fellow students in the ESL for your input and contribution to countless memorable moments.
- Nicola van Wilgen, for support and motivation.
- The Almighty God, Creator of all knowledge.

Contents

List of Figures

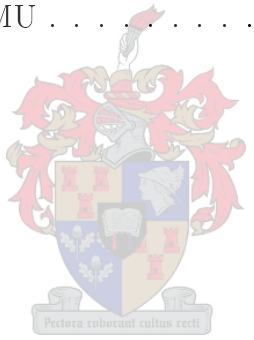

List of Tables

Nomenclature

Symbols

Az	Boresight azimuth angle
El	Boresight elevation angle
ϕ	Euler roll angle
θ	Euler pitch angle
ψ	Euler yaw angle
$\dot{\phi}$	Euler roll rate
$\dot{\theta}$	Euler pitch rate
$\dot{\psi}$	Euler yaw rate
$\mathbf{B}$	Camera boresight vector
$\mathbf{A_{321}}$	Direction cosine matrix for Euler 3-2-1 rotation sequence
$\boldsymbol{\omega}$	Angular velocity vector
$\mathbf{I}$	Moment of inertia tensor
$\mathbf{N_m}$	Motor torque vector
$\mathbf{N_w}$	Frictional torque vector
$\mathbf{N}$	Torque vector
$\mathbf{H}$	Angular momentum vector
h_0	Flywheel angular momentum
V_{ref}	Motor torque reference voltage
V_e	Torque PI controller input voltage
V_{in}	Pulse width modulator input voltage
V_{I_sense}	Voltage measured across current sense resistor
V_{speed}	Flywheel velocity reference voltage
V_{tacho}	Tachometer output voltage
k_m	DC motor torque constant
k_w	Coefficient of viscous friction
τ	Time constant of first order system

C	Calibration matrix
$\mathcal{C}$	Controllability matrix
ω_s	Sampling frequency
ω_b	Closed-loop bandwidth
ω_r	Open-loop system resonant frequency
ω_n	Natural frequency
ζ	Damping factor
$\mathcal{Z}$	Z-transform operator
z	Discrete time z-transform variable
s	Laplace transform variable

Acronyms

A/D	Analogue-to-digital
AHRS	Attitude heading reference system
ASCII	American standard code for information interchange
CMS	Central mechanical services
CPU	Central processing unit
DC	Direct current
D/A	Digital-to-analogue
DOF	Degree-of-freedom
IMU	Inertial measurement unit
LQG	Linear quadratic gaussian regulator
LQR	Linear quadratic regulator
MIMO	Multi input multi output
OBC	On-board computer
PCA	Programmable counter array
PI	Proportional Integral
PWM	Pulse width modulation
RF	Radio frequency
RMS	Root mean square
SEAIP	Stabilized electro-optical airborne instrumentation platform
SISO	Single input single output
UART	Universal asynchronous receiver transmitter
UAV	Unmanned aerial vehicle
ZOH	Zero order hold

Subscripts

I	Inertial axes
B	Airship body axes
G	Gimbal axes
P	Platform axes
1	Gimbal axis 1
2	Gimbal axis 2
3	Gimbal axis 3
f	Flywheel

Chapter 1

Introduction

1.1 Motivation

1.1.1 Aerial Photography and Video

The first aerial photograph was taken by balloonist Gaspard-Félix Tournachon in 1858, also known as Nadar, his pseudonym. Fig. 1.1 shows a photograph of Paris taken by Nadar in 1868 [20]. Aerial photography and video as a remote sensing tool have since enabled man to gather information beyond the range of human vision. It provides the necessary spatial and geographical information for specific applications that cannot easily be acquired without a bird's eye view of an area. Some of the fields that vastly benefit from aerial photography and video are law enforcement, disaster control, cartography, agriculture and environmental studies [21]. The list is not at all exhaustive.

1.1.2 Background

To obtain a stable image from a camera mounted on an aerial vehicle, it is essential to decouple the movement of the vehicle from the camera. Dynamic separation from the vehicle movement can be obtained by mounting the camera on a platform that maintains a constant pointing reference in inertial space. This is achieved through a system of sensors, which measure the orientation of the platform with regard to inertial space, and actuators, which rotate the platform to compensate for vehicle movement. Several platforms have been developed for the stabilisation of cameras for use in earth observation. Table 1.1 lists some of the specified capabilities of commercially available stabilising platforms (refer to Chapter 7 for a

Figure 1.1: An aerial photograph of Paris taken in 1868 by Nadar [20]

comparison with the platform developed in this thesis). These platforms are mainly developed for use on helicopters and unmanned aerial vehicles (UAV's) and retail up to ZAR 700 000 [25].

Table 1.1: Capabilities of commercially available platforms

Platform Manufacturer	Maximum rotation rate	Stabilisation bandwidth	Field of view	
			Az/El	Pitch/Roll
Tenix UAV stabilised gimbal	Not specified	10Hz		±20°/±90°
Floatograph SkyDoc	150°/s	5Hz	±360°/ +20°,−110°	
iMAR iICSC-DL	150°/s	80Hz	±360°/ +80°,−200°	
Southern Research Institute SEAIP	30°/s	Not specified	±180°/ +30°,−110°	

1.2 Objectives

The goal of this project is to develop a cost-effective stabilised platform on which a camera can be mounted for earth observation purposes. The platform will be

developed specifically for use on an airship. Airships are superb candidates for performing long-endurance surveillance[1].

The fundamental specifications for the stabilised platform are:

- The platform must be able to maintain a stable directional pointing reference and not be affected by the airship's rotations.
- A user must be able to steer the pointing reference of the platform smoothly.

This means that the image obtained from the camera on-board the platform should under all operating conditions be free of jitter as perceived by the operator, providing an accurate representation of the area under surveillance and enabling the operator to easily analyse and interpret the sensed data.

1.3 Principles

A device which has proved most suitable for the instrumentation of a reference direction is the gyroscope [8]. Foucault defined the gyroscope in 1852 as *a device exhibiting strong angular momentum* [8]. Scarborough defined the gyroscope more specifically as *a mechanical device the essential part of which is a flywheel*[2] *having a heavy rim and so mounted, that its axis of rotation can turn in any direction about a fixed point on that axis* [6]. The stabilised platform developed in this project is based on the principle of gyroscopic stability. A three-degree-of-freedom gyroscope is illustrated in Fig. 1.2. It has three gimbals that allows the spin axis to have three degrees of rotational freedom about its centre of mass. A general discussion of some of the properties of the gyroscope, based on theory from [6] and [8], follows.

Fig. 1.3 illustrates the basic law of motion of a practical gyroscope. The angular velocity of a flywheel creates an angular momentum vector through its axis of spin. In the absence of an applied torque, an angular momentum vector maintains a fixed orientation in inertial space, thereby providing a directional reference. This angular momentum vector can be steered in a known fashion by applying a calibrated torque to the flywheel. The forced motion of a gyroscope is called *precession* and arises in obedience to the fundamental relation [6]

$$\frac{d\mathbf{H}}{dt} = \mathbf{N}, \tag{1.1}$$

[1] The benefits of airships are stated in detail in [12].

[2] A flywheel is a device that spins at a constant angular velocity.

Figure 1.2: A three-degree-of-freedom gyroscope [26]

where **H** is the angular momentum and **N** is the applied torque.

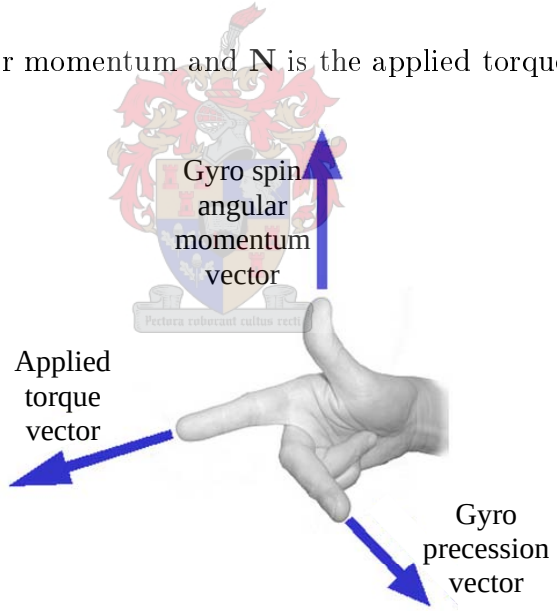

Figure 1.3: Representation of the basic law of motion of the gyroscope

It is shown in [6] that for a perfect gyroscope, the velocity of precession is directly proportional to the magnitude of the external applied torque and inversely proportional to the velocity of spin and moment of inertia in the spin axis of the flywheel. Consider the special case of Fig. 1.4, where the axis system is fixed in the spinning element and the moment of inertia in the x-axis is much greater than the

moment of inertia in the y-axis and z-axis. If an external torque $\mathbf{T}$ is applied to a gyroscope exerting an angular momentum $\mathbf{h}$, the rate of precession, Ω, is

$$\mathbf{\Omega} = \frac{\mathbf{T}}{\mathbf{h}}. \tag{1.2}$$

Here the torque is always applied in the y-axis and the precession is always in the z-axis.

Furthermore, the motion of a gyroscope under external disturbances is stable and periodic of nature. The periodic oscillations are referred to as nutation and must be damped for the gyroscope to be of practical value [8]. The higher the velocity of the flywheel, the smaller the amplitude and the higher the frequency of the simple harmonic oscillations. The frequency of oscillation was found to be

$$\omega = \frac{C\dot{\psi}}{2\pi A}, \tag{1.3}$$

where C is the moment of inertia of the flywheel in its spin axis, $\dot{\psi}$ is the angular rate of the flywheel, and A is the moment of inertia of the axis perpendicular to the spin axis of the flywheel.

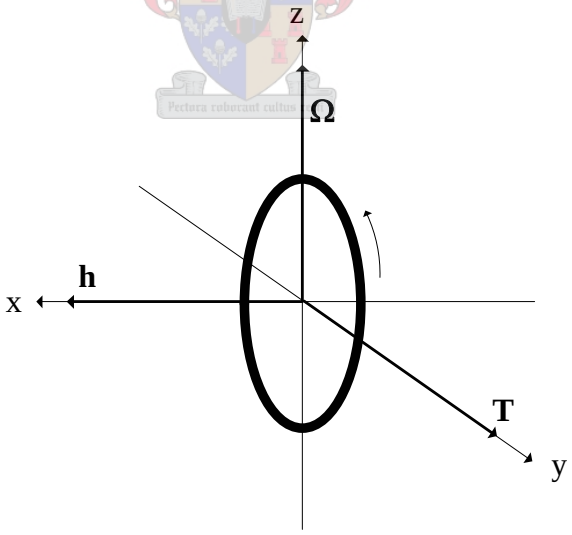

Figure 1.4: Gyroscopic precession under applied external torques

It can thus be seen that a trade-off, dependent on the flywheel angular momentum, exists between the actuation power required to achieve a given rate of precession and control effort required to ensure smooth precessional motion. The

higher the angular momentum generated by the flywheel, the smaller the oscillatory modes of the gyroscope but the higher the required torque to achieve a given rate of precession.

In the chapters that follow, a gyroscope for use as a stabilised platform will be developed and control over the gyroscope will be attempted.

1.4 Overview of Thesis

The relevant coordinate systems are defined in Chapter 2 along with a derivation of the equations of motion of the gyroscope. Chapter 3 details the development of the physical system in terms of hardware and software. Chapter 4 provides insight into practical gyroscopic motion with open loop measurements and simulations. The parameters of the physical system used in the model developed in Chapter 2 are also determined. In Chapter 5, the control methodology is presented, along with the controller design details. Chapter 6 presents the practical results of the controllers developed in this project. Chapter 7 provides a summary and recommendations for future work.

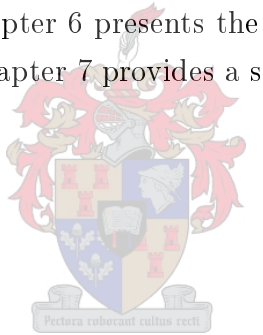

Chapter 2

Theory and Model Development

This chapter begins by defining the relevant coordinate systems along with a method to transform vectors from one coordinate system to another. The derivation of Euler's equations of motion is then presented, which lead to a mathematical model of the stabilised platform.

2.1 Coordinate Systems Definitions

In order to describe and control the orientation of the stabilised platform, four sets of coordinate systems will be defined, namely:

- The inertial axis system
- The airship body axis system
- The platform axis system
- The gimbal axis system

2.1.1 Inertial Axes

An inertial reference frame is a set of axes which remains constant with time. The attitude of a body can uniquely be determined by evaluating the orientation of the body frame relative to the inertial frame. Within the inertial reference frame, Newton's laws are valid [8].

For the problem at hand, the earth can be considered flat and non-rotating. These are valid assumptions since the airship will be rotating much faster than the

earth and the translational motion of the airship will be small with respect to a fixed point on the earth. The inertial axis system, $O_I - X_I Y_I Z_I$, is then defined as a set of earth-fixed, right-hand orthogonal axes oriented north for the positive X_I-axis, east for the positive Y_I-axis and down for the positive Z_I-axis.

2.1.2 Airship Body Axes

The airship body axis, $O_B - X_B Y_B Z_B$, as defined in [12] and illustrated in Fig. 2.1, is a fixed right-hand orthogonal coordinate system with the positive X_B-axis in the direction of the nose of the airship, the positive Y_B-axis to the right of the positive X_B-axis and the Z_B-axis orthogonally downward from the $X_B Y_B$-plane. The origin, O_B, is at the centre of mass of the airship.

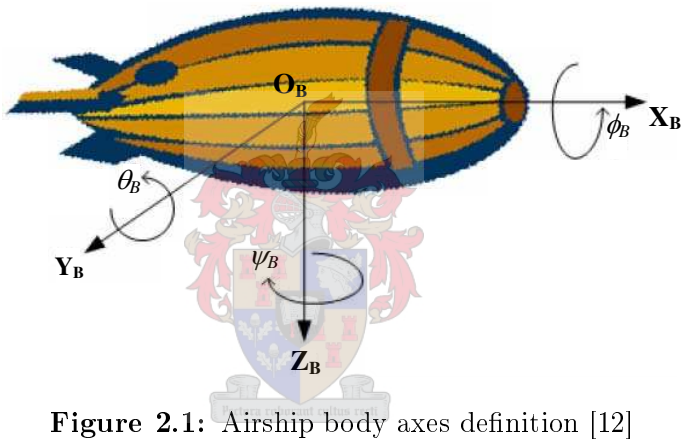

Figure 2.1: Airship body axes definition [12]

The airship body axis system is fixed to the body of the airship and changes with respect to inertial space as the orientation of the airship changes. The attitude of the airship body axis system is described in terms of the angles ϕ_B, θ_B and ψ_B, which are measured by an AHRS developed by Bijker [12] in a separate project.

For the development of the steering controllers of the platform, the base of the airship will be assumed to be inertially aligned. This assumption is necessary since the AHRS measuring the airship's rotations will only be available for integration with this project at a later stage. In reality, the airship's roll and pitch angles are small with respect to inertial space, while the Z_B-axis and the gimbal 3-axis (see Section 2.1.4) remain coincident with a change in the airship's yaw angle, which is unconstrained. Thus, for the development of the theory in the remainder of this chapter, we will assume that the airship body axis system is aligned with the inertial

axis system. In practice, a human in the loop will issue the steering commands and will be able to easily compensate for this assumption, since an airship's rotations are slow [12].

2.1.3 Platform Axes

The platform axis system is defined as a right-hand orthogonal coordinate system, with origin at the intersection of the gimbal axis of rotation and the spin axis of the gyroscope. With reference to Fig. 2.2, the X_P-axis is defined as the axis of rotation of the inner gimbal of the gyroscope, the Y_P-axis is to the right of the X_P-axis in the plane of rotation of the flywheel and the Z_P-axis is pointing orthogonally downward from the $X_P Y_P$-plane. The Z_P-axis is now aligned with the angular momentum vector generated by the flywheel and with the boresight of the camera. This coordinate system is fixed in the stabilisation plane.

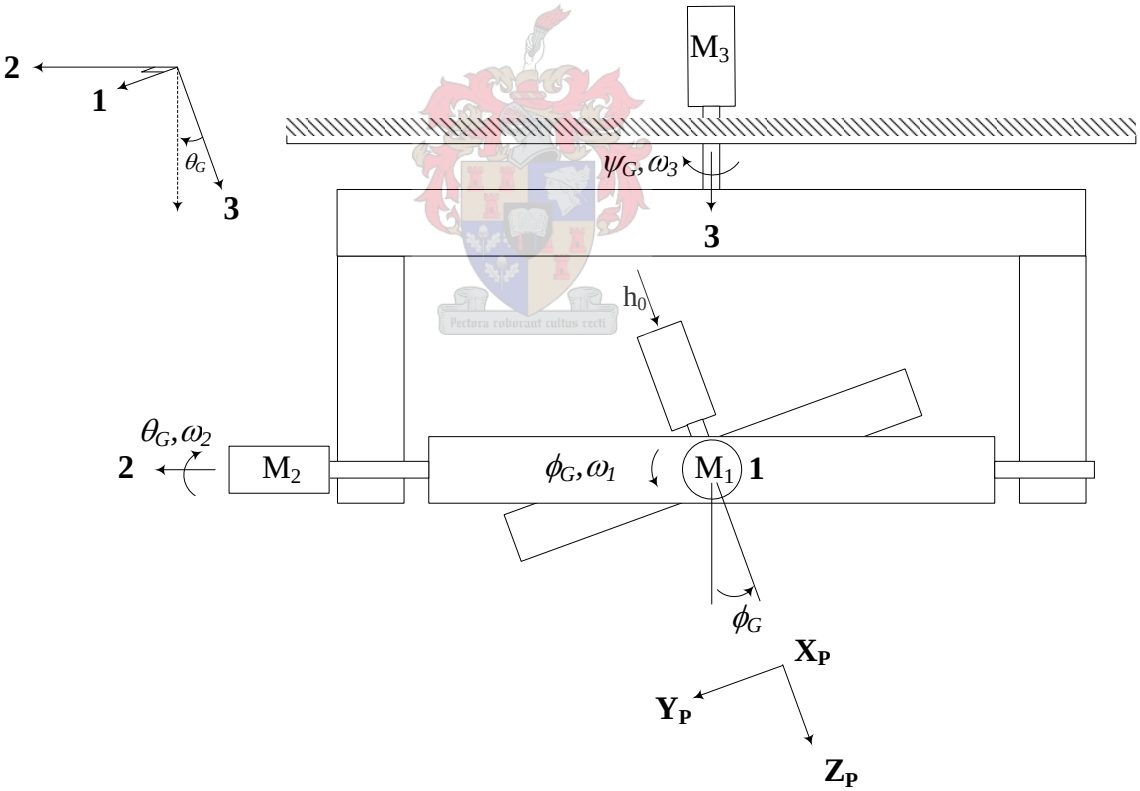

Figure 2.2: Gimbal axes and platform axes definitions

The attitude of the platform axis system with regard to inertial space is specified by the angles ϕ_P, θ_P and ψ_P and with regard to the airship body axis by the angles

ϕ_G, θ_G and ψ_G.

2.1.4 Gimbal Axes

It is necessary to define a convenient set of axes wherein the dynamic equations of motion of the gyroscope can be evaluated. Two right-hand orthogonal coordinate systems will be defined using the three axes of gimbal rotation, **1**, **2** and **3**, illustrated in Fig. 2.2 with **1** towards the reader. The 1-axis is defined as the axis about which the inner gimbal rotates, the 2-axis is defined as the axis about which the middle gimbal rotates and the 3-axis is defined as the axis about which the outer gimbal rotates.

The orthogonal orientation of the 3-axis with regard to the 12-plane disappears as the middle gimbal rotates through an angle of θ_G. We therefore define $\mathbf{1}'$ perpendicular to the 23-plane and $\mathbf{3}''$ perpendicular to the 12-plane in order to form the two orthogonal coordinate systems $O-123''$ and $O-1'23$ as illustrated in Fig. 2.3.

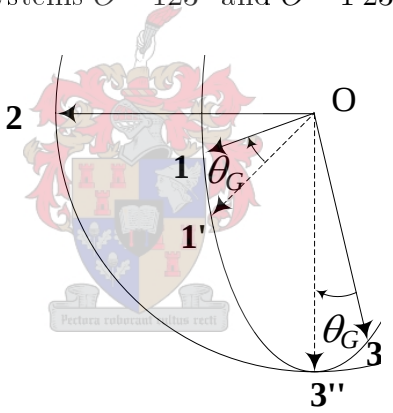

Figure 2.3: Orthogonal gimbal rotation axes definitions

The gyroscope is connected to inertial space through the airship. The 3-axis is fixed to the airship body axes and is always aligned with the Z_B-axis. The orientation of the gimbals relative to the airship body axis is specified by the angles ϕ_G, θ_G and ψ_G.

2.2 Azimuth and Elevation Angles

An intuitive representation of the orientation of the platform is given by evaluating the azimuth and elevation angles of the camera boresight. The boresight vector is

defined as

$$\mathbf{B_P} = \begin{bmatrix} 0 & 0 & 1 \end{bmatrix} \begin{bmatrix} \mathbf{X_P} \\ \mathbf{Y_P} \\ \mathbf{Z_P} \end{bmatrix} \tag{2.1}$$

and is denoted in the inertial axis system as

$$\mathbf{B_I} = \begin{bmatrix} B_{X_I} & B_{Y_I} & B_{Z_I} \end{bmatrix} \begin{bmatrix} \mathbf{X_I} \\ \mathbf{Y_I} \\ \mathbf{Z_I} \end{bmatrix}. \tag{2.2}$$

Referring to Fig. 2.4, the azimuth angle is defined as the angle between the positive X_I-axis and the projection of the boresight vector onto the X_IY_I-plane. The elevation angle is defined as the angle between the X_IY_I-plane and the boresight vector. The angles are calculated mathematically as

$$Az = \arctan\left(\frac{B_{Y_I}}{B_{X_I}}\right) \tag{2.3}$$

and

$$El = \arctan\left(\frac{B_{Z_I}}{\sqrt{B_{X_I}^2 + B_{Y_I}^2}}\right). \tag{2.4}$$

The sign of the boresight components has to be taken into account to obtain the angles in the correct quadrant.

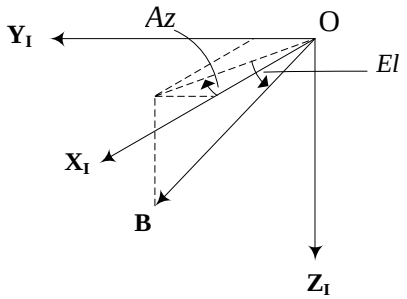

Figure 2.4: Boresight azimuth and elevation angle definitions

2.3 Euler Rotations

The orientation of a body rotating about a fixed point is best described using three angles, ϕ, θ and ψ, called Euler angles. Using the Euler angles, a coordinate transformation that maps vectors in one reference frame to another can be defined [7]. This is done by three consecutive rotations. The Euler 3-2-1 rotation sequence will be used, since it can be instrumented physically by three gimbals as was done for the stabilised platform in this project. The gimbal angles, ϕ_G, θ_G and ψ_G, are simply the Euler angles for the platform axis system when the airship body axis system is aligned with the inertial axis system.

Referring to Fig. 2.5, the transformation involves rotating $O - X_I Y_I Z_I$ through an angle ψ_G about the Z_I-axis to form $O - X_I' Y_I' Z_I'$. The second rotation involves rotating $O - X_I' Y_I' Z_I'$ through an angle θ_G about the Y_I'-axis to form $O - X_I'' Y_I'' Z_I''$. Finally, $O - X_I'' Y_I'' Z_I''$ is rotated through an angle ϕ_G about the X_I''-axis to form $O - X_I''' Y_I''' Z_I'''$, which is aligned with the platform axis system $O - X_P Y_P Z_P$. Beginning with a vector $\mathbf{V_I}$ coordinate in $O - X_I Y_I Z_I$, the transformation to $\mathbf{V_{I'''}} \equiv \mathbf{V_P}$ coordinated in $O - X_P Y_P Z_P$, can be described mathematically as

$$\mathbf{V_{I'}} = \mathbf{A_3}(\psi_G)\mathbf{V_I} \tag{2.5}$$

$$\mathbf{V_{I''}} = \mathbf{A_2}(\theta_G)\mathbf{V_{I'}} \tag{2.6}$$

$$\mathbf{V_{I'''}} = \mathbf{A_1}(\phi_G)\mathbf{V_{I''}}, \tag{2.7}$$

where

$$\mathbf{A_3}(\psi_G) = \begin{bmatrix} \cos\psi_G & \sin\psi_G & 0 \\ -\sin\psi_G & \cos\psi_G & 0 \\ 0 & 0 & 1 \end{bmatrix} \tag{2.8}$$

$$\mathbf{A_2}(\theta_G) = \begin{bmatrix} \cos\theta_G & 0 & -\sin\theta_G \\ 0 & 1 & 0 \\ \sin\theta_G & 0 & \cos\theta_G \end{bmatrix} \tag{2.9}$$

$$\mathbf{A_1}(\phi_G) = \begin{bmatrix} 1 & 0 & 0 \\ 0 & \cos\phi_G & \sin\phi_G \\ 0 & -\sin\phi_G & \cos\phi_G \end{bmatrix}. \tag{2.10}$$

Combining equation (2.8) to (2.10) yield the direction cosine matrix (DCM), given

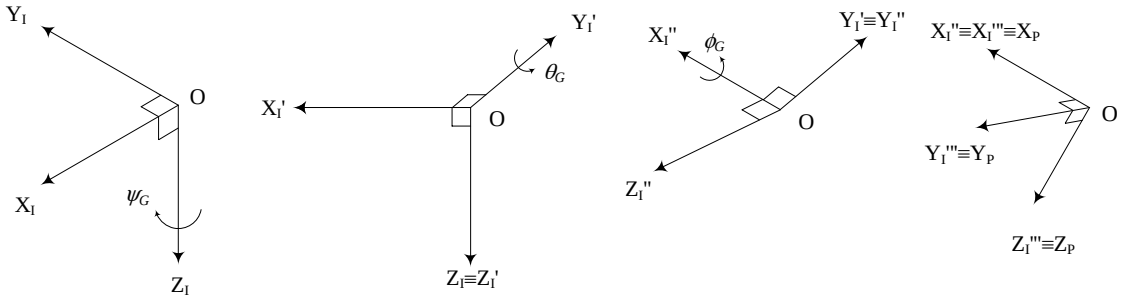

Figure 2.5: The Euler 3-2-1 rotation sequence

by

$$\mathbf{A_{321}}(\phi_G, \theta_G, \psi_G) = \mathbf{A_1}(\phi_G)\mathbf{A_2}(\theta_G)\mathbf{A_3}(\psi_G)$$

$$= \begin{bmatrix} \cos\theta_G \cos\psi_G & \cos\theta_G \sin\psi_G & -\sin\theta_G \\ -\cos\theta_G \sin\psi_G + \sin\phi_G \sin\theta_G \cos\psi_G & \cos\phi_G \cos\psi_G + \sin\phi_G \sin\theta_G \sin\psi_G & \sin\phi_G \cos\theta_G \\ \sin\phi_G \sin\psi_G + \cos\phi_G \sin\theta_G \cos\psi_G & -\sin\phi_G \cos\psi_G + \cos\phi_G \sin\theta_G \cos\psi_G & \cos\phi_G \cos\theta_G \end{bmatrix}. \tag{2.11}$$

A vector coordinated in the inertial axis system, $O - X_I Y_I Z_I$, can now be transformed to the platform axis system, $O - X_P Y_P Z_P$, by

$$\mathbf{V_P} = \mathbf{A_{321}}\mathbf{V_I}. \tag{2.12}$$

The inverse transformation can be carried out to transform a vector coordinated in the platform axis system to the inertial axis system. The inverse of the DCM is simply it's transpose, which gives the transformation as

$$\mathbf{V_I} = \mathbf{A_{321}^T}\mathbf{V_P}. \tag{2.13}$$

2.4 Euler Rotation Rates

The total angular velocity of the platform in terms of the Euler angles can be written as

$$\boldsymbol{\omega} = \dot{\psi_G}\mathbf{Z_I} + \dot{\theta_G}\mathbf{Y_I'} + \dot{\phi_G}\mathbf{X_I''}. \tag{2.14}$$

Applying Eqs. (2.5), (2.6) and (2.7), the unit vectors in Eq. (2.14) can be transformed to platform axes as

$$\mathbf{Z_I} = -\sin\theta_G \mathbf{X_P} + \sin\phi_G \cos\theta_G \mathbf{Y_P} + \cos\phi_G \cos\theta_G \mathbf{Z_P} \tag{2.15}$$

$$\mathbf{Y'_I} = \cos\theta_G \mathbf{Y_P} - \sin\phi_G \mathbf{Z_P} \tag{2.16}$$

$$\mathbf{X''_I} = \mathbf{X_P}. \tag{2.17}$$

The angular velocity of the platform in platform coordinates is then

$$\boldsymbol{\omega} = \omega_{X_P} \mathbf{X_P} + \omega_{Y_P} \mathbf{Y_P} + \omega_{Z_P} \mathbf{Z_P}. \tag{2.18}$$

Substituting Eqs. (2.15), (2.16) and (2.17) into Eq. (2.14) and rewriting, gives the components of the total angular velocity in platform coordinates as

$$\omega_{X_P} = \dot{\phi}_G - \sin\theta_G \dot{\psi}_G \tag{2.19}$$

$$\omega_{Y_P} = \cos\phi_G \dot{\theta}_G + \sin\phi_G \cos\theta_G \dot{\psi}_G \tag{2.20}$$

$$\omega_{Z_P} = -\sin\phi_G \dot{\theta}_G + \cos\phi_G \cos\theta_G \dot{\psi}_G, \tag{2.21}$$

which in matrix form gives the transformation of the angular rates $\dot{\phi_G}$, $\dot{\theta_G}$, and $\dot{\psi_G}$ to platform body coordinates as

$$\begin{bmatrix} \omega_{X_P} \\ \omega_{Y_P} \\ \omega_{Z_P} \end{bmatrix} = \begin{bmatrix} 1 & 0 & -\sin\theta_G \\ 0 & \cos\phi_G & \sin\phi_G \cos\theta_G \\ 0 & -\sin\phi_G & \cos\phi_G \cos\theta_G \end{bmatrix} \begin{bmatrix} \dot{\phi_G} \\ \dot{\theta_G} \\ \dot{\psi_G} \end{bmatrix}. \tag{2.22}$$

Taking the inverse of the matrix in Eq. (2.22), gives the transformation of the platform angular rate vector in platform coordinates to the gimbal axis system as

$$\begin{bmatrix} \dot{\phi_G} \\ \dot{\theta_G} \\ \dot{\psi_G} \end{bmatrix} = \begin{bmatrix} 1 & \sin\phi_G tan\theta_G & \cos\phi_G tan\theta_G \\ 0 & \cos\phi_G & -\sin\phi_G \\ 0 & \sin\phi_G sec\theta_G & \cos\phi_G sec\theta_G \end{bmatrix} \begin{bmatrix} \omega_{X_P} \\ \omega_{Y_P} \\ \omega_{Z_P} \end{bmatrix}. \tag{2.23}$$

The singularity in the above transformation when $\theta = \frac{\pi}{2}$ or multiples thereof, is not of concern as the platform rotation in θ_G is restricted to $\pm 50°$.

The angular velocities of the inner, middle and outer gimbals are given by

$$\boldsymbol{\omega} = \omega_1 \mathbf{1} + \omega_2 \mathbf{2} + \omega_3 \mathbf{3}. \tag{2.24}$$

Realising that $\mathbf{Z_I} \equiv \mathbf{3}$, $\mathbf{Y'_I} \equiv \mathbf{2}$ and $\mathbf{X''_I} \equiv \mathbf{1}$, the Euler angle rates $\dot{\phi_G}$, $\dot{\theta_G}$ and $\dot{\psi_G}$ is equivalent to the rotation rates of the gimbals, ω_1, ω_2 and ω_3. Thus Eq. (2.23) gives the transformation of the platform angular velocity, coordinated in the platform axis system, to the gimbal axis system.

2.5 Euler's Equations of Motion

The time rate of change of angular momentum of a rigid body is related to the torques applied to the body through Newton's second law for rotational motion as

$$\frac{d\mathbf{H}}{dt} = \mathbf{N}, \tag{2.25}$$

where $\mathbf{N}$ is the torque vector acting on the body and $\mathbf{H}$ is the angular momentum vector of the body defined as

$$\mathbf{H} = \mathbf{I}\boldsymbol{\omega}, \tag{2.26}$$

where $\boldsymbol{\omega}$ is the total angular velocity of the body and

$$\mathbf{I} = \begin{bmatrix} I_{xx} & I_{xy} & I_{xz} \\ I_{yx} & I_{yy} & I_{yz} \\ I_{zx} & I_{zy} & I_{zz} \end{bmatrix} \tag{2.27}$$

is the moment of inertia tensor.

Eq. (2.25) describes the rotational motion of a rigid body in an inertial reference system. It is more convenient to express this equation along body axes, since the moment of inertia tensor is most conveniently expressed along these axes. It is necessary to find the time derivative of $\mathbf{H}$ along the body axes to achieve this. The theorem of Coriolis, given as

$$\left(\frac{d}{dt}\right)_{body}(\cdot) = \left(\frac{d}{dt}\right)_{inertial}(\cdot) + \boldsymbol{\omega} \times (\cdot), \tag{2.28}$$

relates the time derivative of an arbitrary vector $(\cdot)$ in one reference frame to its time derivative in another [3]. Applying Eqs. (2.26) and (2.28) to Eq. (2.25) yields

$$\mathbf{I}\frac{d\boldsymbol{\omega}}{dt} = \mathbf{N} - \boldsymbol{\omega} \times \mathbf{I}\boldsymbol{\omega}. \tag{2.29}$$

Eq. (2.29) is the vector formulation of Euler's equations of motion for a rigid body

where the vector quantities are coordinated in the body axis system [7].

For a body equipped with a flywheel[1], the total angular momentum is the sum of the angular momentum generated by the rotational motion of the body and the angular momentum generated by the flywheel. This is expressed in equation form as

$$\mathbf{H} = \mathbf{I}\boldsymbol{\omega} + \mathbf{h}, \tag{2.30}$$

where $\mathbf{h}$ is the angular momentum of the flywheel. Including the angular momentum of the flywheel in Euler's equations gives

$$\mathbf{I}\frac{d\boldsymbol{\omega}}{dt} = \mathbf{N} - \frac{d\mathbf{h}}{dt} - \boldsymbol{\omega} \times (\mathbf{I}\boldsymbol{\omega} + \mathbf{h}). \tag{2.31}$$

Since the angular momentum of a flywheel is constant,

$$\frac{d\mathbf{h}}{dt} = 0 \tag{2.32}$$

and Eq. (2.31) reduces to

$$\mathbf{I}\frac{d\boldsymbol{\omega}}{dt} = \mathbf{N} - \boldsymbol{\omega} \times (\mathbf{I}\boldsymbol{\omega} + \mathbf{h}). \tag{2.33}$$

Eq. (2.33) describes the motion of a rigid body equipped with an element that produces a constant angular velocity.

2.6 Gyroscope Equations of Motion

To obtain a dynamic model of the gimballed structure, we need to evaluate Eq. (2.33) along each axis that the gyroscope is permitted to precess, i.e. along each of the gimbal rotation axes as defined in Section 2.1.4. Each gimbal is really a separate rigid body and requires a set of three Euler equations to describe its motion. To simplify the analysis we will assume that each gimbal has a spherical moment of inertia tensor, so that cross coupled inertia effects can be ignored. That is,

$$\mathbf{I} = \begin{bmatrix} I_{11} & 0 & 0 \\ 0 & I_{22} & 0 \\ 0 & 0 & I_{33} \end{bmatrix}. \tag{2.34}$$

[1]The addition of a flywheel constitutes that the body is not rigid, but the dynamic equations can still be used [7].

The resultant Euler equations will then only be along the gimbal rotation axes, $O-123$. Along these axes

$$\mathbf{N} = \begin{bmatrix} N_{m1} + N_{w1} \\ N_{m2} + N_{w2} \\ N_{m3} + N_{w3} \end{bmatrix}, \tag{2.35}$$

where $\mathbf{N}_m$ are the steering torques applied to the gimbals and $\mathbf{N}_w$ are the friction torques acting on the gimbals. It is important to realise that $\mathbf{N}$ is not the coordinates of a single geometric vector and do not represent one single physical torque. It is a mathematical vector whose elements are the magnitudes of three real physical torques of a specially defined set, which are generally not orthogonal.

To describe the rotational motion of the inner and middle gimbals, Eq. (2.33) will be evaluated along $O-123''$ and to describe the rotations of the outer gimbal, Eq. (2.33) will be evaluated along $O-1'23$, as defined in Section 2.1. It is necessary to describe the angular velocity vector discussed in Section 2.4 as well as the angular momentum vector generated by the flywheel, along these coordinate systems. Figs. 2.6 and 2.7 illustrate the coordination of vectors between the relevant coordinate systems, and will be used as an aid in the following sections. Fig. 2.6 illustrates a transformation equivalent to Eq. (2.7) and Fig. 2.7 illustrates a transformation equivalent to the inverse of Eq. (2.6).

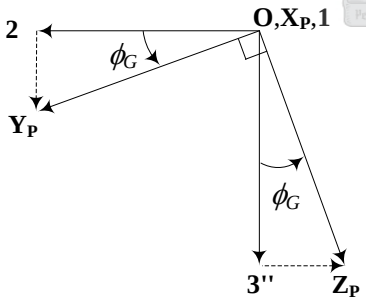

Figure 2.6: Vector transformation from platform axes to $O-123''$

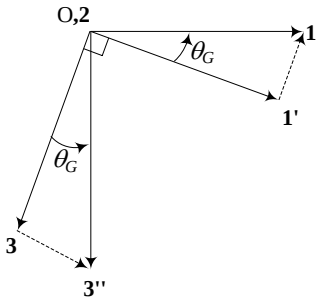

Figure 2.7: Vector transformation from $O-123''$ to $O-1'23$

Equations of Motion Evaluated in $O-123''$

$\omega_3\mathbf{3}$ can be coordinated along $O-123''$ by applying the inverse transformation illustrated in Fig. 2.7,

$$\begin{aligned}\mathbf{A_2}(\theta_G)\boldsymbol{\omega_3} &= \begin{bmatrix}\cos\theta_G & 0 & -\sin\theta_G\\ 0 & 1 & 0\\ \sin\theta_G & 0 & \cos\theta_G\end{bmatrix}\begin{bmatrix}0\\0\\w_3\end{bmatrix}\\ &= \begin{bmatrix}-\omega_3\sin\theta_G\\0\\\omega_3\cos\theta_G\end{bmatrix}.\end{aligned} \tag{2.36}$$

The components of the angular velocity vector coordinated in $O-123''$ are now given by

$$\boldsymbol{\omega_{123''}} = \begin{bmatrix}(\omega_1-\omega_3\sin\theta_G) & \omega_2 & \omega_3\cos\theta_G\end{bmatrix}\begin{bmatrix}\mathbf{1}\\\mathbf{2}\\\mathbf{3''}\end{bmatrix}. \tag{2.37}$$

The angular momentum of the flywheel is always aligned with the Z_P-axis and can be written as

$$\mathbf{h_0} = h_0\mathbf{Z_P}. \tag{2.38}$$

Referring to Fig. 2.6, $\mathbf{h_0}$ coordinated in $O-123''$ can be obtained by applying the transformation

$$\begin{aligned}\mathbf{A_1^T}(\phi_G)\mathbf{h_0} &= \begin{bmatrix}1 & 0 & 0\\ 0 & \cos\phi_G & -\sin\phi_G\\ 0 & \sin\phi_G & \cos\phi_G\end{bmatrix}\begin{bmatrix}0\\0\\h_0\end{bmatrix}\\ &= \begin{bmatrix}0\\-h_0\sin\phi_G\\h_0\cos\phi_G\end{bmatrix}.\end{aligned} \tag{2.39}$$

The angular momentum of the flywheel, coordinated in $O-123''$, is now given by

$$\mathbf{h_{123''}} = \begin{bmatrix}0 & -h_0\sin\phi_G & h_0\cos\phi_G\end{bmatrix}\begin{bmatrix}\mathbf{1}\\\mathbf{2}\\\mathbf{3''}\end{bmatrix}. \tag{2.40}$$

Evaluation of the cross product between the angular momentum and angular

velocity vectors coordinated in $O-123''$ yield

$$\begin{aligned}\boldsymbol{\omega}\times\mathbf{h} &= \begin{vmatrix} \mathbf{1} & \mathbf{2} & \mathbf{3''} \\ \omega_1-\omega_3\sin\theta_G & \omega_2 & \omega_3\cos\theta_G \\ 0 & -h_0\sin\phi_G & h_0\cos\phi_G \end{vmatrix} \\ &= (\omega_2 h_0\cos\phi_G+\omega_3 h_0\sin\phi_G\cos\theta_G)\mathbf{1} \\ &\quad -(\omega_1 h_0\cos\phi_G-\omega_3 h_0\cos\phi_G\sin\theta_G)\mathbf{2} \\ &\quad +(-\omega_1 h_0\sin\phi_G+\omega_3 h_0\sin\phi_G\sin\theta_G)\mathbf{3''}. \end{aligned} \tag{2.41}$$

Substituting Eq. (2.41) into Eq. (2.33), and realising that the $3''$-axis is not a gimbal axis of rotation, gives

$$I_{11}\dot{\omega}_1 = \mathbf{N}_1-\omega_2 h_0\cos\phi_G-\omega_3 h_0\sin\phi_G\cos\theta_G \tag{2.42}$$

$$I_{22}\dot{\omega}_2 = \mathbf{N}_2+\omega_1 h_0\cos\phi_G-\omega_3 h_0\cos\phi_G\sin\theta_G. \tag{2.43}$$

Equations of Motion Evaluated in $O-1'23$

Referring to Fig. 2.7, $\omega_1\mathbf{1}$ coordinated in $O-1'23$ can be obtained by the transformation

$$\begin{aligned}\mathbf{A_2^T}(\theta_G)\boldsymbol{\omega_1} &= \begin{bmatrix} \cos\theta_G & 0 & \sin\theta_G \\ 0 & 1 & 0 \\ -\sin\theta_G & 0 & \cos\theta_G \end{bmatrix}\begin{bmatrix}\omega_1\\0\\0\end{bmatrix} \\ &= \begin{bmatrix}\omega_1\cos\theta_G\\0\\-\omega_1\sin\theta_G\end{bmatrix}. \end{aligned} \tag{2.44}$$

The components of the angular velocity vector coordinated in $O-1'23$, are now given by

$$\boldsymbol{\omega_{1'23}} = \begin{bmatrix}(\omega_1\cos\theta_G) & \omega_2 & (\omega_3-\omega_1\sin\theta_G)\end{bmatrix}\begin{bmatrix}\mathbf{1'}\\\mathbf{2}\\\mathbf{3}\end{bmatrix}. \tag{2.45}$$

The components of $\mathbf{h_0}$ coordinated in $O-1'23$ can be obtained by rotating $O-X_PY_PZ_P$ through ϕ_G to coincide with $O-123''$, as illustrated Fig. 2.6 and then through θ_G to coincide with $O-1'23$, as illustrated in Fig. 2.7. Applying the

transformation yield

$$\mathbf{A_2^T}(\phi_G)\mathbf{A_1^T}(\theta_G)\mathbf{h_0} = \begin{bmatrix} \cos\theta_G & 0 & \sin\theta_G \\ 0 & 1 & 0 \\ -\sin\theta_G & 0 & \cos\theta_G \end{bmatrix} \begin{bmatrix} 1 & 0 & 0 \\ 0 & \cos\phi_G & -\sin\phi_G \\ 0 & \sin\phi_G & \cos\phi_G \end{bmatrix} \begin{bmatrix} 0 \\ 0 \\ h_0 \end{bmatrix}$$
$$= \begin{bmatrix} h_0\cos\phi_G\sin\theta_G \\ -h_0\sin\phi_G \\ h_0\cos\phi_G\cos\theta_G \end{bmatrix}. \tag{2.46}$$

The angular momentum of the flywheel coordinated in $O-1'23$ is now given by

$$\mathbf{h_{1'23}} = \begin{bmatrix} (h_0\cos\phi_G\sin\theta_G) & -h_0\sin\phi_G & (h_0\cos\phi_G\cos\theta_G) \end{bmatrix} \begin{bmatrix} \mathbf{1'} \\ \mathbf{2} \\ \mathbf{3} \end{bmatrix}. \tag{2.47}$$

Evaluation of the cross product between the angular momentum and angular velocity vectors coordinated in $O-1'23$ yield

$$\boldsymbol{\omega_{1'23}} \times \mathbf{h_{1'23}} = \begin{vmatrix} \mathbf{1'} & \mathbf{2} & \mathbf{3} \\ \omega_1\cos\theta_G & \omega_2 & \omega_3 - \omega_1\sin\theta_G \\ h_0\cos\phi_G\sin\theta_G & -h_0\sin\phi_G & h_0\cos\phi_G\cos\theta_G \end{vmatrix}$$
$$= \big(\omega_2 h_0\cos\phi_G\cos\theta_G + \omega_3 h_0\sin\phi_G - \omega_1 h_0\sin\phi_G\sin\theta_G\big)\mathbf{1'}$$
$$- \big(\omega_1 h_0\cos\phi_G(\cos^2\theta_G + \sin^2\theta_G) - \omega_3 h_0\cos\phi_G\sin\theta_G\big)\mathbf{2}$$
$$+ \big(-\omega_1 h_o\sin\phi_G\cos\theta_G - \omega_2 h_0\cos\phi_G\sin\theta_G\big)\mathbf{3}. \tag{2.48}$$

Substituting Eq. (2.48) into Eq. (2.33) and realising that $\mathbf{1'}$ is not a gimbal axis of rotation, gives

$$I_{22}\dot{\omega}_2 = \mathbf{N}_2 + \omega_1 h_0\cos\phi_G - \omega_3 h_0\cos\phi_G\sin\theta_G \tag{2.49}$$
$$I_{33}\dot{\omega}_3 = \mathbf{N}_3 + \omega_1 h_o\sin\phi_G\cos\theta_G + \omega_2 h_0\cos\phi_G\sin\theta_G, \tag{2.50}$$

where the trigonometric property $\sin^2\theta + \cos^2\theta = 1$ has been applied to Eq. (2.48). Eq. (2.49) is identical to Eq. (2.43), which is expected since the 2-axis is common to both the $O-1'23$ and $O-123''$. Eqs. (2.42), (2.49) and (2.50) are the dynamic gimbal equations of motion for the stabilised platform.

2.6.1 Disturbance Torques on Gimbals due to Viscous Friction

Torques will be generated in the gimbal rotation axes due to friction in the rotational elements between the gimbals and must be accounted for in the model. Here we will account for rotations of the gimbal system due to rotations of the airship with regard to inertial space and due to steering of the platform.

The angular velocity of the airship, referred to the inertial axis system will denoted as

$$\boldsymbol{\omega_B^I} = \begin{bmatrix} \omega_{B_X} \\ \omega_{B_Y} \\ \omega_{B_Z} \end{bmatrix} \tag{2.51}$$

and when referred to the gimbal axis system, denoted as

$$\boldsymbol{\omega_B^{123}} = \begin{bmatrix} \omega_{B_1} \\ \omega_{B_2} \\ \omega_{B_3} \end{bmatrix}. \tag{2.52}$$

The torque due to viscous friction in the gimbal axis system is

$$\mathbf{N_w} = \begin{bmatrix} k_{w1} & k_{w2} & k_{w3} \end{bmatrix} \left[\boldsymbol{\omega_B^{123}} - \boldsymbol{\omega} \right], \tag{2.53}$$

where k_{wn} is the coefficient of viscous friction of the n^{th} gimbal and $\boldsymbol{\omega}$ is the angular velocity of the platform in gimbal coordinates.

The components of $\boldsymbol{\omega_B^{123}}$ are obtained as follows. The component of $\boldsymbol{\omega_B}$ in the 1-axis is obtained by coordinating $\boldsymbol{\omega_B}$ in the platform axis system through the DCM given in Eq. (2.11) and taking the resulting component in the X_P-axis, since the 1-axis is aligned with the X_P-axis of the platform. The transformation yield

$$\omega_{B_1} = \omega_{B_X} \cos\theta_G \cos\psi_G + \omega_{B_Y} \cos\theta_G \sin\psi_G - \omega_{B_Z} \sin\theta_G. \tag{2.54}$$

$O - X_B Y_B Z_B$ will be aligned with the 2-axis after a rotation through ψ_G. The component of $\boldsymbol{\omega_B}$ in the 2-axis can be obtained by applying the transformation matrix given by Eq. (2.8) to Eq. (2.51), which yield

$$\omega_{B_2} = -\omega_{B_X} \sin\psi_G + \omega_{B_Y} \cos\psi_G. \tag{2.55}$$

Since the Z_B-axis is aligned with the 3-axis, the component of $\boldsymbol{\omega_B}$ in the 3-axis is simply

$$\omega_{B_3} = \omega_{B_Z}. \tag{2.56}$$

Applying Eqs. (2.54), (2.55) and (2.56) to Eq. (2.53) gives the frictional torque components in the gimbal axis system $O - 123$ as

$$N_{w1} = k_{w1}\big((\cos\theta_G \cos\psi_G \omega_{X_B} + \cos\theta_G \sin\psi_G \omega_{Y_B} - \sin\theta_G \omega_{Z_B}) - \omega_1\big) \tag{2.57}$$

$$N_{w2} = k_{w2}\big((-\omega_{X_B} \sin\psi_G + \omega_{Y_B} \cos\psi_G) - \omega_2\big) \tag{2.58}$$

$$N_{w3} = k_{w3}(\omega_{Z_B} - \omega_3). \tag{2.59}$$

2.7 Summary

This chapter presented the theory behind the development of a mathematical model for the stabilised platform, as well as the derivation of the model. The necessary transformations were defined to obtain all vector quantities in the gimbal axis system. The model will be evaluated critically in Chapter 4.

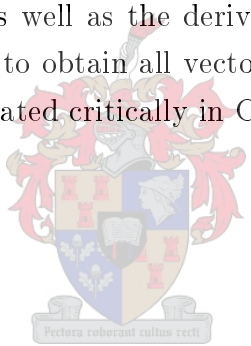

Chapter 3

Platform Development

This chapter describes the development of the platform structure, sensors and actuators as well as the development of the hardware and software to interface these components.

3.1 Three-Degree-of-Freedom Gyroscope

A gyroscope was designed and built in cooperation with the Central Mechanical Services (CMS) at the University of Stellenbosch. The final product is shown in Fig. 3.1. Apart from general gyroscopic construction rules (i.e. each gimbal must be symmetrical and balanced in weight about its axis of rotation), the following design specifications for the development of a gyroscope for use as a stabilised platform were set:

- The gyroscope must have three degrees of rotational freedom for roll, pitch and yaw movement of the platform.
- The construction must allow for a DC motor and potentiometer to be mounted on each gimbal axis as defined in Chapter 2.
- 360 ° of rotation must be allowed in the azimuth plane.
- At least ±45 ° of rotation must be allowed in pitch.
- At least ±25 ° of rotation must be allowed in roll.

Refer to Appendix A for a detailed description of the gyroscope.

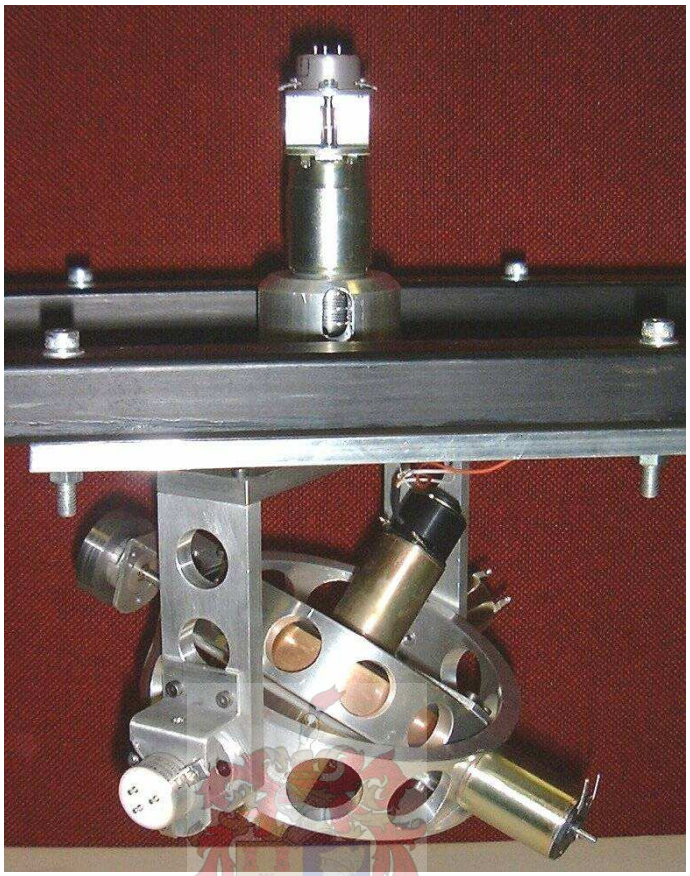

Figure 3.1: Three-degree-of-freedom gyroscope

3.2 Actuators

This section describe the development of the hardware required to perform all necessary actuation. The actuators are grouped as:

- Gimbal motors
- Flywheel

The motor drives will be discussed first, followed by a discussion of the flywheel and gimbal motors. Analogue controllers are then discussed to decouple the actuator dynamics from the main control loop.

3.2.1 Motor Drives

The drive circuitry for each motor consists of a DMOS H-bridge driven by a PWM signal. The PWM signal is generated by a UC3524A microchip. The H-bridge used

is the LMD18200, which has a current sense output pin with a sensitivity of 377 µA per ampere of current through the motor. The current sense output is converted to a voltage through a resistor to ground, which is used as the feedback signal in each torque control system. The voltage measured over the current sense resistor is directly proportional to the torque generated by the motor which is calculated as

$$N = \frac{V_{I\_sense} k_m}{(377 \times 10^{-6}) R_{sense}}, \tag{3.1}$$

where V_{I_sense} is the measured voltage, k_m is the torque constant of the motor and R_{sense} is the value of the resistor used to perform the current conversion.

The block diagram of the gimbal motor drives and of the flywheel motor drive are shown in Fig. 3.2 and Fig. 3.3 respectively. Passive low-pass filtering is performed on the input and output signals of each drive system. The design of the electronic circuits is detailed in Appendix C.

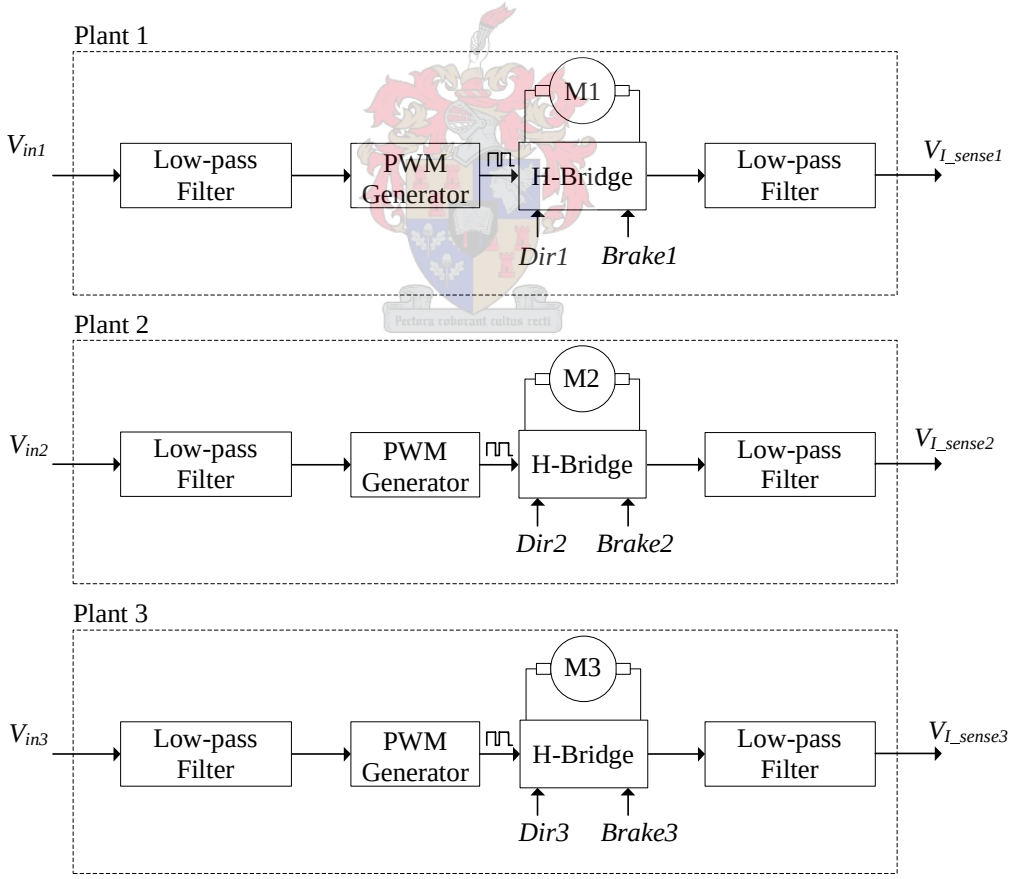

Figure 3.2: Block diagram of gimbal motor drive systems

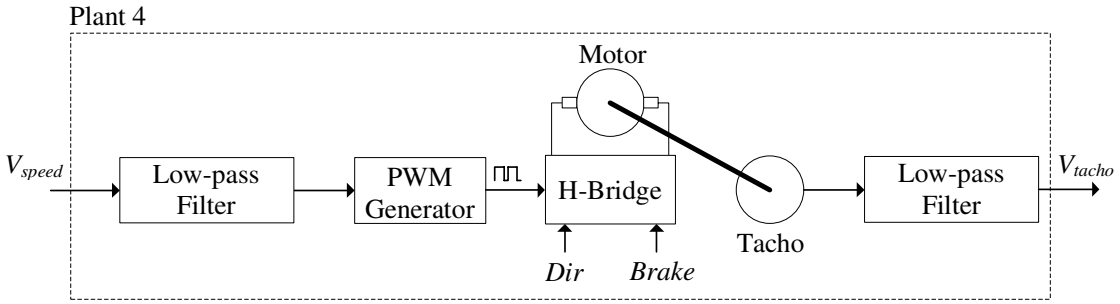

Figure 3.3: Block diagram of flywheel motor drive system

3.2.2 Flywheel

With the following assumptions, the flywheel provides open loop stability to the platform in maintaining a constant reference direction [8]:

- The flywheel spins about an axis of symmetry.
- The flywheel spins at a constant speed.
- Flywheel spin angular momentum is much greater than non-spin angular momentum.

Only the first assumption cannot be guaranteed in the implementation of the platform due to the shape and weight of the payload, but great care will be taken in balancing the weights about the spin axis. The flywheel consist of a balanced brass disc (A disc developed previously in the ESL at the University of Stellenbosch was used as a first iteration) attached to a brushed DC motor (Faulhaber Minimotor 2842-012C) equipped with a tachometer. The tachometer outputs a voltage proportional to the speed of the motor, which can be used in a feedback loop to control the motor speed.

The disc's moment of inertia is $I_f = 3.8 \times 10^{-4}\text{kg}\cdot\text{m}^2$ and the maximum reference speed that can be commanded by the microprocessor is $\omega_f = 3300\text{rpm}$. Therefore the angular momentum generated by the flywheel is

$$\begin{aligned} h_o &= \omega_f I_f \\ &= 0.13132\text{N}\cdot\text{m}\cdot\text{s}. \end{aligned} \tag{3.2}$$

With the flywheel angular momentum as in Eq. (3.2), a reasonable balance is obtained between the required actuator power and control effort, as discussed in Section 1.3. It will be shown in Chapter 4 that for the flywheel angular momentum as

in Eq. (3.2), torques of less than 10 mN·m are required to steer the gimbals at the required angular rate, also discussed in Chapter 4.

3.2.3 Gimbal Motors

The gimbal motors will be used to steer the platform to a new pointing reference and to compensate for disturbance torques on the gimbals. The axle of each motor must be able to rotate freely with minimal friction along with the gimbal it is attached to, when no torque is commanded. The main criteria in selecting the motors to be used are the friction torques and torque delivering capabilities. As stated in the previous section, torques of up to 10 mN·m will be required. With these factors in consideration, ordinary brushed DC motors were selected to be used in the implementation, instead of expensive torque motors. For the inner and middle gimbals (motor 1 and 2), the Faulhaber Minimotor 2842-024C was selected and for the outer gimbal (motor 3), the Faulhaber Minimotor 3042-036C. The 2842-024C motor can deliver torque up to 26 mNm and has a friction torque of 1.2 mNm. The 3042-036C motor can deliver torque up to 41 mNm and has a friction torque of 2.1 mNm. These torque ratings are sufficient to steer the platform at slow angular rates.

3.2.4 Torque Controllers

The dynamics of the actuators can be separated from the main control loop by designing torque controllers with a much higher bandwidth (at least 10 times greater) than that of the main controller, for which a high bandwidth would be redundant. Slow sampling rates can then be used in the main control loop, which simplifies the filtering and A/D and D/A converters needed. The bandwidth of the main controller, discussed in detail in Section 5.2.1, is less than 2 Hz. A model for each plant in Fig. 3.2 must be determined before controllers can be designed.

The controllers designed in the following sections were implemented as analogue circuits, described in Appendices B and C.

Gimbal Motors Plant Identification

Referring to Fig. 3.2, the motor drives' responses to step inputs are shown in Fig. 3.4 for plant 1 and 2 and in Fig. 3.5 for plant 3. These are dominant first order responses

with transfer functions

$$H(s) = \frac{V_{I\_sense}}{V_{in}} = \frac{K}{s+\sigma} \tag{3.3}$$

$$= \frac{\frac{K}{\sigma}}{\tau s + 1}, \tag{3.4}$$

where K/σ is the plant gain and $\tau = \frac{1}{\sigma}$ is the electrical time constant of the plant. The time constant of a first order system is defined as the time at which the unit step response reaches the value $\frac{K}{\sigma}(1-\frac{1}{e})$ [1]. Substituting the values of K and τ obtained from the open loop step responses into Eq. (3.3), gives the transfer functions of plant 1 and 2 as

$$H_1(s) = H_2(s) = \frac{422}{s+521.227} \tag{3.5}$$

and of plant 3 as

$$H_3(s) = \frac{225}{s+712.251}. \tag{3.6}$$

Both systems show a steady state error for step inputs.

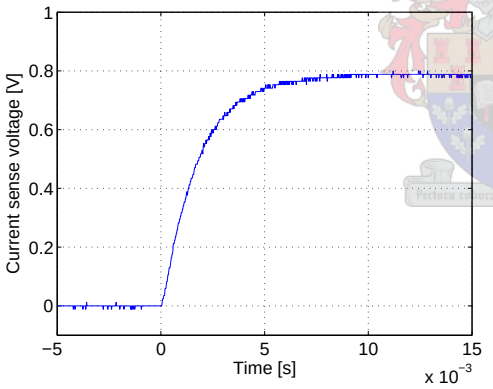

Figure 3.4: Open loop step response of plant 1 and 2

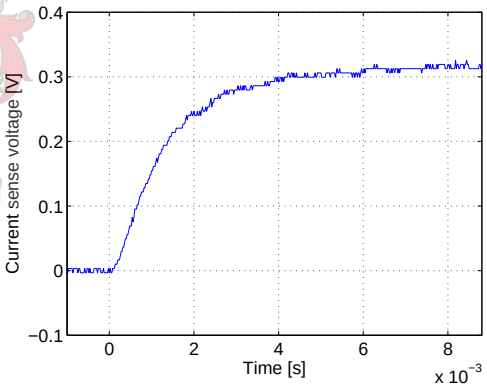

Figure 3.5: Open loop step response of plant 3

Controller Design

Three PI-controllers, one for each gimbal motor, were designed and implemented. This will ensure zero steady state errors for step torque commands and provide control over the bandwidth of the closed loop systems. The closed loop system is shown in Fig. 3.6. The block diagram applies to all three motor drive systems. The

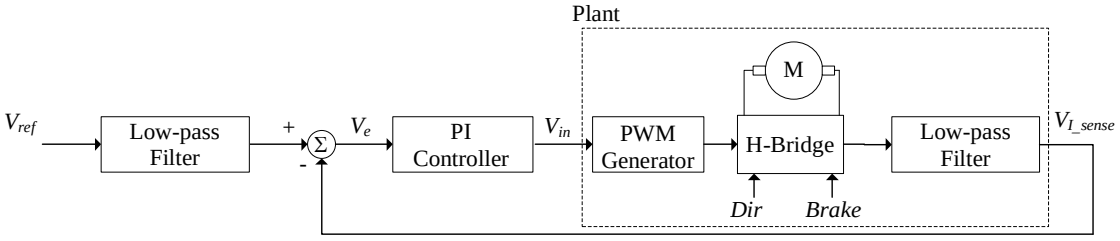

Figure 3.6: Block diagram of torque control loop

PI controller transfer function is given by

$$\begin{aligned} D(s) &= \frac{V_{in}}{V_e} = K_P + \frac{K_I}{s} \\ &= \frac{K_D(s+a)}{s}. \end{aligned} \tag{3.7}$$

Using pole cancellation and selecting $a = \sigma$, the closed loop transfer function of the system is given as

$$G_{cl}(s) = \frac{KK_D}{s + KK_D}. \tag{3.8}$$

The controller gain can be selected to obtain the appropriate closed loop bandwidth. Designing for a closed loop bandwidth of 180 Hz for plants 1 and 2 and for a bandwidth of 65 Hz for plant 3, the resulting controller transfer functions are

$$D_1(s) = D_2(s) = 2.7\left(\frac{s + 521.227}{s}\right) \tag{3.9}$$

and

$$D_3(s) = 1.8\left(\frac{s + 712.251}{s}\right). \tag{3.10}$$

The systems' closed loop poles are situated at $\sigma_{1,2} = 1139.4$ and $\sigma_3 = 408.4$. The simulated and measured step responses are shown in Fig. 3.7 for the closed loop systems of plant 1 and plant 2 and in Fig. 3.8 for the closed loop system of plant 3. All three systems exhibit zero steady state error and the desired bandwidth specifications are met with the controller gains small enough not to cause saturation in the control signal V_{in}.

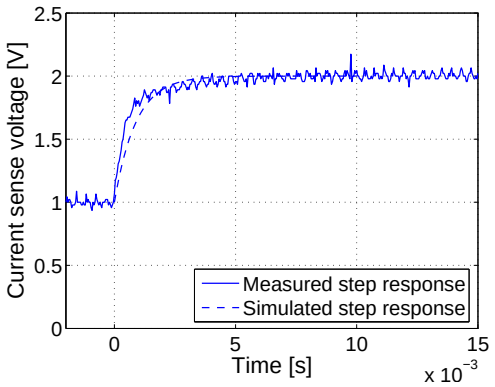

Figure 3.7: Closed loop step response of systems driving motor 1 and 2, for a step in $V_{ref} = 1\text{V}$

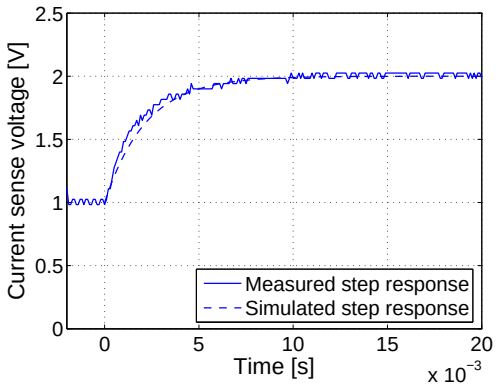

Figure 3.8: Closed loop step response of system driving motor 3, for a step in $V_{ref} = 1\text{V}$

3.2.5 Speed Controller

It is important that the flywheel maintains a constant speed. Any change in speed will result in a change of angular momentum, which will result in a torque being applied to the gimbals. An analogue controller will be designed to regulate the speed of the flywheel. Once again, a model for the flywheel at the relevant operating conditions must first be obtained.

Flywheel Plant Identification

The open loop step response of the flywheel is shown in Fig. 3.9, for a 0.2 V step in V_{speed} about 3000 rpm. From the step response the time constant and plant gain were determined as $\tau = 6.95\text{s}$ and $K = 0.234$. Substituting these values into Eq. (3.3) gives the transfer function of the plant in Fig. 3.3 as

$$H_4(s) = \frac{0.234}{s + 0.144}. \tag{3.11}$$

The plant's step response indicates that system's settling time needs to be decreased.

Controller Design

A PI controller was designed and implemented to increase the bandwidth of the open loop system and to ensure a zero steady state error in the output speed. The block diagram of the closed loop system is shown in Fig. 3.10. Including the PI

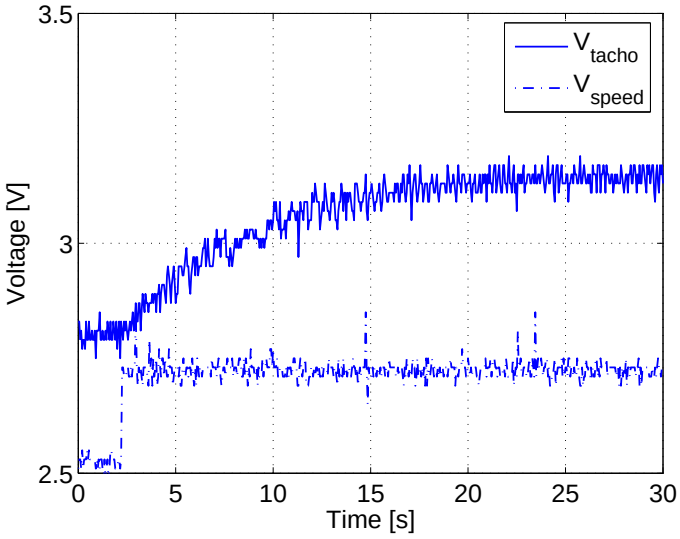

Figure 3.9: Open loop step response of flywheel motor and drive

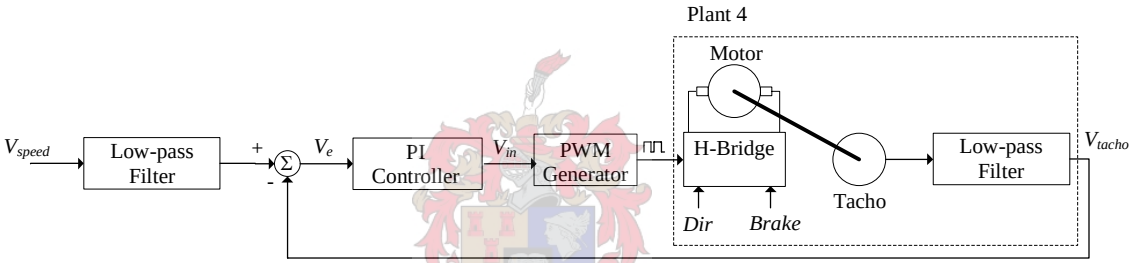

Figure 3.10: Block diagram of speed control loop

controller given in Eq. (3.7), the open loop transfer function of the system is

$$G_{ol}(s) = 0.234K_D\left(\frac{s+a}{s(s+0.144)}\right). \tag{3.12}$$

The root locus of the plant and controller is shown in Fig. 3.11. The speed controller was designed to have a settling time of less than 1 s and a damping factor of $\zeta = 0.7$. Closed loop poles at

$$s_{1,2} = -4.6 \pm 4.69 \tag{3.13}$$

will satisfy this design specification. The resulting PI controller, obtained by the method of root locus design [1], is

$$D_4(s) = 38.7\left(\frac{s+4.723}{s}\right). \tag{3.14}$$

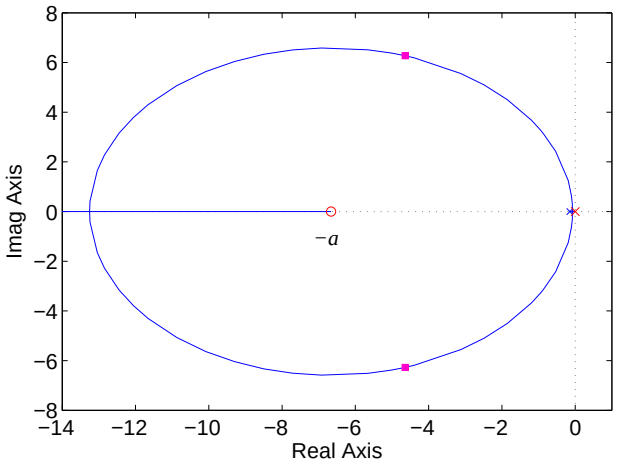

Figure 3.11: Root locus of speed controller

Fig. 3.12 illustrates the measured response of the closed loop system during spin-up. The controller is activated at 1.5 s. The controller saturates during the first 6.5 s while the flywheel reaches nominal speed. At 8 s the flywheel reaches the commanded reference speed and the controller regulates the speed of the flywheel with zero steady state error at 3300 rpm. Overshoot can be observed just after 8 s when the controller reaches 3300 rpm, which is due to the saturation of the controller during the spin-up phase.

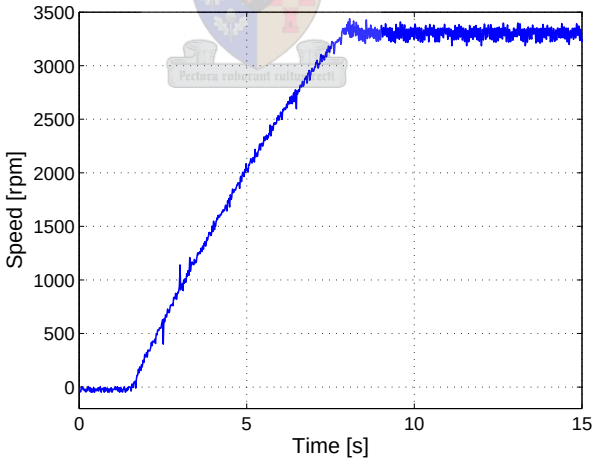

Figure 3.12: Closed loop step response of speed control loop

3.3 Sensors

The gimbal angles and angular rates must be available for feedback to implement a full state feedback control system for the platform. The sensors implemented to measure the platform states are discussed in the following sections.

3.3.1 Angle Sensors

The gimbal angles ϕ_G, θ_G and ψ_G are measured using three 10 kΩ potentiometers (Vishay Spectrol Model 157) mounted on each gimbal. By applying a reference voltage to the potentiometer and measuring the voltage across the center tap of the potentiometer and ground, the gimbal angles can directly be calculated. Allowing for 360° of rotation with a voltage reference of 2.4 V, the gimbal angle in terms of the measured voltage is

$$\theta_{gimbal} = (150 V_{pot})^\circ. \tag{3.15}$$

The block diagram of the angle sensor is shown in Fig. 3.13. The voltage reference is generated by a 2.4 V zener diode circuit. The circuitry is detailed in Appendix C. The resolution that can be obtained by sampling the measured voltage through a

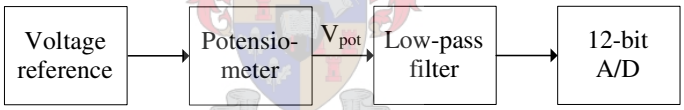

Figure 3.13: Block diagram of angle sensor signal path

12-bit A/D channel with a voltage reference of 2.4 V is

$$\begin{aligned} \theta_{res} &= \frac{360}{2^{12}} \\ &= 0.088^\circ/bit. \end{aligned} \tag{3.16}$$

3.3.2 Inertial Measurement Unit (IMU)

Three single axis IMU boards, developed by Bijker [12], are mounted in a perpendicular configuration to measure the angular rates and accelerations in all three axes of the platform. The single axis IMU boards consists of a ±75 °/s rate gyro (ADXRS401) and an ±1.7 g accelerometer (ADXL203).

The accelerometers output measurements due to static (e.g. gravity) and dynamic (e.g. vibration) accelerations. Utilising the gravity measurement as an input

vector, the accelerometers can be used as a tilt sensor in roll and pitch. There are several drawbacks to this implementation. Firstly, all dynamic acceleration, e.g. displacement of the airship and vibration of the platform due to the flywheel must be compensated for. Secondly, an accelerometer is most sensitive to tilt when its sensitive axis is perpendicular to the earth's gravity vector. The resolution of the sensor declines as the angle between its axis of sensitivity and the earth's gravity vector changes away from 90°. The accelerometer measurements were not used in the development of controllers for the stabilised platform, since the gyros provide sufficient information to use in a feedback controller. They are however available for sampling through the 8-bit A/D channels of the microprocessor.

Fig. 3.14 shows the block diagram of the IMU with conditioning blocks. The gyro

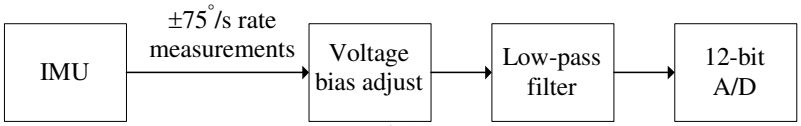

Figure 3.14: Block diagram of IMU signal path

output signals are biased at 2.5 V and must be adjusted to the voltage reference of the Cygnal A/D channels, which is 1.2 V. The adjusted signals are then filtered by anti-aliasing filters before being sampled by the microprocessor at a sampling rate of 1 kHz. The sampled signal is downsampled in the microprocessor to produce an effective sampling rate of 50 Hz. The cut-off frequency of the anti-aliasing filters are 25 Hz. The hardware is detailed in Appendix C.

Calibration

Sensor calibration is necessary to compensate for deviations from the specified output parameters and for misalignments on the platform [12]. The sensors were calibrated by placing the IMU on a rate table and rotating it through 360° for each axis. Since the sensors are sensitive to linear acceleration effects[1], the axis of rotation must be aligned with the earth's gravity vector. A calibration matrix can be calculated by integrating the resulting measurements. The actual rate vector is then

$$\begin{bmatrix} \omega_{x_{cal}} \\ \omega_{y_{cal}} \\ \omega_{z_{cal}} \end{bmatrix} = C \begin{bmatrix} \omega_{x_{sensor}} \\ \omega_{y_{sensor}} \\ \omega_{z_{sensor}} \end{bmatrix} - \begin{bmatrix} \omega_{x_{offset}} \\ \omega_{y_{offset}} \\ \omega_{z_{offset}} \end{bmatrix}, \tag{3.17}$$

[1]The rate gyros used have sensitivity to linear acceleration of 0.2°/s/g [17].

where C is a 3×3 matrix which are equal to the identity matrix if no calibration is necessary. The calibration matrix was calculated as

$$C = \begin{bmatrix} 0.97926 & 0.003656 & 0.02940 \\ -0.03131 & 0.98340 & -0.00583 \\ 0.01232 & -0.02034 & 0.97110 \end{bmatrix}. \tag{3.18}$$

The calibration results are shown in Figs. 3.15 to 3.20.

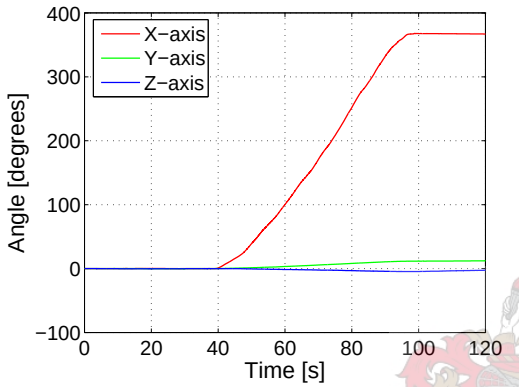

Figure 3.15: Integrated rate gyro measurement in X-axis before calibration

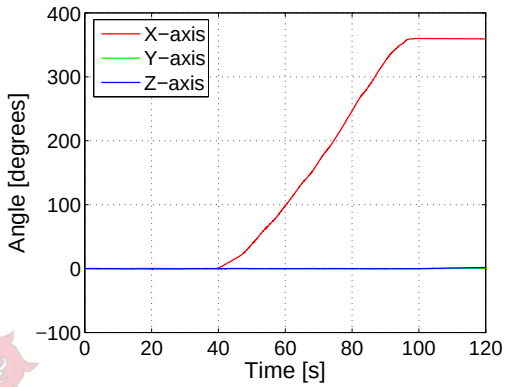

Figure 3.16: Integrated rate gyro measurement in X-axis after calibration

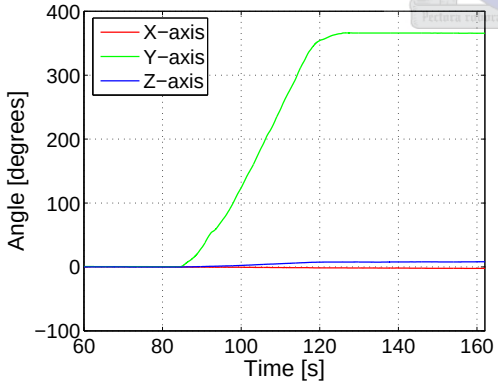

Figure 3.17: Integrated rate gyro measurement in Y-axis before calibration

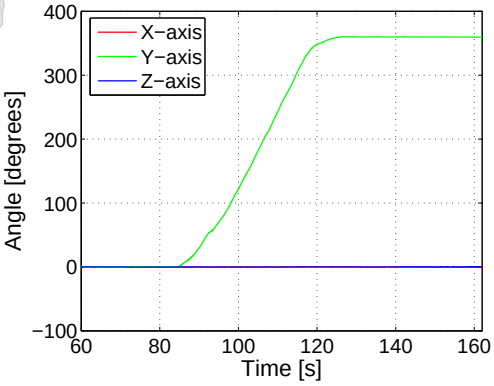

Figure 3.18: Integrated rate gyro measurement in Y-axis after calibration

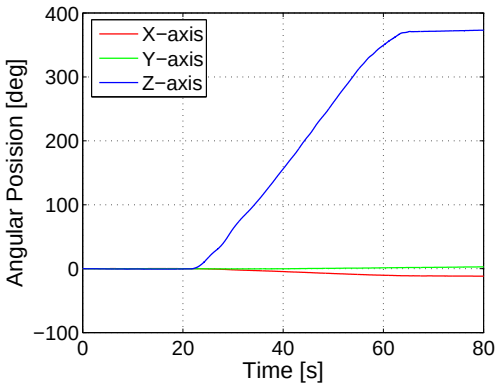

Figure 3.19: Integrated rate gyro measurement in Z-axis before calibration

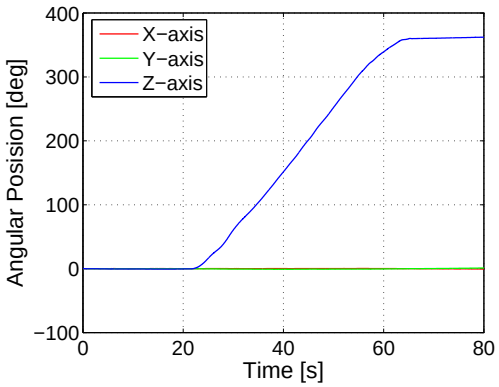

Figure 3.20: Integrated rate gyro measurement in Z-axis after calibration

3.4 Power Distribution

All the components are powered from a single 12 V power supply. The power distribution is illustrated in Fig. 3.21. The power consumption with the gimbal motors inactive is 4.5 W.

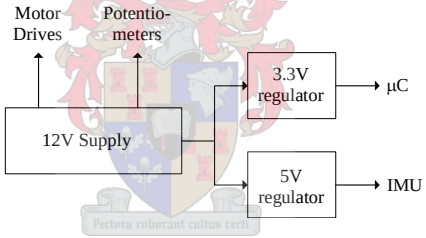

Figure 3.21: Block diagram of power distribution network

3.5 Interface

The main controller, responsible for steering and stabilisation of the platform, interfaces with the actuators and sensors through a microprocessor which is situated on-board the platform. The block diagram of the system is shown in Fig. 3.22.

3.5.1 Microprocessor

The microprocessor used is the Cygnal C8051F020. The following peripherals are utilised in the final implementation of the platform:

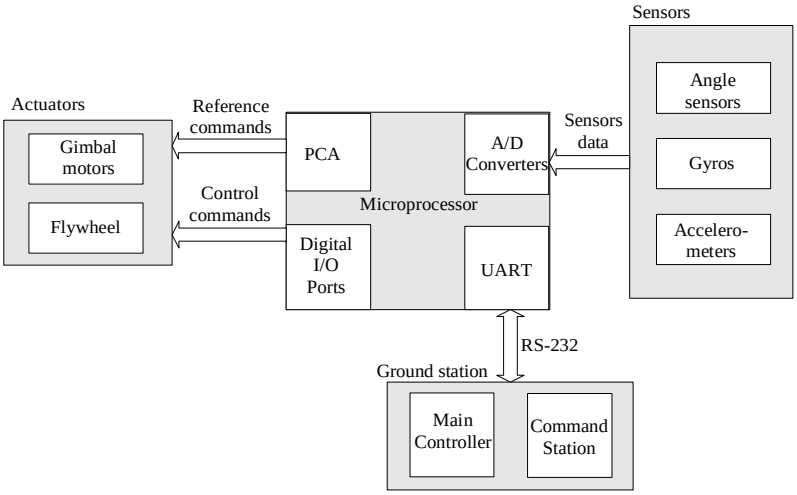

Figure 3.22: Block diagram of controller and actuators/sensors interface

- Six 12-bit A/D channels. Three are used for sampling of the rate measurements from the gyros and another 3 for angle measurements from the potentiometers.
- Four capture/compare modules of the Programmable Counter Array (PCA). These are used for generating analogue voltages which serves as reference commands to the speed and torque controllers.
- Two UART's, of which one is used to communicate with the ground station and another can be implemented to communicate with the OBC that hosts the airship's AHRS.
- One digital output port, of which three pins control the directions of the gimbal motors and another four control the brakes of the gimbal motors and flywheel.

The flow chart of the software running on the microprocessor is illustrated in Fig. 3.23. The sensor data are sampled at an oversample frequency of 1 kHz and downsampled to 50 Hz. The downsample process reduces noise and increases the effective number of bits of the A/D measurement by 2 [19]. The sampled data are encoded as ASCII values for compatibility with the MATLAB Real-Time Toolbox and transmitted over the UART at a rate of 115 200 BAUD.

Parallel to the sampling process, the motor reference torques are received from the main controller and processed. Port0 of the microprocessor is programmed to set the brake and direction pins of each motor drive. Each capture/compare module of the PCA is then programmed to output a PWM signal with a duty cycle

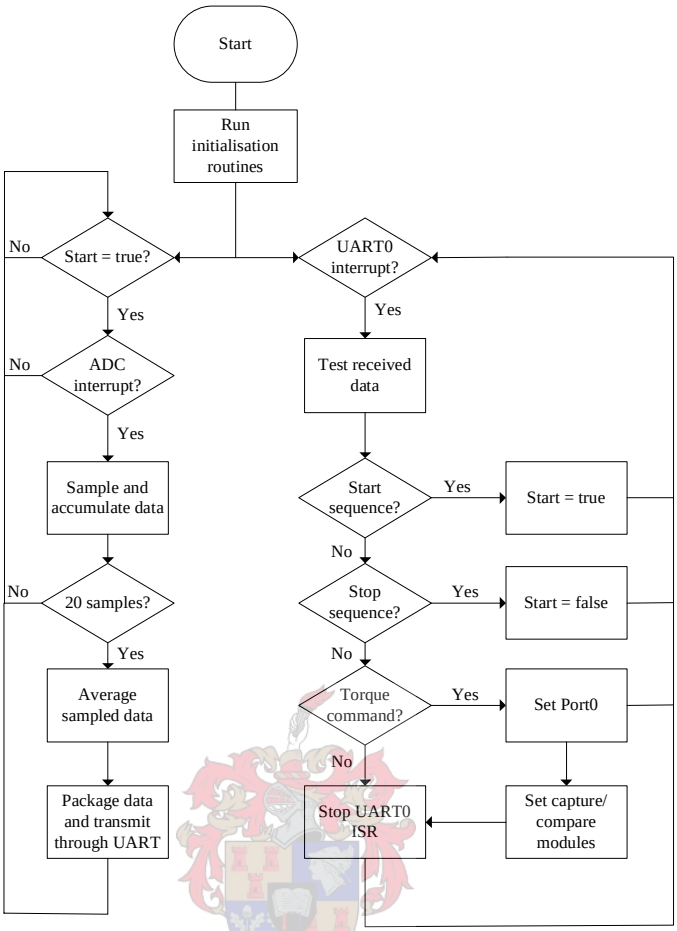

Figure 3.23: Microprocessor embedded software flow chart

proportional to the requested torque. The PWM signal is low-passed filtered to obtain a DC reference voltage for the speed and torque controllers.

3.5.2 Ground Station

The ground station software provides a user with the following functionality:

- Activation/deactivation of on-board microcontroller.
- Resetting IMU gyro offsets.
- Controlling platform roll, pitch and yaw angles.
- Viewing platform angles, angular rates and commanded torques.
- Logging telemetry data.

Fig. 3.24 illustrates the ground station software flow chart. Fig. 3.25 shows a screen shot of the control page of the Borland C++ program that interfaces a user with the platform.

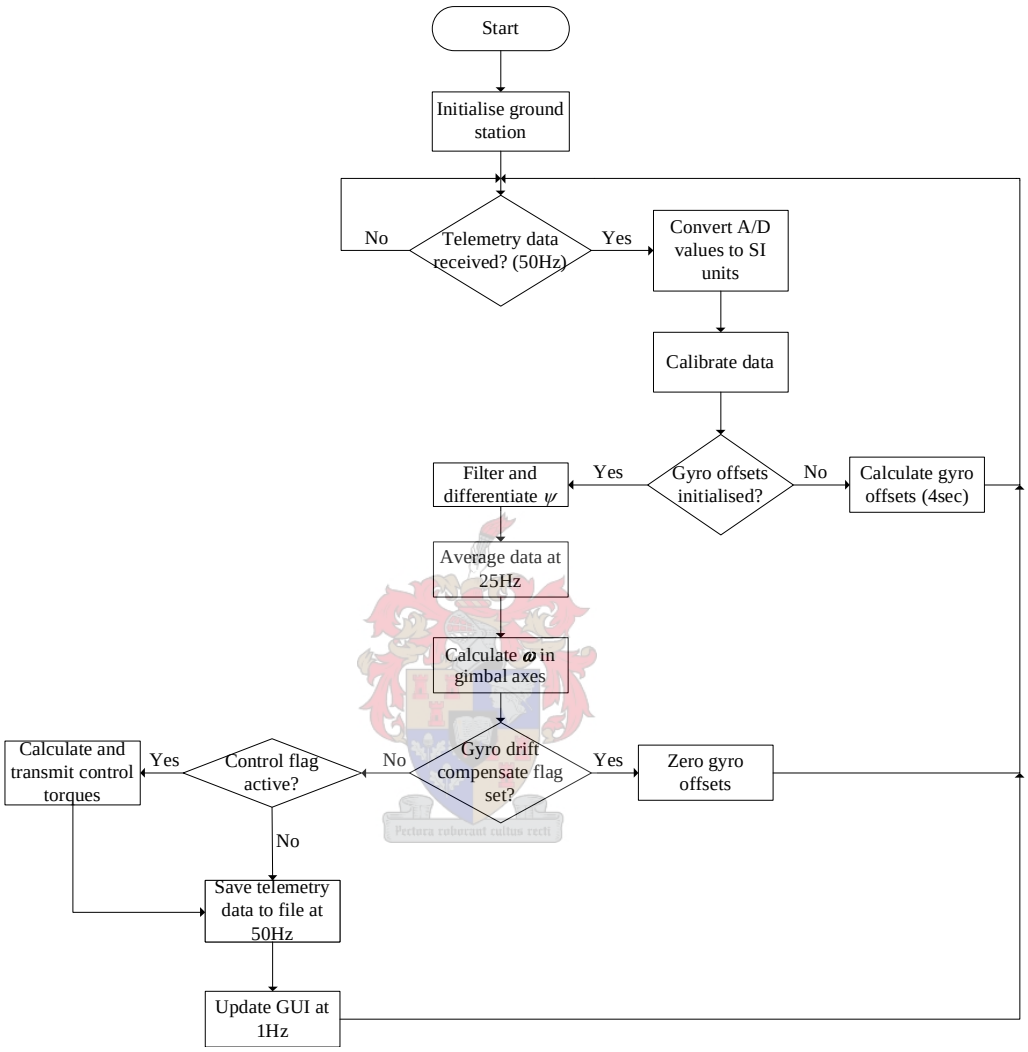

Figure 3.24: Ground station software flow chart

The main controller was developed and implemented on the ground station for testing purposes. The controller can be implemented on the same on-board computer (OBC) as the airship's AHRS in the final integration. Communications between the OBC and ground station are then performed via an RF link. The OBC and RF link are discussed in [12].

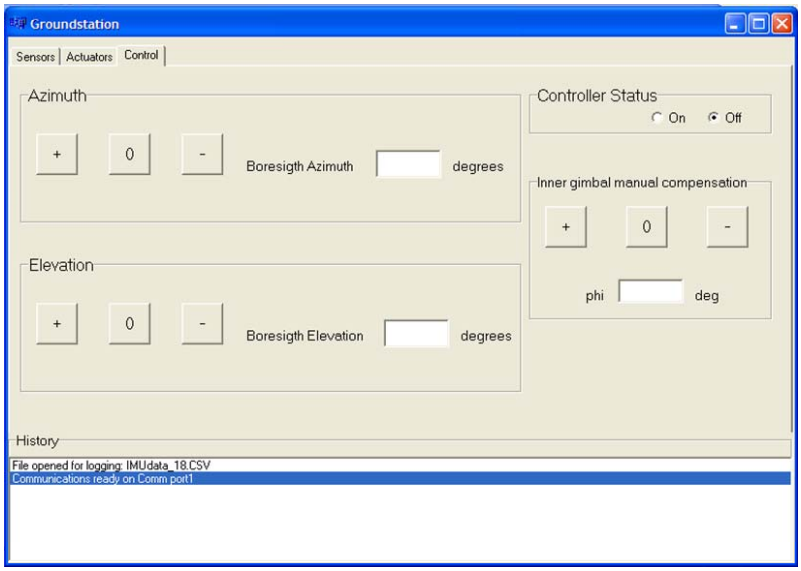

Figure 3.25: Ground station

3.6 Summary

This chapter described the physical implementation of the stabilised platform. An overview of the development of a gimballed structure, along with actuators and sensors necessary to control the platform, were presented.

The structure, along with the payload, weighs approximately 2.7 kg. The total development cost were approximately ZAR 6440 for the electronics, sensors and actuators and ZAR 17 800 for the 3-DOF gyroscope.

Chapter 4

Model Verification and Open Loop Simulations

In this chapter, the open loop behaviour of the model is simulated and compared with measurements of the actual plant. This comparison serves as a basis for determining the model parameters. The effect of the airship's rotations on the platform are also investigated by means of simulations.

4.1 Plant Response to Step Torque Commands

The accuracy of the mathematical model and the model parameters must be evaluated before the design of controllers for the platform can be investigated. The model, derived in Chapter 2, is restated here for convenience.

$$I_{11}\dot{\omega}_1 = N_{m1} + N_{w1} - \omega_2 h_0 cos\phi_G - \omega_3 h_0 sin\phi_G cos\theta_G \tag{4.1}$$

$$I_{22}\dot{\omega}_2 = N_{m2} + N_{w2} + \omega_1 h_0 cos\phi_G - \omega_3 h_0 cos\phi_G sin\theta_G \tag{4.2}$$

$$I_{33}\dot{\omega}_3 = N_{m3} + N_{w3} + \omega_1 h_o sin\phi_G cos\theta_G + \omega_2 h_0 cos\phi_G sin\theta_G, \tag{4.3}$$

with

$$I_{11} = 6.441 \times 10^{-3} kg.m^2$$

$$I_{22} = 7.475 \times 10^{-3} kg.m^2$$

$$I_{33} = 1.39691 \times 10^{-2}\text{kg}\cdot\text{m}^2$$
$$h_0 = -0.1313N.m.s$$

The Simulink model block diagram used to simulate Eqs. (4.1), (4.2) and (4.3) is shown in Fig. 4.1.

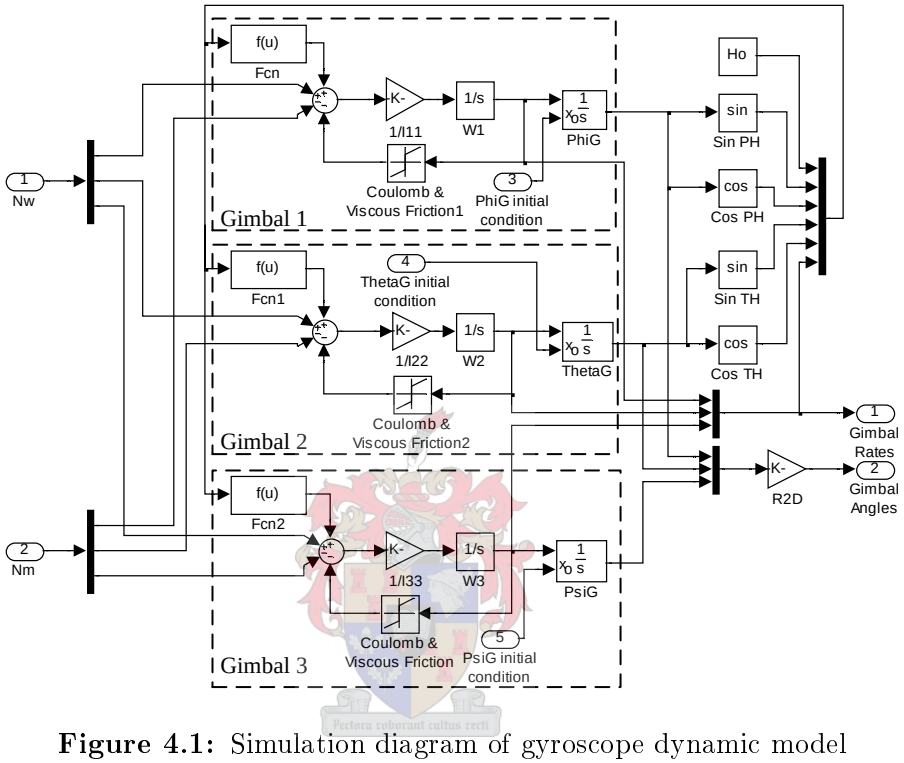

Figure 4.1: Simulation diagram of gyroscope dynamic model

4.1.1 Simulated Response without Friction

Firstly, the open loop behaviour of the platform is investigated with the assumption that the gimbals are free to rotate with respect to each other without any friction acting on the rotational elements. The simulated movement of the platform, for a step of 10 mN·m in N_{m1} and N_{m2}, is shown in Fig. 4.2 and Fig. 4.3 respectively. The initial conditions are $\phi_G(0) = \theta_G(0) = \psi_G(0) = 0$. For a step on the inner gimbal, the initial rotation is only in θ_G (middle gimbal), and as θ_G increases the outer (ψ_G) and inner (ϕ_G) gimbals start to rotate. For a step on the middle gimbal, initially only the inner gimbal rotates and as ϕ_G increases the outer and middle gimbals start to rotate. Periodic oscillations (the nutational modes of a gyroscope) are also visible

on the output of the system. The simulation results correspond to the movement of the gyroscope described in Section 1.3.

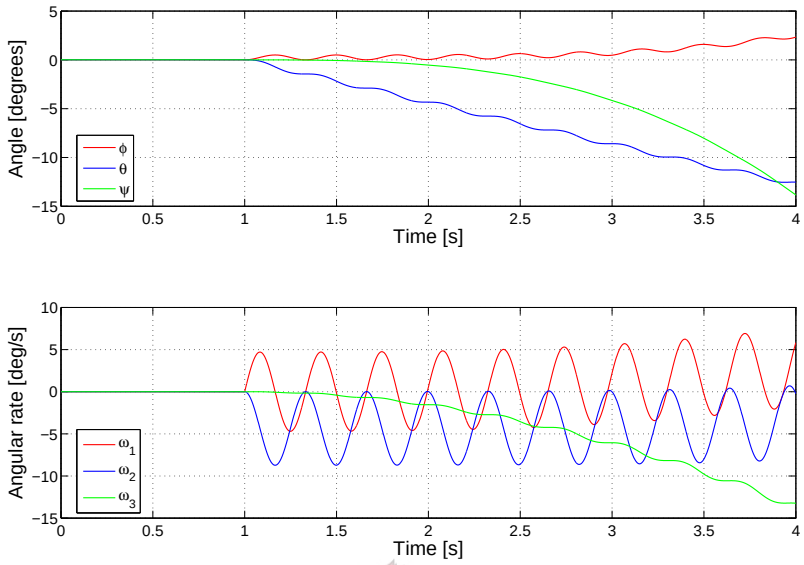

Figure 4.2: Simulated step response for a torque step command to gimbal 1

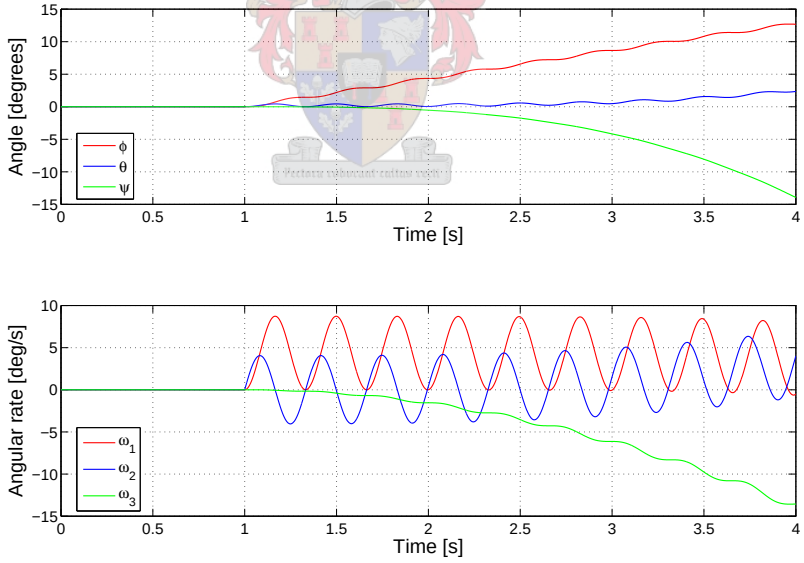

Figure 4.3: Simulated step response for a torque step command to gimbal 2

4.1.2 Measured Response

We now investigate the measured open loop behaviour of the plant. The results are compared with the simulation results from the previous section. The measured responses to step commands are shown in Fig. 4.4 for a step in N_{m1} of 10 mN·m and in Fig. 4.5 for a step in N_{m2} of 10 mN·m. It can be seen that for a step on gimbal 1, the mean of the angular velocity of the inner gimbal, $\bar{\omega}_1$, is not equal to zero as expected. Similarly, for a step on gimbal 2 we find that $\bar{\omega}_2 \neq 0$. Damping of the angular rates can also be observed.

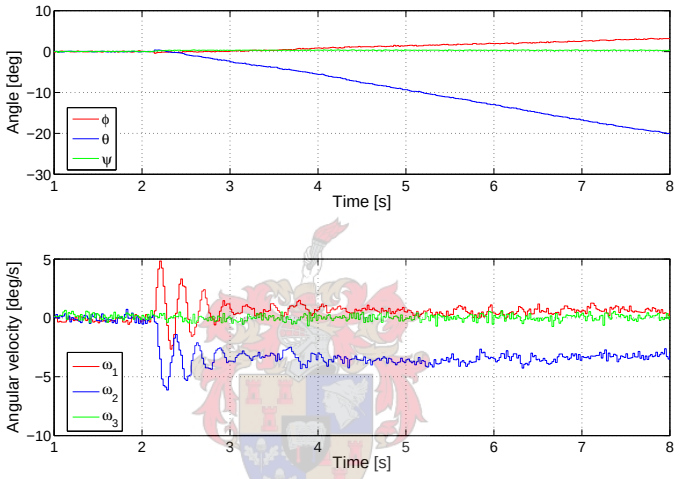

Figure 4.4: Measured step response for a torque step command to gimbal 1

The damping and offsets are mainly due to viscous and coulomb friction in the rotational elements of the gimbals. Comparing the simulated and measured step response, it is clear that friction has a significant effect on the response of the system and cannot be ignored in the model. The main sources of friction are the potentiometers, motors and wiring.

Another important observation from Fig. 4.4 is that ω_3 is zero for all time. From consecutive measurements were found that for torque values commanding slow angular rates (i.e. $\omega < 0.03$rad/s), gimbal 3 is decoupled from the movement of gimbal 1 and 2 and vice versa. This is due to the large coefficients of static friction between gimbal 3 and the base to which it is attached and between the contact points of gimbal 1 and gimbal 2. The effect of static friction can be used as an advantage in the design of steering controllers for the platform, since gimbal 3 can

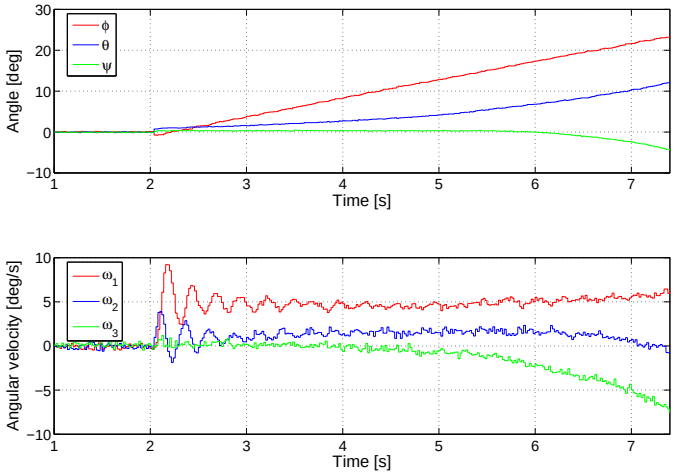

Figure 4.5: Measured step response for a torque step command to gimbal 2

be mathematically decoupled from gimbals 1 and 2 for small angular rates. This will be discussed further in Chapter 5.

4.2 Parameter Estimation

The non-linear effects of the wires between the gimbals make measurements of gimbal moment of inertia and coefficients of friction difficult and inaccurate. These parameters can however be determined more precisely by a comparison of the simulated and measured system responses.

The moment of inertia of each gimbal can be determined by comparing the frequency of oscillation of the simulated and measured step responses, as determined by the relationship expressed in Eq. (1.3). The final parameters, determined by a process of iteration, are given in Table 4.1. The model for frictional torque used in

Table 4.1: Physical properties of gimbals

Gimbal	Moment of Inertia $[\text{kg}\cdot\text{m}^2]$	Coefficient of viscous friction $\left[\frac{\text{N}}{\text{m}\cdot\text{s}^{-1}}\right]$
Outer (3)	7.14×10^{-3}	4.5×10^{-3}
Middle (2)	5.263×10^{-3}	4×10^{-3}
Inner (1)	4.587×10^{-3}	4×10^{-3}

the simulations, with $\boldsymbol{\omega_B} = 0$, are

$$N_{w1} = -\big(k_{w1}\omega_1 + 0.0015 sgn(\omega_1)\big) \tag{4.4a}$$
$$N_{w2} = -\big(k_{w2}\omega_2 + 0.0015 sgn(\omega_2)\big) \tag{4.4b}$$
$$N_{w3} = -\big(k_{w3}\omega_3 + 0.002 sgn(\omega_3)\big). \tag{4.4c}$$

To ensure that the simulations represent a good approximation of the physical system, sensor noise is included at the angular rate outputs of the simulation model. The sensor noise are modelled as band-limited white noise, with RMS values calculated from actual sensor measurements at the control bandwidth of

$$\sigma_{\omega_1} = 0.003347\text{rad/s} \tag{4.5a}$$
$$\sigma_{\omega_2} = 0.003277\text{rad/s} \tag{4.5b}$$
$$\sigma_{\omega_3} = 0.003529\text{rad/s}. \tag{4.5c}$$

The simulated and measured step responses are shown in Figs. 4.6, 4.7 and 4.8, where the parameters of Table 4.1 and Eqs. (4.4) and (4.5) were used in the simulations. It can be seen that some uncertainty in the model parameters still exists. This is partially due to unmodelled dynamics (e.g. the effect of the wires) and assumptions made in the modelling process, e.g. assuming a spherical moment of inertia tensor. More exact plant parameters can be obtained by applying a deterministic estimation method like least squares estimation [2]. However, the above mentioned parameters describe the plant to a close enough approximation to yield good control results. The spring effects in the wires, visible in Fig. 4.8, remain unmodelled, but will be taken into account in the controller design process. The effect of the wires can be eliminated with the use of slip rings.

4.3 Effect of Airship Rotations on Platform

A model for the airship's rotations must be determined before the pointing stability of the platform in the presence of disturbance torques can be evaluated in simulation. Typical rotations of a small blimp are illustrated in Fig. 4.9 [12]. The maximum amplitude of the roll, pitch and yaw angles were measured as $\phi_P \approx 30°$, $\theta_P \approx 15°$ and $\psi_P \approx 100°$. For simulation purposes, the rotations can be approximated by sinusoidal waves having periods of 16 s for roll rotation, 6 s for pitch rotation and

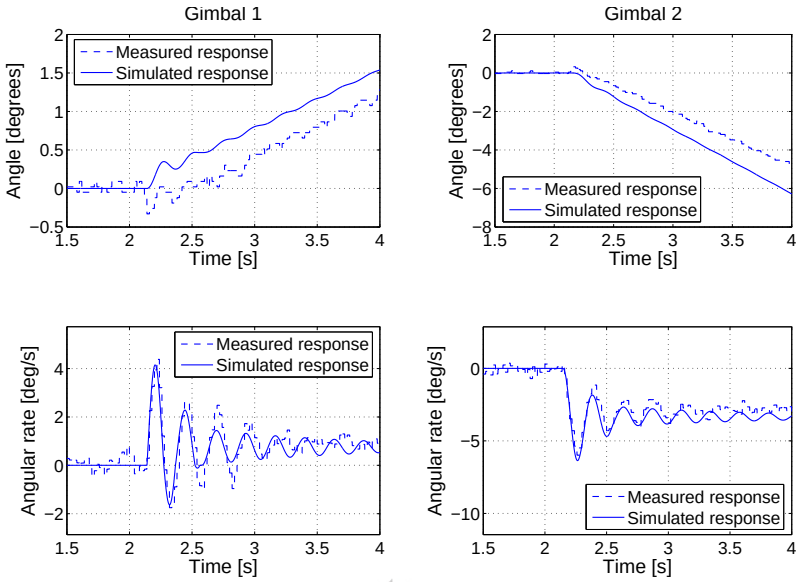

Figure 4.6: Measured and simulated step responses for a torque step command to gimbal 1 of $N_{w1} = 8.5\text{mN}\cdot\text{m}$

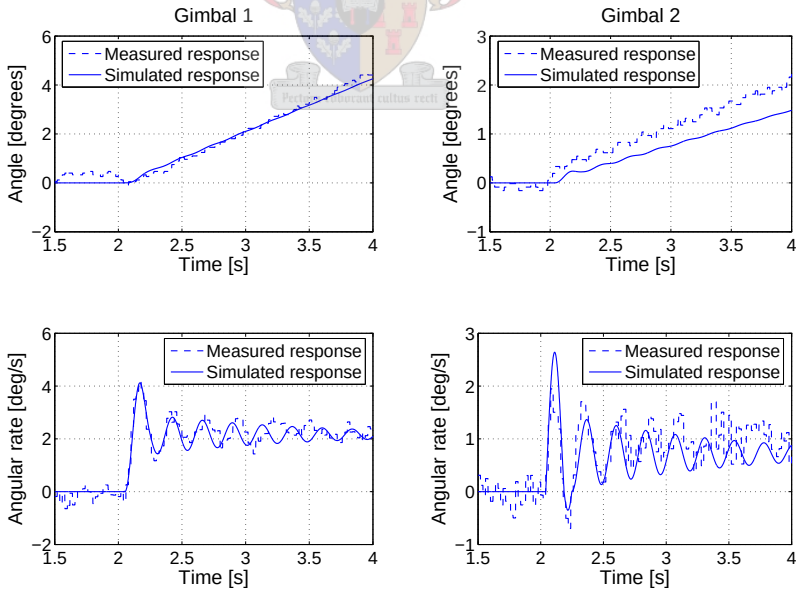

Figure 4.7: Measured and simulated step responses for a torque step command to gimbal 2 of $N_{w2} = 6\text{mN}\cdot\text{m}$

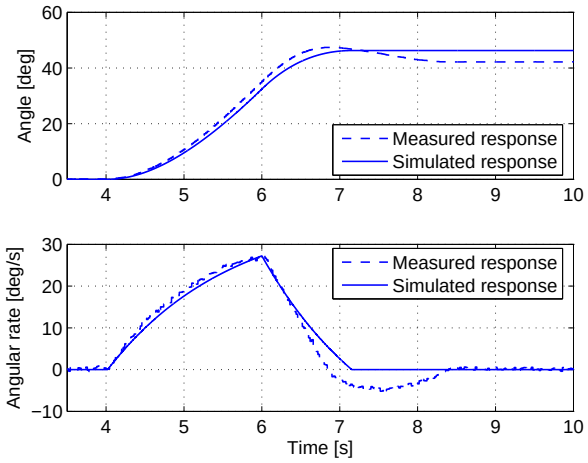

Figure 4.8: Measured and simulated step responses for a torque pulse command to gimbal 3 of $N_{w3} = 8\text{mN}\cdot\text{m}$ with a duration of 2 s ($\theta = \phi = 0°$)

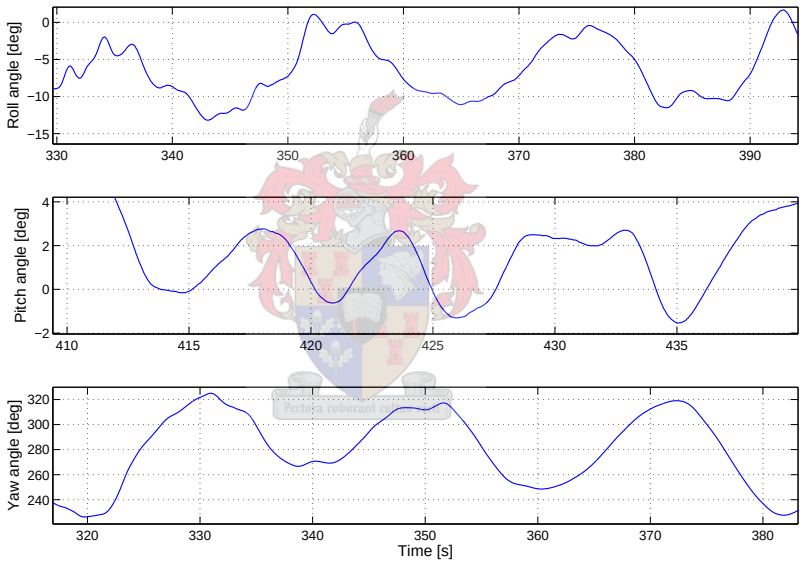

Figure 4.9: Typical roll, pitch and yaw rotation angles of a small blimp [12]

20 s for yaw rotation. Hence,

$$\omega_{B_X} = 0.205 sin\left(\frac{\pi}{8}t\right), \tag{4.6}$$

$$\omega_{B_Y} = 0.274 sin\left(\frac{\pi}{3}t\right) \tag{4.7}$$

and

$$\omega_{B_Z} = 0.55 sin\left(\frac{\pi}{10}t\right). \tag{4.8}$$

The effect of the airship's rotations on the platform can be investigated by simulating Eqs. (4.1), (4.2) and (4.3) with $\mathbf{N_w}$ as in Eqs. (2.57), (2.58) and (2.59) and the airship's angular rates $\boldsymbol{\omega}_B$ as given above.

The simulation results are shown in Fig. 4.10. The platform deviates from its pointing reference with up to 6° in azimuth and 7° in elevation. The RMS errors in the azimuth and elevation planes are 2.6151° and 2.0493° respectively. Gimbal 3 experience angular rates of up to 0.2 rad/s and gimbals 1 and 2 experience angular rates of up to 0.093 rad/s due to torque disturbances. The controller should be designed to compensate for these disturbances.

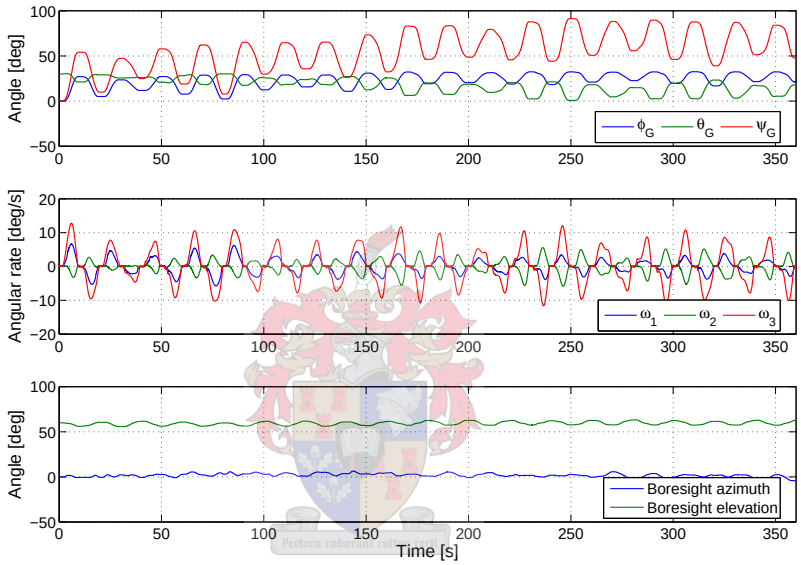

Figure 4.10: Simulated effect of blimp movement on platform due to viscous friction

Chapter 5

Platform Controller Design

This chapter begins by stating the strategy on which the controller designs are based. Thereafter, the theory and design of the controllers responsible for platform steering and disturbance torque rejection, are presented. This include the derivation of a linear platform model. Finally, the controllers are evaluated in simulation.

5.1 Control Strategy

As was seen in Chapter 4, the equations governing the motion of the platform can be decoupled at slow angular rates, reducing the complexity of the controllers needed to steer the platform. Two separate controllers will be designed, one to control motion in the azimuth plane (SISO controller) and another to control motion in the elevation plane (MIMO controller having two input and output variables). This is a sound strategy even for disturbance torque rejection, since the dynamics of an airship are very slow [12].

The main focus in the controller design process will be on the design of steering controllers for the platform. The performance of the platform's pointing stability in terms of disturbance torque rejection will only be evaluated in simulations, since the platform cannot at present be physically tested in an environment where it is subjected to actual airship rotation rates.

Measurements of the platform's angular rates, coordinated in the gimbal axis system, will be used as feedback in the control loops. Reference angular rates can then easily be commanded to steer the platform's pointing direction to a desired angle in azimuth or elevation. Regulation of the angular rates at 0 rad/s will ensure that the platform maintains a constant pointing direction. The errors in ϕ_G, θ_G and

ψ_G will be evaluated for each controller and will be used as a criterion to determine the tracking performance, even though an angle is not physically commanded.

5.2 Elevation Controller

The elevation angle of the platform is determined by the orientation of the middle and inner gimbals. The middle gimbal will be the primary steering device for elevation pointing, as it's rotation angle is much greater than that of the inner gimbal. The inner gimbal will only be used to compensate for rotations of the airship.

5.2.1 Specifications and Sample Rate Selection

As was seen in Section 4.3, the controller should be able to compensate for disturbance signals with frequency content up to $\frac{\pi}{3}$rad/s. To ensure that the controller will be able to react to these disturbances, the closed loop system bandwidth is selected as

$$w_b = 1.6\text{rad/s}. \tag{5.1}$$

Speed response specifications are not critical for the functioning of the elevation steering controller. However, a faster angular rate response will result in smaller steady state angle tracking errors and faster disturbance rejection capabilities. Also, a response that is too fast can stimulate unmodelled dynamics and exceed physical limitations in the system which will lead to instability. With the above in consideration, the following specifications are set for the elevation controller:

- Rise time of under 2 s
- Overshoot of less than 10 % on the commanded output
- Zero steady state error
- Be able to track angular rates of 0.03 rad/s without effecting ψ_G

The selection of the sampling frequency of a discrete system, ω_s, is mainly determined by the closed loop bandwidth of the system in accordance to the relation

$$\frac{\omega_s}{\omega_b} > 20. \tag{5.2}$$

This will ensure a reasonably smooth control response (i.e., at least ten samples per rise time) [2]. By substituting Eq. (5.1) into Eq. (5.2), a lower bound for the sampling frequency is calculated as

$$f_s = \frac{\omega_s}{2\pi} \geq 5\text{Hz}. \tag{5.3}$$

Another important constraint on the sampling time of the elevation controller is the fact that the plant has lightly damped modes, evident from the open loop measurements of Chapter 4. These resonant frequencies, illustrated in Fig. 5.1, will be excited by disturbance torques and must be sufficiently damped by the controller to ensure stability in the platform's pointing direction. For the controller to be able to react to these resonances, the sampling frequency must be chosen greater than twice the resonant frequency [2], that is

$$\begin{aligned} \omega_s &> 2\omega_r \\ \Rightarrow f_s &> 8.6\text{Hz}. \end{aligned} \tag{5.4}$$

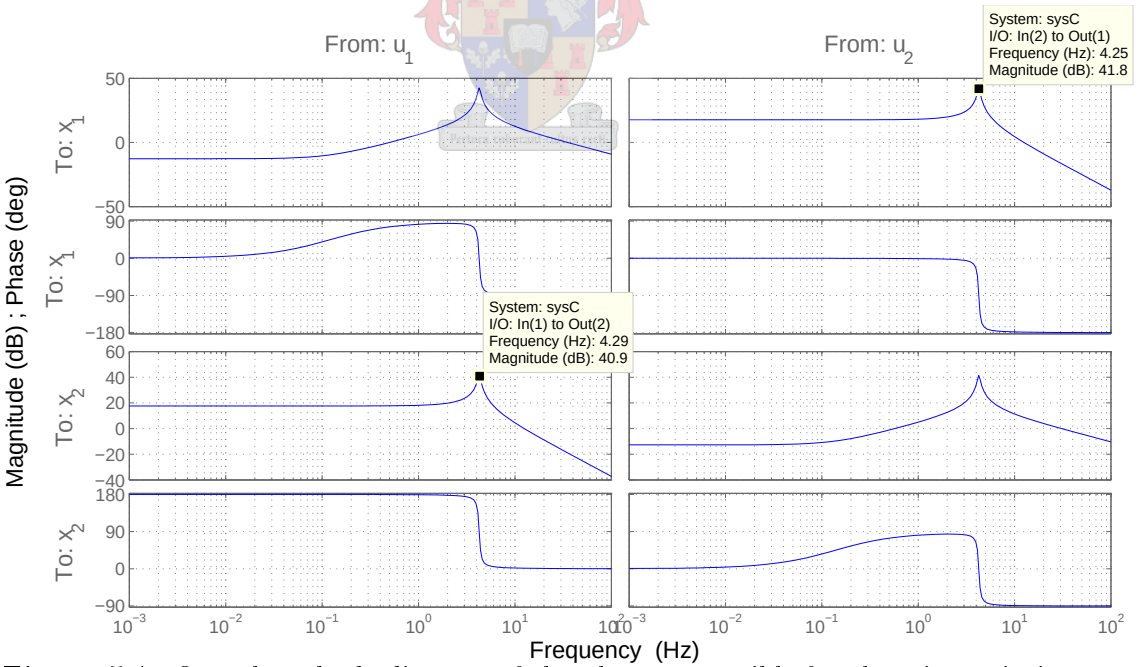

Figure 5.1: Open loop bode diagram of the plant responsible for elevation pointing

From a practical perspective, it is desirable to choose the sample rate of the con-

troller as slow as possible. The signal to noise ratio of the sensor measurements will increase as the sample rate decreases when oversampling and averaging is used [19], as is implemented in this project. Less measurement noise will result in more robust controllers and simpler post processing algorithms (e.g. obtaining the derivative of a measurement).

With the above factors in consideration, a good choice for the sample frequency, which satisfy Eqs. (5.3) and (5.4), is

$$f_s = 25\text{Hz}. \tag{5.5}$$

5.2.2 State Equations and Control Law

The plant for the elevation controller consists of the middle and inner gimbals of the gyroscope. The system has two control inputs, N_{m1} and N_{m2}, and two outputs to be controlled, ω_1 and ω_2. To design a controller for the MIMO system, state space techniques will be used. The system can be described by the state equations

$$\dot{\mathbf{x}} = \mathbf{F}\mathbf{x} + \mathbf{G}\mathbf{u} \tag{5.6}$$

$$\mathbf{y} = \mathbf{H}\mathbf{x} + \mathbf{J}\mathbf{u}, \tag{5.7}$$

where $\mathbf{x}$ is the state vector, $\mathbf{F}$ is the state matrix, $\mathbf{u}$ is the input vector, $\mathbf{G}$ is the input matrix, $\mathbf{H}$ is the output matrix and $\mathbf{J}$ is the feedforward matrix.

The dynamic equations for the system of gimbal 1 and gimbal 2, decoupled from the movement of gimbal 3, i.e. $w_3 = 0$, are

$$I_{11}\dot{\omega}_1 = N_1 - \omega_2 h_0 cos\phi_G - k_{w1}\omega_1 \tag{5.8}$$

$$I_{22}\dot{\omega}_2 = N_2 + \omega_1 h_0 cos\phi_G - k_{w2}\omega_2. \tag{5.9}$$

The state vector is chosen as

$$\mathbf{x} = \begin{bmatrix} \omega_1 \\ \omega_2 \\ \phi_G \\ \theta_G \end{bmatrix}. \tag{5.10}$$

Defining the functions

$$f_1(\phi_G, \theta_G, \omega_1, \omega_2, N_1, N_2) = \dot{\omega}_1 = \frac{N_1}{I_{11}} - \frac{\omega_2 h_0 cos\phi_G}{I_{11}} - \frac{k_{w1}\omega_1}{I_{11}} \tag{5.11}$$

$$f_2(\phi_G, \theta_G, \omega_1, \omega_2, N_1, N_2) = \dot{\omega}_2 = \frac{N_2}{I_{22}} + \frac{\omega_1 h_0 cos\phi_G}{I_{22}} - \frac{k_{w2}\omega_2}{I_{22}} \tag{5.12}$$

$$f_3(\phi_G, \theta_G, \omega_1, \omega_2, N_1, N_2) = \dot{\phi}_G = \omega_1 \tag{5.13}$$

$$f_4(\phi_G, \theta_G, \omega_1, \omega_2, N_1, N_2) = \dot{\theta}_G = \omega_2, \tag{5.14}$$

the system can be linearised for small perturbations in $\mathbf{x}$ about the point $(\omega_{1_0}, \omega_{2_0}, \phi_{G_0}, \theta_{G_0})$. The linearized state matrix is calculated as

$$\begin{aligned} F &= \begin{bmatrix} \frac{\partial f_1}{\partial \omega_1} & \frac{\partial f_1}{\partial \omega_2} & \frac{\partial f_1}{\partial \phi_G} & \frac{\partial f_1}{\partial \theta_G} \\ \frac{\partial f_2}{\partial \omega_1} & \frac{\partial f_2}{\partial \omega_2} & \frac{\partial f_2}{\partial \phi_G} & \frac{\partial f_2}{\partial \theta_G} \\ \frac{\partial f_3}{\partial \omega_1} & \frac{\partial f_3}{\partial \omega_2} & \frac{\partial f_3}{\partial \phi_G} & \frac{\partial f_3}{\partial \theta_G} \\ \frac{\partial f_4}{\partial \omega_1} & \frac{\partial f_4}{\partial \omega_2} & \frac{\partial f_4}{\partial \phi_G} & \frac{\partial f_4}{\partial \theta_G} \end{bmatrix} \\ &= \begin{bmatrix} -\frac{k_{w1}}{I_{11}} & -\frac{h_0 cos\phi_{G_0}}{I_{11}} & \omega_{2_0}\frac{h_0 sin\phi_{G_0}}{I_{11}} & 0 \\ \frac{h_0 cos\phi_{G_0}}{I_{22}} & -\frac{k_{w2}}{I_{22}} & -\omega_{1_0}\frac{h_0 sin\phi_{G_0}}{I_{22}} & 0 \\ 1 & 0 & 0 & 0 \\ 0 & 1 & 0 & 0 \end{bmatrix}, \end{aligned} \tag{5.15}$$

where the partial derivatives are evaluated at $(\omega_{1_0}, \omega_{2_0}, \phi_{G_0}, \theta_{G_0})$. Since ω_1 and ω_2 will be nominally zero during stabilization and small ($\omega < 0.03$rad/s) during platform steering and because ϕ_G will in general be small, the state matrix can be simplified as

$$F = \begin{bmatrix} -\frac{k_{w1}}{I_{11}} & -\frac{h_0 cos\phi_{G_0}}{I_{11}} & 0 & 0 \\ \frac{h_0 cos\phi_{G_0}}{I_{22}} & -\frac{k_{w2}}{I_{22}} & 0 & 0 \\ 1 & 0 & 0 & 0 \\ 0 & 1 & 0 & 0 \end{bmatrix}. \tag{5.16}$$

Eq. (5.16) shows that the angular rate states, x_1 and x_2, are independent of the angle states x_3 and x_4 and can therefore be decoupled. To steer the platform, the gimbal

angular rates ω_1 and ω_2 will be controlled and the angle states can be omitted from the state vector to yield the simplified state equations as

$$\dot{\mathbf{x}} = \begin{bmatrix} -\frac{k_{w1}}{I_{11}} & -\frac{h_0 cos\phi_{G_0}}{I_{11}} \\ \frac{h_0 cos\phi_{G_0}}{I_{22}} & -\frac{k_{w2}}{I_{22}} \end{bmatrix} \mathbf{x} + \begin{bmatrix} \frac{1}{I_{11}} & 0 \\ 0 & \frac{1}{I_{22}} \end{bmatrix} \mathbf{u} \tag{5.17}$$

$$\mathbf{y} = \begin{bmatrix} 1 & 0 \\ 0 & 1 \end{bmatrix} \mathbf{x} + \begin{bmatrix} 0 & 0 \\ 0 & 0 \end{bmatrix} \mathbf{u}, \tag{5.18}$$

with

$$\mathbf{x} = \begin{bmatrix} \omega_1 \\ \omega_2 \end{bmatrix} \tag{5.19}$$

and

$$\mathbf{u} = \begin{bmatrix} N_{m1} \\ N_{m2} \end{bmatrix}. \tag{5.20}$$

The system of Eqs. (5.17) to (5.20) can be discretized by

$$\mathbf{\Phi} = e^{FT_s} \tag{5.21}$$

and

$$\mathbf{\Gamma} = \int_0^{T_s} e^{F\eta} \, \mathrm{d}\eta \, \mathbf{G}, \tag{5.22}$$

to yield the discrete state space representation

$$\mathbf{x}(k+1) = \mathbf{\Phi}\mathbf{x}(k) + \mathbf{\Gamma}\mathbf{u}(k) \tag{5.23}$$

$$\mathbf{y}(k) = \mathbf{H}\mathbf{x}(k) + \mathbf{J}\mathbf{u}(k). \tag{5.24}$$

The state equations do not account for static or coulomb friction and therefore integral control will be added to the system to ensure zero steady state errors. The state-space model, augmented with an integral state for each output and including

a reference input, is

$$\begin{bmatrix} \mathbf{x}_I(k+1) \\ \mathbf{x}(k+1) \end{bmatrix} = \begin{bmatrix} \mathbf{I} & \mathbf{H} \\ \mathbf{0} & \mathbf{\Phi} \end{bmatrix} \begin{bmatrix} \mathbf{x}_I(k) \\ \mathbf{x}(k) \end{bmatrix} + \begin{bmatrix} \mathbf{0} \\ \mathbf{\Gamma} \end{bmatrix} \mathbf{u}(k) - \mathbf{\Gamma}_r \mathbf{r}(k) \tag{5.25}$$

$$\mathbf{y}(k) = \begin{bmatrix} \mathbf{0} & \mathbf{H} \end{bmatrix} \begin{bmatrix} \mathbf{x}_I(k) \\ \mathbf{x}(k) \end{bmatrix}. \tag{5.26}$$

where $\mathbf{r}(k) = \left[\begin{smallmatrix} \omega_{1_{ref}} \\ \omega_{2_{ref}} \end{smallmatrix}\right]$ are the reference inputs and $\mathbf{\Gamma}_r = \left[\begin{smallmatrix} \mathbf{I} \\ \mathbf{0} \end{smallmatrix}\right]$ is the reference input matrix. The augmented state matrix, input matrix and output matrix will be denoted $\mathbf{\Phi}_I$, $\mathbf{\Gamma}_I$ and $\boldsymbol{H}_I$ respectively. The control law to be used is

$$\mathbf{u}(k) = -\mathbf{K}\mathbf{x}(k), \tag{5.27}$$

which for a full state feedback controller with integral control and a reference input becomes

$$\mathbf{u}(k) = -\begin{bmatrix} \mathbf{K}_I & \mathbf{K} \end{bmatrix} \begin{bmatrix} \mathbf{x}_I(k) \\ \mathbf{x}(k) \end{bmatrix} + \mathbf{K}\mathbf{N}_x \mathbf{r}(k), \tag{5.28}$$

where $\mathbf{N}_x$ is the state command matrix, which for this system is $\mathbf{N}_x = \left[\begin{smallmatrix} 1 & 0 \\ 0 & 1 \end{smallmatrix}\right]$ due to the particular selection of the state matrices. The closed loop system, illustrated in Fig. 5.2, in state space form is

$$\begin{bmatrix} \mathbf{x}_I(k+1) \\ \mathbf{x}(k+1) \end{bmatrix} = \left(\mathbf{\Phi}_I - \mathbf{\Gamma}_I \begin{bmatrix} \mathbf{K}_I \\ \mathbf{K} \end{bmatrix} \right) \begin{bmatrix} \mathbf{x}_I(k) \\ \mathbf{x}(k) \end{bmatrix} + \mathbf{\Gamma}_r \mathbf{r} \tag{5.29}$$

$$\mathbf{y}(k) = \mathbf{H}_I \begin{bmatrix} \mathbf{x}_I(k) \\ \mathbf{x}(k) \end{bmatrix}. \tag{5.30}$$

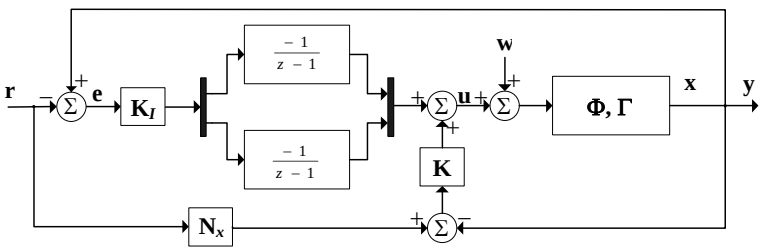

Figure 5.2: Block diagram of full-state feedback controller with integral control and reference and disturbance inputs **r** and **w**

5.2.3 Controllability

From the open loop measurements in Chapter 4, it is clear that all the states can be controlled by the two available inputs, and intuitively the system is controllable. This can be verified mathematically by testing that the controllability matrix, defined as

$$\mathcal{C} = \begin{bmatrix} \mathbf{\Gamma} & \mathbf{\Phi\Gamma} & \cdots & \mathbf{\Phi}^{n-1}\mathbf{\Gamma} \end{bmatrix} \tag{5.31}$$

is non-singular. The rank of $\mathcal{C}$ must be n for the matrix to be non-singular, where n is the size of $\mathbf{\Phi}$ and thus the number of poles that has to be placed. Substituting the state equations at $\phi_G = 0$rad into Eq. (5.31) yields

$$\mathcal{C} = \begin{bmatrix} 2180 & 0 & -1900.96 & 5438.446 \\ 0 & 1900 & -5438.446 & -1444 \end{bmatrix} \tag{5.32}$$

which has a rank of 2. The system was found to be controllable for the region of interest $-25° < \phi_G < 25°$.

5.2.4 Controller Design Methods

The performance of two methods to determine the gain matrix $[\mathbf{\kappa}_I \ \mathbf{\kappa}]$ in the full state feedback controller for the platform were investigated, namely pole placement and LQR optimal control [2]. These methods are discussed in the following sections.

Pole Placement

With the control law as in Eq. (5.27), the closed loop poles of the system $[\mathbf{\Phi} - \mathbf{\Gamma K}]$ are given by the roots of the characteristic equation

$$|z\mathbf{I} - \mathbf{\Phi} + \mathbf{\Gamma K}| = 0. \tag{5.33}$$

By selecting a set of closed loop poles $(p_1, p_2, \ldots, p_n)$ which will yield a desired system response, the feedback gain matrix $\mathbf{K}$ that realize these poles can be calculated by solving for K in the equation

$$|z\mathbf{I} - \mathbf{\Phi} + \mathbf{\Gamma K}| = (z - p_1)(z - p_2)\ldots(z - p_n). \tag{5.34}$$

For a MIMO system, the resulting gain matrix is not unique. The MATLAB function `place.m` handles the extra degrees of freedom and calculates a feedback

gain that minimizes the sensitivity of the closed-loop poles to perturbations in $\mathbf{\Phi}$ or $\mathbf{\Gamma}$[1].

Steady State Optimal Control

The optimal linear quadratic regaluator (LQR) control method calculates the values of $\mathbf{K}$ in the control law of Eq. (5.27) in such a manner as to minimise the cost function

$$\mathcal{J} = \frac{1}{2} \lim_{n\to\infty} \sum_{k=0}^{n} \left[\mathbf{x}^T(k)\mathbf{Q}_1\mathbf{x}(k) + \mathbf{u}^T(k)\mathbf{Q}_2\mathbf{u}(k)\right]. \tag{5.35}$$

The focus of the design is shifted from iterating on closed loop pole positions to assigning weights in a cost function to produce the desired closed loop response. The selection of the weighting matrices $\mathbf{Q}_1$ and $\mathbf{Q}_2$ is only weakly connected to the closed loop performance specifications and therefore the elements of these matrices are determined by an iterative process. However, a degree of control over the settling time can be obtained through the Pincer Procedure [2] which introduces another parameter, α, into the problem. With

$$\mathbf{z}(k) = \alpha^k \mathbf{x}(k) \text{ and } \mathbf{v}(k) = \alpha^k \mathbf{u}(k), \tag{5.36}$$

the modified performance criterion is

$$\mathcal{J}_\alpha = \lim_{n\to\infty} \sum_{k=0}^{n} \left[\mathbf{x}^T(k)\mathbf{Q}_1\mathbf{x}(k) + \mathbf{u}^T(k)\mathbf{Q}_2\mathbf{u}(k)\right]\alpha^{2k} \tag{5.37}$$

$$= \lim_{n\to\infty} \sum_{k=0}^{n} \left[\mathbf{z}^T\mathbf{Q}_1\mathbf{z} + \mathbf{v}^T\mathbf{Q}_2\mathbf{v}\right] \tag{5.38}$$

and the state equations become

$$\mathbf{z}(k+1) = \alpha\mathbf{\Phi}\mathbf{z}(k) + \alpha\mathbf{\Gamma}\mathbf{v}(k). \tag{5.39}$$

If α is selected as

$$\alpha > 100^{1/k} = 100^{T_s/t_s}, \tag{5.40}$$

all states should settle to less than 1% within the specified settling time t_s.

[1] See Kautsky, J. and Nichols N.K., "Robust Pole Assignment in Linear State Feedback", Int. J. Control, 41 (1985), pp. 1129-1155.

The MATLAB function `dlqr.m` was used to calculates the gain matrices $\mathbf{K}$ and $\mathbf{K}_I$.

Gain Scheduling

It is clear from Eq. (5.16) that the model is dependent on the selection of the operating point in ϕ_{G_0}. Both controllers will initially be designed and tested at $\phi_{G_0} = 0°$. The adaptive control method of gain scheduling will then be implemented on the controller with the best results in order to enable the controller to track reference inputs at all allowable values of ϕ_G. The control scheme is illustrated in Fig. 5.3. The state matrix F will be calculated at predefined values of ϕ_G and

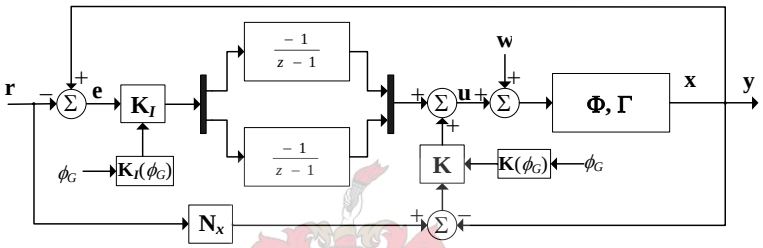

Figure 5.3: Block diagram of the gain scheduling controller

discretized with the MATLAB function `c2d.m`. The resulting discrete state and input matrices will be used in the calculation of $[\mathbf{K}_I\ \mathbf{K}]$ to generate an array of gain matrices. The appropriate gains in $[\mathbf{K}_I\ \mathbf{K}]$ can then be selected as a function of ϕ_G at each sample instance.

Gain scheduling will not introduce stability issues since the change in model and feedback gains will be very small over one sample period, as will be seen in the following sections.

5.2.5 Pole Placement Controller Design

To achieve good control effort (i.e. meet the design specifications with as little control as possible), the four poles of the system will be placed according to a fourth order Butterworth filter distribution [13]. The closed-loop poles of the Butterworth filter are equally spaced in the left hand side of the s-plane on a constant ω_n radius and has an effective damping factor of $\zeta_{eff} = 0.707$. The filter cut-off frequency is selected as 0.63 Hz. This will ensure that the bandwidth and rise time specifications of the

closed-loop system are met and that the system's resonance frequencies will not be stimulated by the controller. The resulting poles in the z-plane for $\phi_{G_0} = 0°$ are

$$\begin{aligned} z_{1,2} &= 0.9312 + 0.1372j \\ z_{I1,2} &= 0.8760 + 0.0817j. \end{aligned} \tag{5.41}$$

The gain matrices are calculated as

$$\begin{bmatrix} \mathbf{K_I} & \mathbf{K} \end{bmatrix} = \begin{bmatrix} 0.002725 & -0.001186 & -0.018498 & 0.089157 \\ 0.001444 & 0.002646 & -0.104939 & 0.032215 \end{bmatrix}. \tag{5.42}$$

Fig. 5.4 shows the bode diagram of the closed loop system. A reference command to $\omega_{1_{ref}}$ will pass through to output ω_1, while the magnitude of ω_2 for the same reference input will be damped at low frequencies. The same holds for input $\omega_{2_{ref}}$ to outputs ω_2 and ω_1, verifying that the general working of the controller is correct. The $-3\,\text{dB}$ cut-off is at approximately $0.5\,\text{Hz}$ and a roll-off of $40\,\text{dB/dec}$ can be observed for $\omega_{1_{ref}}$ to ω_1 and $\omega_{2_{ref}}$ to ω_2.

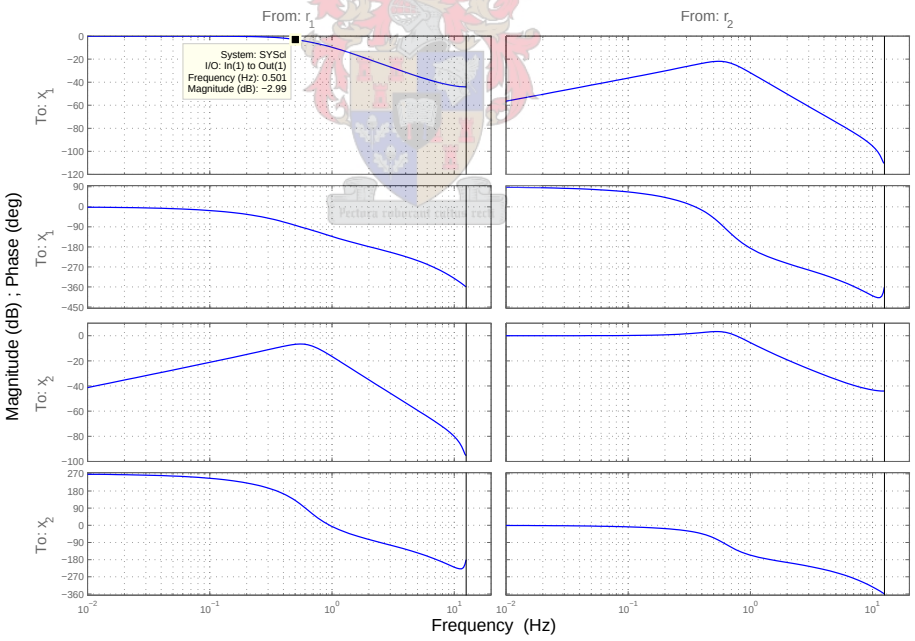

Figure 5.4: Closed loop bode diagram of input **r** to output **y**

The simulated response to a step command in $\omega_{2_{ref}}$ is shown in Fig. 5.5. The settling time is less than $2\,\text{s}$ with no overshoot in ω_2. A steady state error in ϕ_G

of 1.69° results due to unwanted excitation of ω_1 in the transient phase. The RMS tracking error in θ_G is 1.8947°.

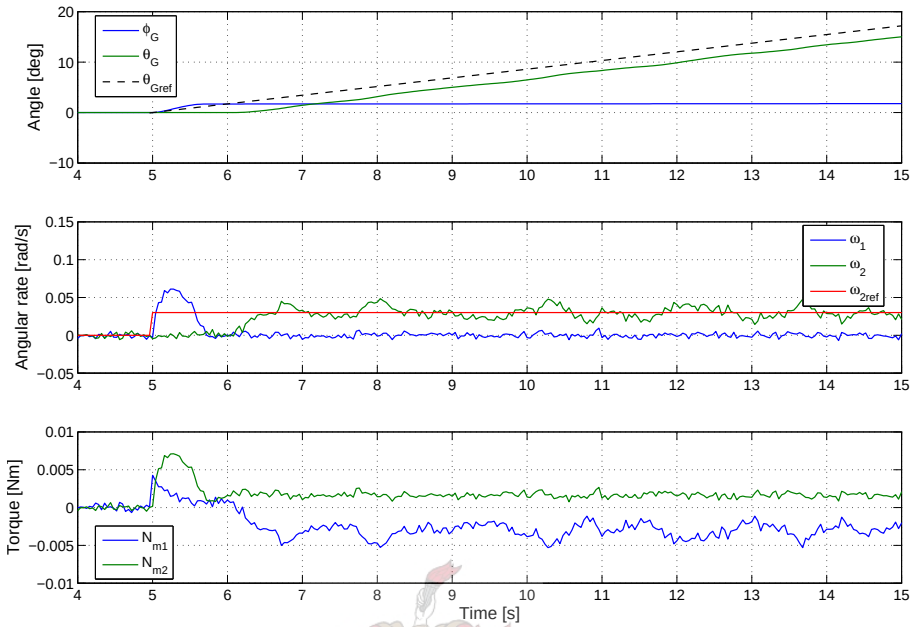

Figure 5.5: Simulated step response of controller designed by pole placement for a step in $\omega_{2ref} = 0.03$rad/s

5.2.6 LQR Controller Design

To obtain the desired response and system bandwidth as discussed in Section 5.2.1, the Pincer settling time is chosen as $t_s = 4$s. The actual 2 s specification will be enforced by the selection of $\mathbf{Q}_1$ in order to provide more flexibility in the resulting pole locations. From Eq. (5.40), α is calculated as

$$\alpha = 1.04713. \tag{5.43}$$

$\mathbf{Q}_1$ and $\mathbf{Q_2}$ are selected as

$$\mathbf{Q}_1 = \begin{bmatrix} q_i & 0 & 0 & 0 \\ 0 & q_i & 0 & 0 \\ 0 & 0 & q & 0 \\ 0 & 0 & 0 & q \end{bmatrix} \tag{5.44}$$

$$\mathbf{Q}_2 = \begin{bmatrix} \frac{1}{u_{11}^2} & 0 \\ 0 & \frac{1}{u_{22}^2} \end{bmatrix}, \tag{5.45}$$

with $u_{11} = u_{22} = 10mNm$ (the maximum actuator authority). q_i and q are varied to obtain the desired closed loop response. The same weight is assigned to the respective states, since there is no classification of importance between the two system or integrator states. As a design tool, the root loci of the system and integrator poles, with $\phi_{G_0} = 0°$, are plotted as a function of the elements in $\mathbf{Q}_1$, which are illustrated in Fig. 5.6. For each separate locus, q is kept constant while the value of q_i is iterated from 10^{-5} to 10^5. The loci are plotted in different colours for different values of q. Table 5.1 contains the colour legend for the plot in Fig 5.6.

It can be seen that as q increases, the natural frequency and the damping factor of x_1 and x_2 increases. The weighting elements are selected as $q = 5$ and $q_i = 10^{-5}$. The resulting closed loop poles in the z-plane for $\phi_{G_0} = 0°$ are

$$\begin{aligned} z_{1,2} &= 0.4026 \pm 0.7335i \\ z_{I1,2} &= 0.9550 \pm 4.813452 \times 10^{-8}i. \end{aligned} \tag{5.46}$$

The integrator poles dominate the closed loop response and ensure that the settling time specification is met. Only a small amount of damping is added to the system poles, as damping with regard to a non-inertial reference can lead to instability in the physical implementation. This also reduces the controller's sensitivity to model parameter deviations.

It will be shown in Chapter 6 that the performance of the LQR controller exceeds that of the controller designed by pole placement. Gain scheduling will thus be implimented on the LQR controller. Fig. 5.7 illustrates the resulting gain elements as a function of ϕ_G. The gain matrices are implemented by means of second order

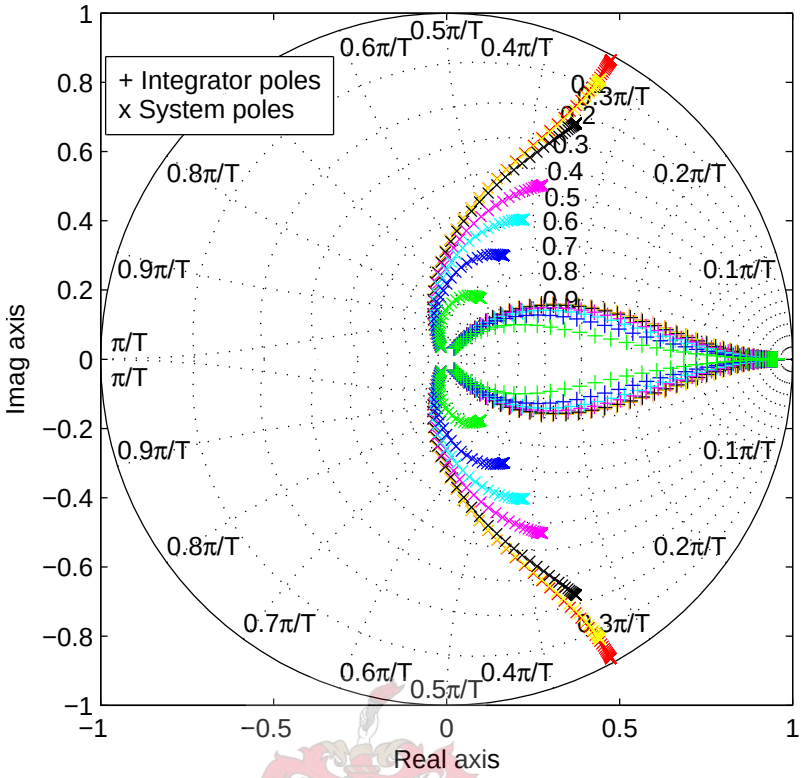

Figure 5.6: Root loci of elevation pointing system as a function of q_i and q

Table 5.1: Colour legend for Fig. 5.6

	Red	Yellow	Black	Magenta	Cyan	Blue	Green
q	0.001	1	10	50	100	200	500

polynomials, given by

$$
\begin{aligned}
K_{I11} &= 0.000242466\phi_G^2 + 0.002005259 \\
K_{I12} &= 0.005214423\phi_G^2 - 0.010493582 \\
K_{I21} &= 0.003702174\phi_G^2 + 0.028078711 \\
K_{I22} &= -0.002678747\phi_G^2 + 0.006185185 \\
K_{11} &= -0.005281990\phi_G^2 + 0.010618685 \\
K_{12} &= 0.000241618\phi_G^2 + 0.002034274 \\
K_{21} &= 0.001910840\phi_G^2 - 0.004763405 \\
K_{22} &= 0.003832059\phi_G^2 + 0.029751148,
\end{aligned}
$$

where ϕ_G is measured in radians.

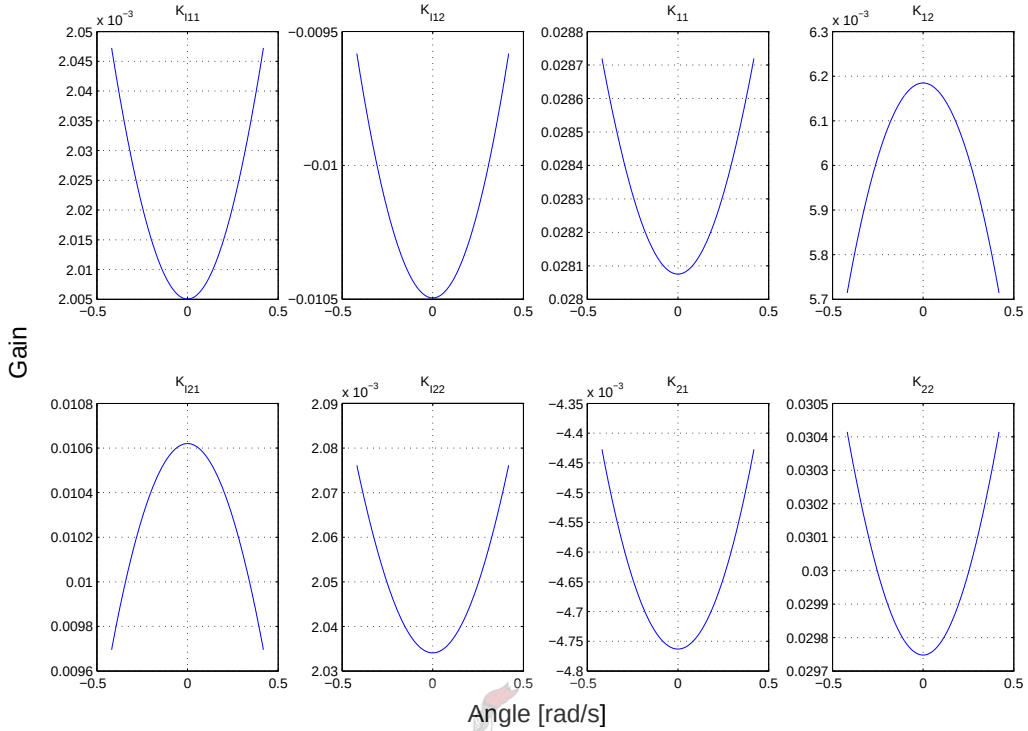

Figure 5.7: Gain elements as a function of ϕ_G for the LQR controller with gain scheduling

The implementation of gain scheduling lead to deviations from the closed loop poles of Eq. (5.46), since the weighting matrices remain constant when the gains are calculated as a function of ϕ_G. The locus of implemented poles are illustrated in Fig. 5.8. The change in system poles due to gain scheduling will not have a significant effect on the response of the system, since the integrator poles dominate the closed loop response. The integrator poles remain essentially the same as the gains change as a function of ϕ_G.

The simulated step responses for a reference step in ω_1 and ω_2 of 0.03 rad/s are shown in Figs. 5.9 and 5.10 respectively. The settling times are well within the specified limit of less than 2 s for steps in both $\omega_{1_{ref}}$ and $\omega_{2_{ref}}$. The RMS error in ϕ_G is calculated as 0.9923° and in θ_G as 0.9624°. This is a reduction in tracking errors of 50 % over the controller designed using pole placement.

5.3 Azimuth Controller

The specifications set for the elevation controller also apply to the azimuth controller. The specifiations are:

- Rise time of under 2 s

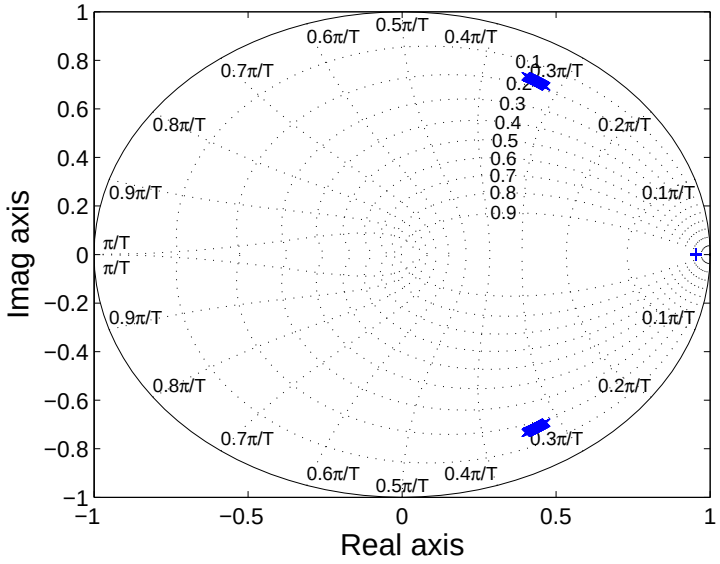

Figure 5.8: Closed loop pole perturbations for LQR controller with gain scheduling

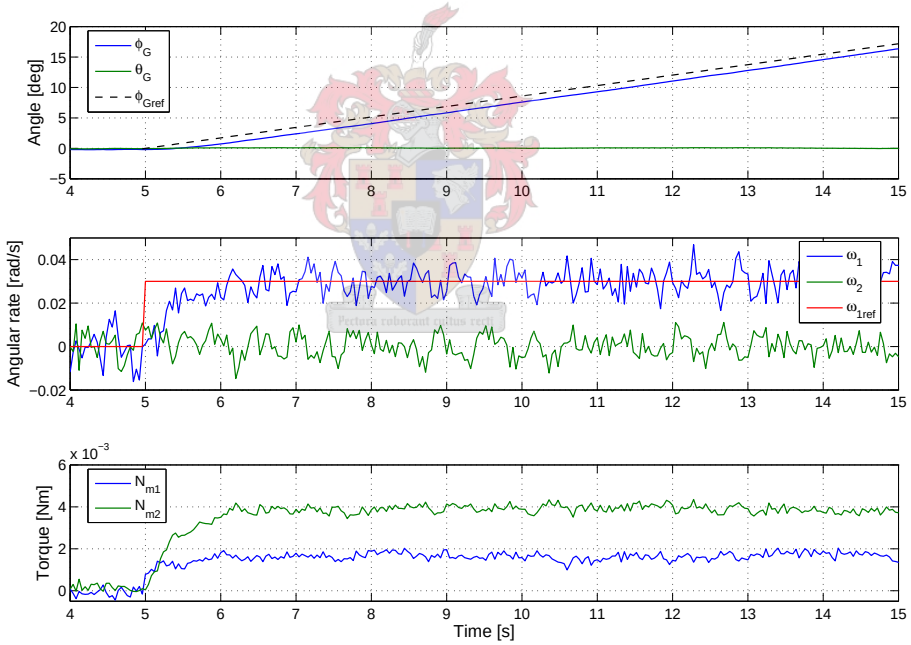

Figure 5.9: Simulated step response of LQR controller for a step in $\omega_{1ref} = 0.03$rad/s

- Overshoot of less than 10 %
- Zero steady state error
- Be able to track angular rates of 0.025 rad/s without affecting ϕ_G or θ_G

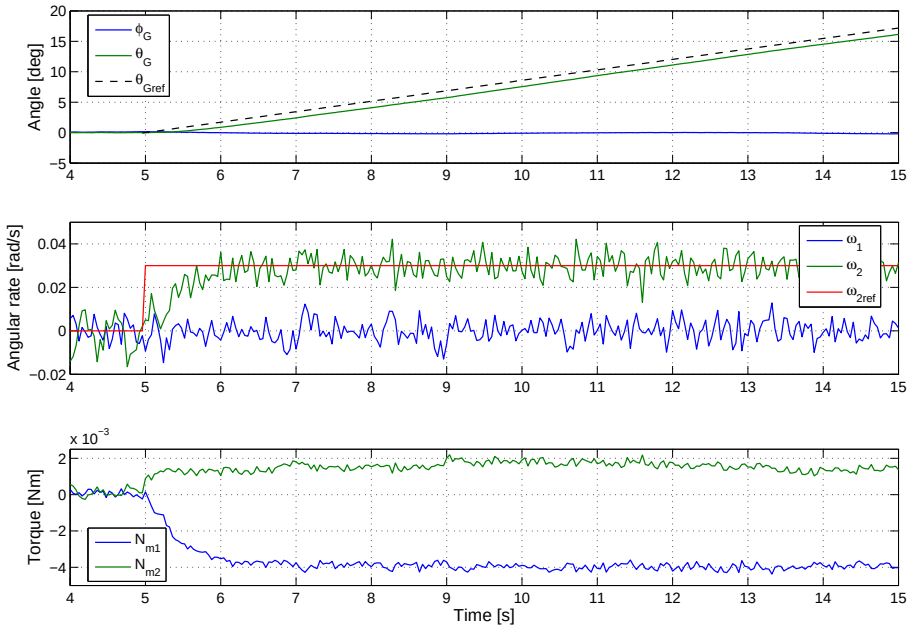

Figure 5.10: Simulated step response of LQR controller for a step in $\omega_{2ref} = 0.03$rad/s

A sampling time of 0.04 s, as was determined fit for the elevation controller, will also be used for the azimuth controller. A simple first order PI controller will be implimented on the outer gimbal to control platform motion in the azimuth plane. This will ensure zero steady state error in the presence of unmodelled non-linear dynamics, e.g. static and coulomb friction.

The motion of the third gimbal, decoupled gyroscopically from gimbals 1 and 2, is described by Eq. (4.3) with $\omega_1 = \omega_2 = 0$rad/s. That is,

$$I_{33}\dot{\omega}_3 = N_3 + k_{w3}\omega_3. \tag{5.47}$$

Taking the Laplace transform of Eq. (5.47), yields the transfer function of the plant as

$$G_3(s) = \frac{\Omega_3}{N_3} = \frac{1}{I_{33}s + k_{w3}}, \tag{5.48}$$

with $I_{33} = 7.14 \times 10^{-3}$kg·m^2 and $k_{w3} = 4.5 \times 10^{-3}$N/m·s^{-1}. Discretizing Eq. (5.48) using the method of zero-order hold equivalents for a sampling period of $T_s = 0.04$s, yield the discrete transfer function of the plant as

$$\begin{aligned} G_3(z) &= (1 - z^{-1})\, \mathcal{Z}\left\{\frac{G_3(s)}{s}\right\} \\ &= \frac{5.53}{z - 0.9751}. \end{aligned} \tag{5.49}$$

Designing for a 1 % settling time of $t_s = 2$s with optimal damping, i.e. $\zeta = 0.707$, the desired closed loop poles in the s-domain are

$$s_{1,2} = -2.3 \pm 2.301j, \tag{5.50}$$

which translates to the z-domain through $z = e^{sT_s}$ as

$$z_{1,2} = 0.9082 \pm 0.0838j. \tag{5.51}$$

These poles can be realized with a discrete PI controller, of which the transfer function is given by

$$D(z) = K_D \frac{z-a}{z-1}. \tag{5.52}$$

The control scheme is illustrated in Fig. 5.11. Using the method of discrete root

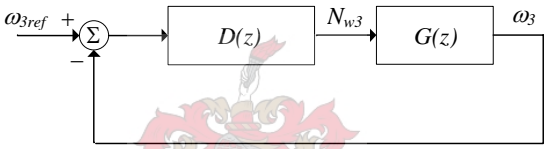

Figure 5.11: Block diagram of closed loop system for control in the azimuth plane

locus design [2], the values of K_D and a that realize the poles given in Eq. (5.51) were calculated as

$$K_D = 0.0286$$

and

$$a = 0.9029.$$

The root locus of the system is illustrated in Fig. 5.12.

The simulated step response for a step in ω_3 of 0.025 rad/s is illustrated in Fig. 5.13. The system satisfies the settling time specification of $t_s = 2$s, with no visible overshoot. The RMS angle tracking error is calculated as 1.61 °.

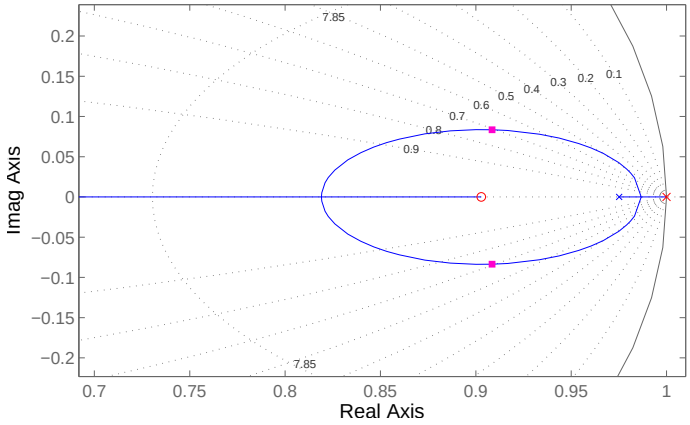

Figure 5.12: Root locus of system responsible for azimuth pointing

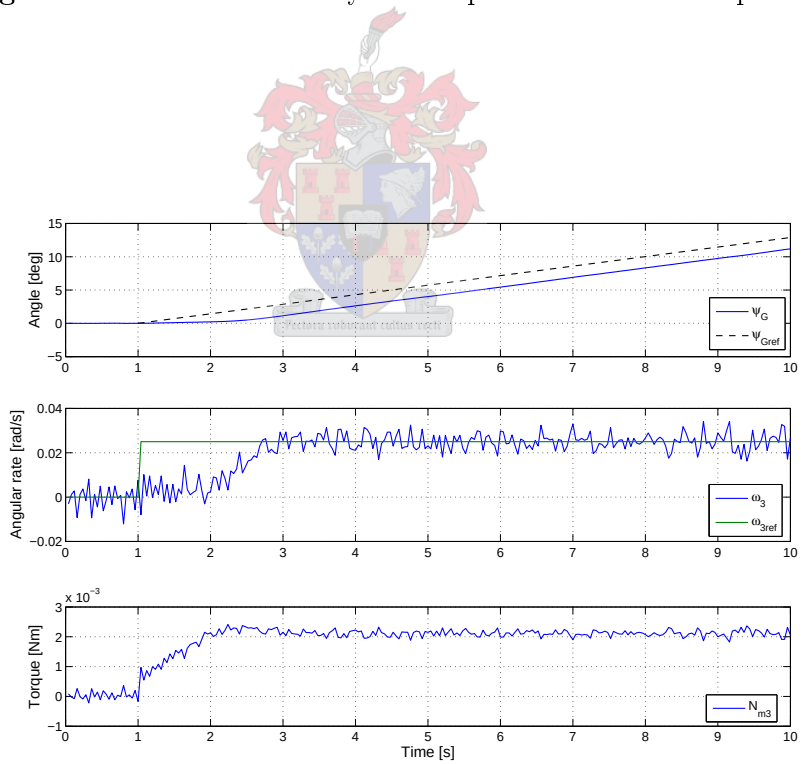

Figure 5.13: Simulated step response of PI controller for a step in $\omega_{3ref} = 0.025$rad/s

Chapter 6

Results

This chapter provides system output measurements of controller tests performed on the ground. The controllers' steering performance is evaluated under base-stationary conditions. Also presented are simulation results stating the performance of the controllers when subjected to external disturbance torques. Finally, conclusions are drawn from the results obtained.

6.1 Elevation Controller

6.1.1 Pole Placement Controller Results

Fig. 6.1 shows the response to a step command of 0.03 rad/s in $\omega_{2_{ref}}$. The system enters a stable limit cycle as a result of the step command due to the non-linearities in the plant, which are mainly static and coulomb friction that is not accounted for in the model. It was found that the oscillations can be eliminated by reducing the feedback gains in $\mathbf{K}$ by a factor of 0.2 . As a result, less control effort is applied in moving the system poles, causing the dynamics of the integrator poles to dominate the response. The resulting pole locations are

$$z_{1,2} = 0.5479 \pm 0.7105i$$
$$z_{I1,2} = 0.9860 \pm 0.02319i.$$

Upon closer inspection, the frequency of the limit cycle was found to be approximately 0.67 Hz. This frequency is filtered by the modified closed loop system, evident from the bode plot in Fig. 6.2, which also indicates that the modified system does

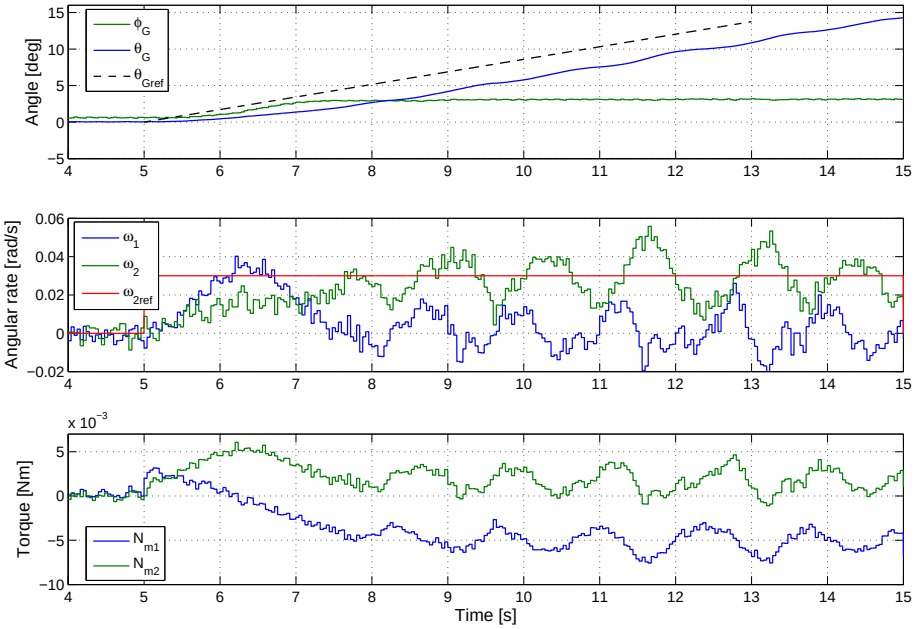

Figure 6.1: Measured step response of elevation controller (pole placement) for a step in $\omega_{2ref} = 0.03$rad/s

not meet the bandwidth specification of 1.6 rad/s.

Fig. 6.3 shows the modified system's response to a step command of 0.03 rad/s in $\omega_{2_{ref}}$. The limit cycle is eliminated but neither the settling time nor the overshoot specifications are met. This is a practical trade-off in the pole placement controller. The RMS tracking error in θ_G, calculated for the first 7 s after the step command was issued, increased from 2.3811 ° to 3.0016 ° even though the steady state response has improved. The larger RMS error is mainly due to the larger DC component in the tracking error which is caused by the modified system's degraded transient response to a step command.

Although controller tuning is often necessary in practical systems, it is difficult to predict the resulting pole locations when feedback gains are arbitrarily modified. Closed loop poles are not placed according to certain specifications and the method of pole placement loses its design power. For the problem at hand, factors in the practical system prevented the effective implementation of a controller based on pole placement. However, a better understanding of the system in terms of allowable closed loop pole locations and order of feedback gains were obtained. This knowledge proved very useful in finding a robust solution for the LQR controller.

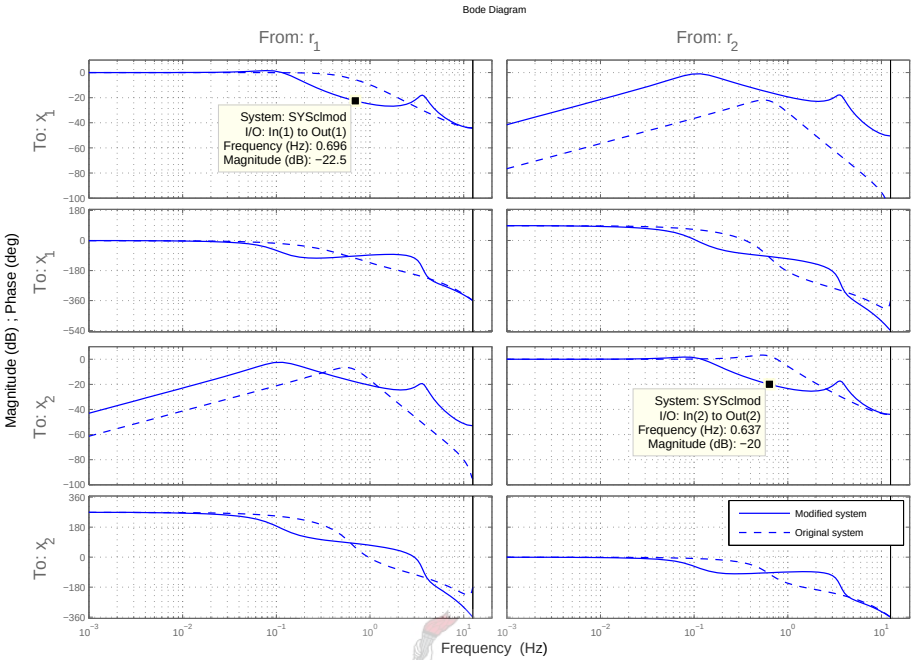

Figure 6.2: Closed-loop bode diagram of input **r** to output **y**

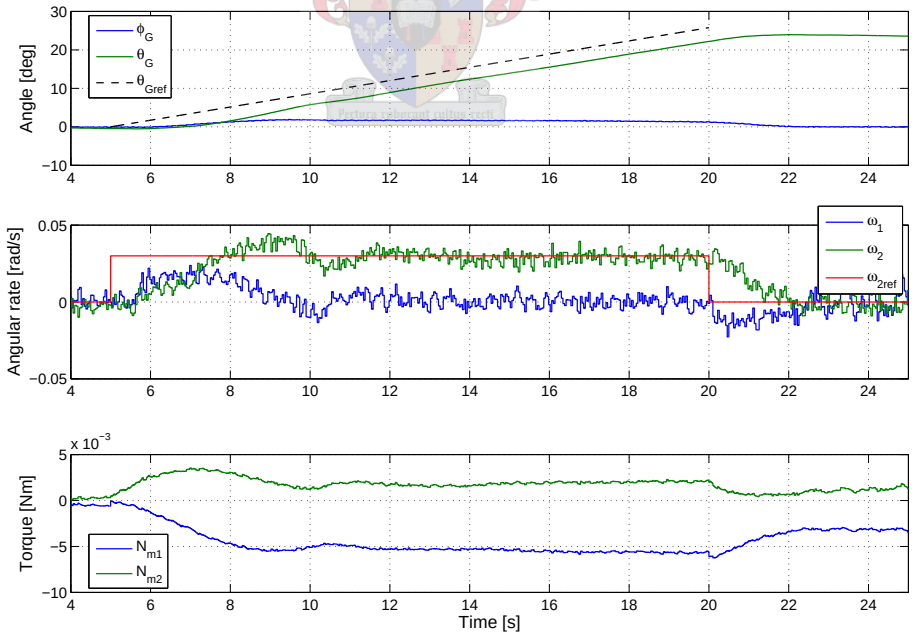

Figure 6.3: Measured step response of modified elevation controller (pole placement) for a step in $\omega_{2ref} = 0.03$rad/s

6.1.2 LQR Controller Results

The measured step response for a reference step in ω_1 and ω_2 of 0.03 rad/s are shown in Figs. 6.4 and 6.5 respectively. A 0.5 s delay in the response due to a step in $\omega_{1_{ref}}$ and $\omega_{2_{ref}}$ can be observed. The delay is due to static and coulomb friction that have to be overcome by the integral action of the controller. The settling times are less than 2 s for a step in both $\omega_{1_{ref}}$ and $\omega_{2_{ref}}$. The reference angular velocities are tracked with zero steady state error. The measured RMS angle tracking errors are 1.4292° in ϕ_G due to a step in $\omega_{1_{ref}}$ and 1.5092° in θ_G due to a step in $\omega_{2_{ref}}$, measured over the first 7 s after the step commands are given. This is more than was observed in simulation and can be accounted for by the slightly slower transient response caused by the delay of the physical system.

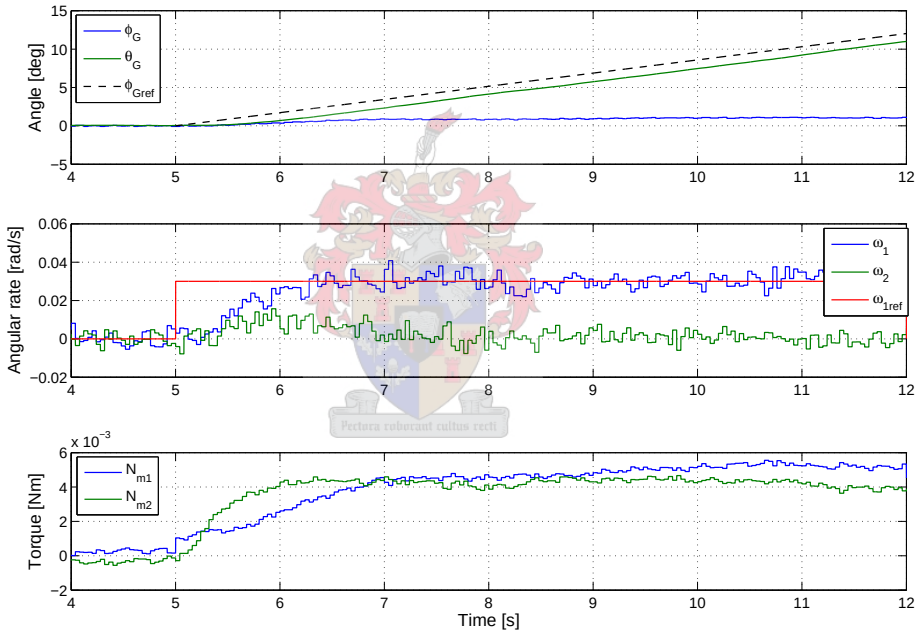

Figure 6.4: Measured step response of LQR controller for a step in $\omega_{1ref} = 0.03$rad/s

Fig. 6.6 shows the response to a step command in $\omega_{2_{ref}}$ of 0.03 rad/s with ϕ_G at an offset angle of −8°. The response satisfies the specifications and illustrates the working order of the gain scheduling component of the controller, along with Fig. 6.4.

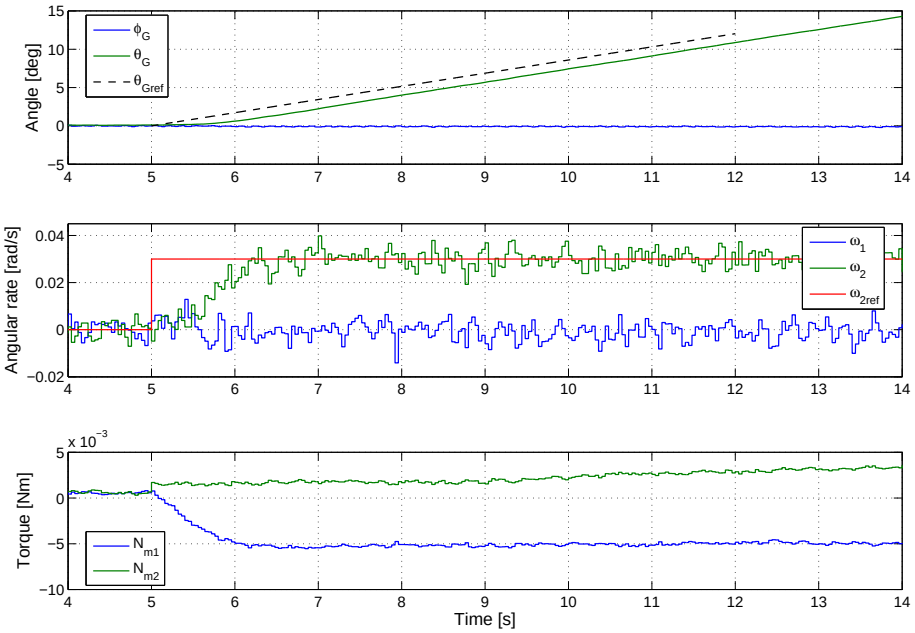

Figure 6.5: Measured step response of LQR controller for a step in $\omega_{2ref} = 0.03$rad/s

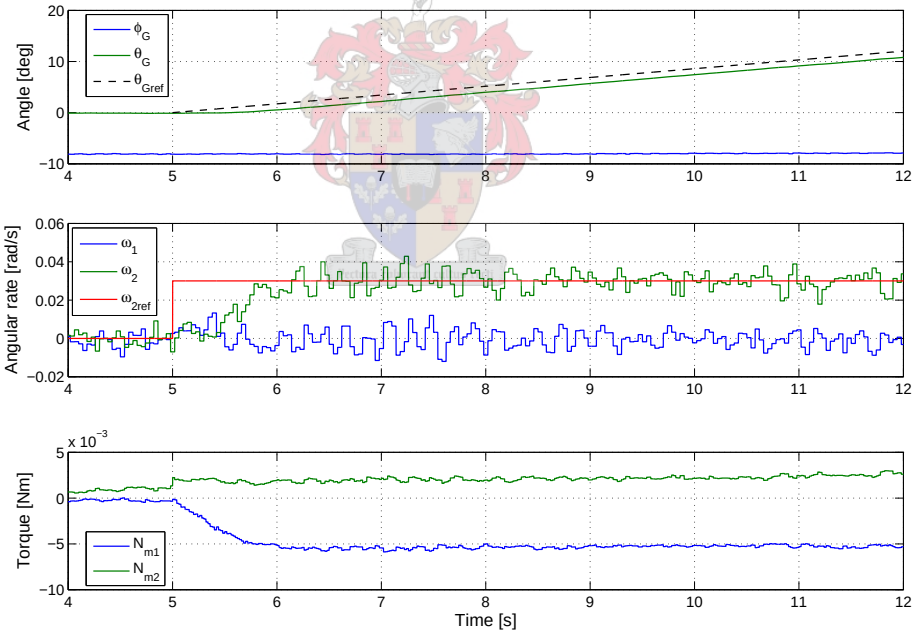

Figure 6.6: Measured step response of LQR controller for a step in $\omega_{2ref} = 0.03$rad/s with $\phi_G = -8°$

6.2 Azimuth Controller

The measured step responses for a step command in $\omega_{3_{ref}}$ of 0.025 rad/s are shown in Fig. 6.7 for $\theta_G \approx 0°$ and in Fig. 6.8 for $\theta_G \approx 35°$. All the specifications are

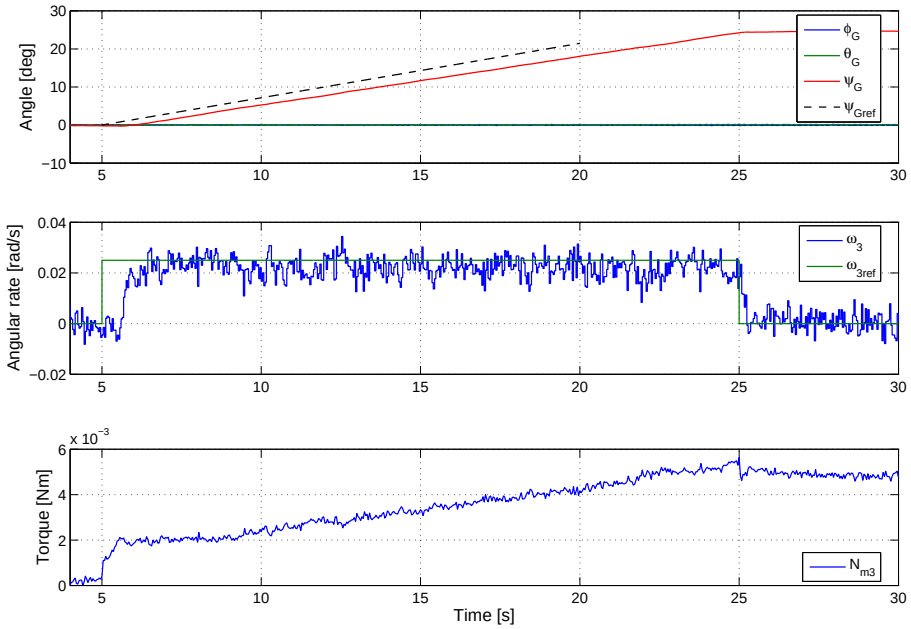

Figure 6.7: Measured step response of azimuth controller for a step in $\omega_{3ref} = 0.025$rad/s with $\phi_G = \theta_G = 0°$

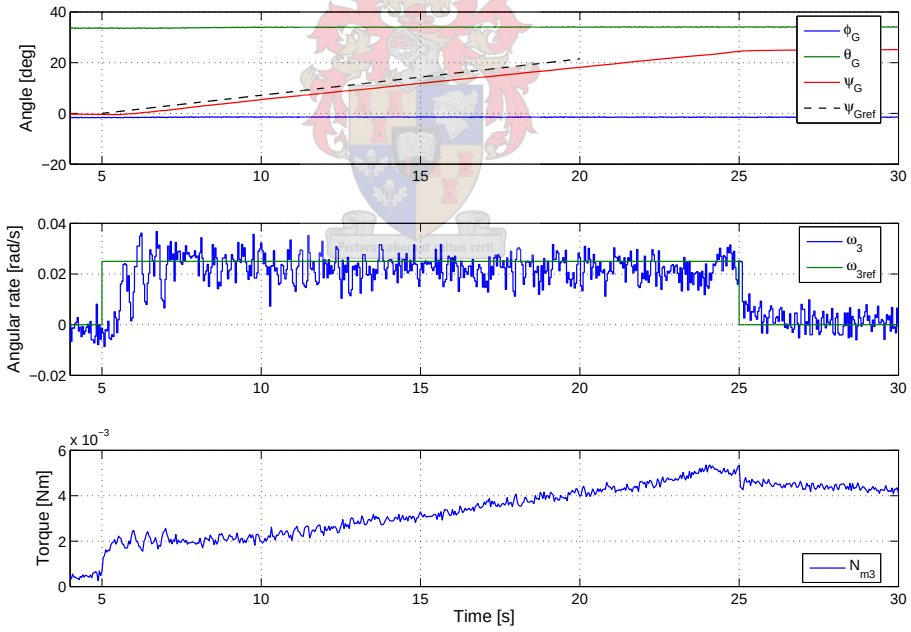

Figure 6.8: Measured step response of azimuth controller for a step in $\omega_{3ref} = 0.025$rad/s with $\phi_G = -4°$ and $\theta_G = 33.6°$

met for the case $\phi_G = \theta_G = 0°$. A settling time of less than 2 s and negligible overshoot can be observed. Fig. 6.8 indicates that the transient response degrades slightly as the elevation angle decreases. This is mainly due the assumption that the moment of inertia of each gimbal is spherical, which is not the case in the practical

implementation. The worst case settling time was measured as approximately 2.1s, which is still acceptable, since the steering performance in the steady state will not be influenced by the slightly slower settling time. ϕ_G and θ_G are not influenced when the platform is steered in the azimuth plane.

6.3 Disturbance Rejection

Fig. 6.9 shows the simulated stabilising performance of the combined azimuth and elevation controllers in the presence of disturbance torques due to airship rotations. The RMS errors in azimuth and elevation pointing has decreased to 0.2703° and 0.4248° respectively. The boresight drift that was observed in simulations of the open loop system over a period of 360 s, has been eliminated with the controllers active.

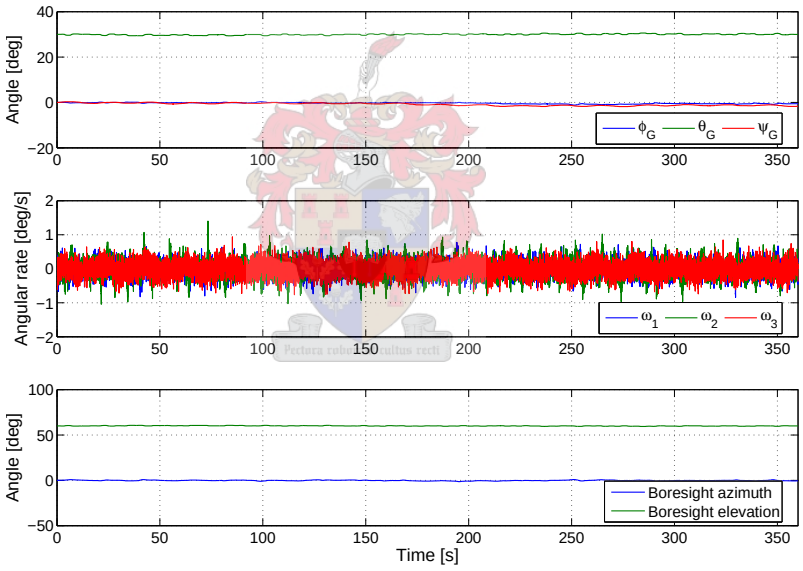

Figure 6.9: Simulated effect of airship movement on platform due to viscous friction with azimuth and elevation stabilising controllers

6.4 Conclusions

To further improve the pointing resolution of the platform in the presence of disturbance torques, the settling time specification of 2 s can be decreased. However, it is difficult to find a robust practical solution with faster response times. A MIMO controller implementing the full set of differential equations that describe the motion

of the gyroscope should also increase the performance of platform in the presence of disturbance torques.

6.4.1 Elevation controller

The closed loop system designed by the method of pole placement was found to be very sensitive to the amount of control applied to the system poles. A number of different pole locations that satisfy the specifications were tested, of which the best solution was presented here. Other methods tried include radial projection, where the system poles' damping factor is increased while the natural frequency is kept constant, leaving the placement of the integrator poles to achieve the desired system response. Butterworth configurations at several different frequencies with and without modified damping ratios were also investigated, without obtaining better results. This indicates that robust pole placement in MIMO higher order systems, with uncertainties in the locally linearised model as well as unmodelled non-linearities, is not an easy task. However, insight into the behaviour of the plant was obtained. When the model uncertainties lie within known bounds, methods like pole colouring [10], adapted and simplified for the discrete case in [11], can be used. These methods provide a graphical aid in determining the closed-loop pole variations. The effect of the non-linearities can be investigated by means of describing functions analysis of the system [2]. We, however, reverted to the method of optimal LQR control to find a robust solution.

The method of LQR control provided a solution which demonstrated good regulation in the presence of disturbance torques and low sensitivity to model uncertainties. The LQR controller can be declared robust in the light of the results obtained from measurements and simulations. The controller developed by LQR optimal control was implemented on the ground station in Borland C++, discussed in Section 3.5.2, as the elevation control part of the main controller.

In all cases where satisfactory control results were obtained for the elevation pointing system, the integrator poles dominated the response and the system poles were kept close to their original positions. Large deviations from these positions led to instability in the physical system. In addition to the unmodelled non-linearities, the instability is caused by the fact that damping of the nutational modes of the gyroscope is attempted with regard to a non-inertial reference, i.e. the middle and outer gimbals [8].

6.4.2 Azimuth controller

Satisfactory results were obtained from the PI controller developed in Section 5.3 for azimuth control and regulation. The difference equation resulting from Eq. 5.52 was implemented in the ground station as the azimuth control part of the main controller.

Chapter 7

Recommendations and Conclusions

7.1 Recommendations for Future Work

Some work still needs to be done before the platform can be effectively deployed on an airship.

- The current electronics layout was designed to interface with a Cygnal development board. The electronics layout can be redesigned to include the microprocessor, servodrives and IMU in a more compact and lightweight configuration. It should be noted that the gyroscope needs to be rebalanced when alterations are made to the platform payload. Slip rings should also be installed between gimbal 2 and 3, since the wires degrade the practical performance of the platform in the current system.

- The controllers can be modified to include the AHRS measurements as feedback signals. This will allow absolute regulation of the boresight pointing direction. Due to gyro drift, the current system relies on a human in the loop to obtain long term pointing stability.

- The Kalman filter developed in the AHRS project [12] can be augmented to include gyro bias estimation for the rate gyros onboard the platform. The angle measurements can be used as feedback for the estimation process. Gyro drift is causing unintended actuation of the platform in the current system.

- An LQG estimator can be implemented which estimates the states of the platform, taking into account the stochastic nature of the sensor measurements [2].

Using the estimated states in the full-state feedback controller, instead of the noisy measurements, will improve the performance of the controllers.

- For the development of the controllers in this thesis, it was assumed that the flywheel is already spinning at a constant predefined speed. When the flywheel is in spin-up (i.e. accelerating from 0 rpm to 3300 rpm), the change of angular momentum causes the gimbals to rotate. These unwanted rotations can be eliminated by implementing a spin-up controller on the outer gimbal which counteracts the torque generated by the flywheel in spin-up. This will allow for on demand activation and deactivation of the flywheel in mid flight. This will also provide control over the peak power consumption of the flywheel during spin-up.

7.2 Conclusions

By utilising the inherent inertial properties of a gyroscope, a 3-axis stabilised camera-platform for use in earth observation was developed. A motorised 3-DOF gyroscope, which serves as the stabilised platform maintaining a stable pointing reference in inertial space, was designed and built by the CMS at the University of Stellenbosch. The following tasks were successfully carried out in customising the gyroscope for this purpose:

- Servo drive electronics and control systems were developed to ensure correct actuation of the platform. The actuator dynamics were decoupled from the main control loop resulting in separate torque control systems for each gimbal motor, which were implemented as analogue circuits. A speed controller was designed and implemented to ensure that the flywheel maintains a constant angular velocity, which is one of the criteria for the successful operation of a gyroscope. An IMU and gimbal angle sensors were developed and implemented to provide measurements of the platform states.

- A mathematical model for the stabilised platform was developed from first principles. The model was verified and used to determine the behavior of the platform in simulation. It was found that for the gyroscope built in this project, the motion of the outer gimbal could be decoupled from the rest of the system at slow angular rates. Therefore, the main controller could be split into two parts, one controlling motion in the azimuth plane and another

controlling motion in the elevation plane. Some aspects of the physical system remain unmodelled, but great care was taken in the implementation to limit the sources of unmodelled dynamics.

- Controllers for steering the platform were designed and implemented based on a linearised mathematical model of the platform. Satisfactory results were obtained from the full-state feedback controller designed by the method of LQR optimal control for elevation pointing and from the PI controller designed for azimuth pointing. All the controller design specifications were met. It was shown in simulation that the controllers also provided good disturbance torque rejection.

- The steering system was integrated in a Borland C++ GUI program that communicates with the microcontroller onboard the platform. This allows a user to easily steer the platform from a remote location.

Comparing the capabilities of the platform developed in this thesis with commercially available platforms (refer to Tables 7.1 and 1.1), it can be concluded that the specifications of a stabilised platform for use on an airship, are less strict, which lead to a much more cost effective system design.

Table 7.1: Capabilities of platform developed in this thesis

Maximum steering rate[1]	Active control bandwidth	Gyroscopic stabilisation bandwidth	Field of view (Az/El)
1.7 °/s	1 Hz	55 Hz	±165 °/ ±40 ° biased at 90 °

[1] The maximum rotation rate will be higher, and can only be measured after integration with the airship AHRS.

List of References

[1] Franklin, G., Powell, J. and Emami-Naeini, A.: *Feedback Control of Dynamic Systems.* 4th edn. Prentice Hall, New Jersey, 2002.

[2] Franklin, G., Powell, J. and Workman, M.: *Digital Control of Dynamic Systems.* 3rd edn. Addison-Westley, California, 1998.

[3] Marion, J.B. and Thornton, S.T.: *Classical Dynamics of Particles and Systems.* 4th edn. Saunders College Publishing, Fort Worth, Philadelphia, 1995.

[4] Neamen, D.: *Electronic Circuit Analysis and Design.* 2nd edn. McGraw-Hill, Boston, 2001.

[5] Nilsson, J.W. and Riedel, S.A.: *Electric Circuits.* 6th edn. Prentice Hall, New Jersey, 1969.

[6] Scarborough, J.B.: *The Gyroscope: Theory and Applications.* Interscience Publishers, Inc., New York, 1958.

[7] Ed. by Wertz, J.R.: *Spacecraft Attitude Determination and Control.* Kluwer Academic Publishers, Londen, 1978.

[8] Wrigley, W., Hollister, W.M. and Denhard, W.G.: *Gyroscopic Theory, Design and Instrumentation.* The M.I.T. Press, Cambridge, Massachusetts, 1969.

[9] Chingcuanco, A.O.: *Modelling and Control of a Balloon Borne Stabilized Platform.* Ph.D. thesis, University of California, Berkeley, 1989.

[10] Söylemez, M. and Munro, M.: Robust pole assignment in uncertain systems. In: *IEE Proceedings on Control Theory and Applications*, vol. 144, no. 3. May 1997.

[11] Botto, M., Babuška, R. and da Costa, J.: Discrete-time robust pole-placement design through global optimization. In Preprints 15th IFAC World Congress, pages T-Tu-M21, paper no. 2083, July 2002.

[12] Bijker, J.: *Development of an Attitude Heading Reference System for an Air ship*. Master's thesis, University of Stellenbosch, Stellenbosch, 2006.

[13] Steyn, W.H.: Advanced Digital Control Systems 813 class notes, 2005. University of Stellenbosch.

[14] Regan, T.: A DMOS 3A, 55V, H-Bridge: The LMD18200. Application Note 694, National Semiconductor, 1999.

[15] National Semiconductor: LMD18200 3A, 55V H-Bridge. Datasheet, 1998.

[16] Texas Instruments: Advanced Regulating Pulse Width Modulators. Datasheet, 1999.

[17] Analog Devices: ADXRS401. Datasheet Rev. 0, 2004.

[18] Analog Devices: ADXL103/ADXL203. Datasheet Rev. 0, 2004.

[19] Cygnal Integrated Products, Inc.: Improving ADC resolution by oversampling and averaging. Application Note AN18, May 2001.

[20] Olsen, J.: Remote sensing from air and space, 2005.
Available at: `http://www.physics.nps.navy.mil/00_Remote_Sensing_from_Air_and_Space.pdf`

[21] Canada Centre for Remote Sensing: Fundamentals of remote sensing, 2006.
Available at: `http://ccrs.nrcan.gc.ca/resource/tutor/fundam/pdf/fundamentals_e.pdf`

[22] Stabilized electro-optical airborne instrumentation platform (SEAIP), technical brief. Southern Research Institution, 2006.
Available at: `https://www.sri.org/pdf/electro_optical.pdf`

[23] iMAR web page: `http://www.imar-navigation.de/englishside/imar.htm`. 2005.

[24] Floatograph web page: `http://www.floatograph.com`. 2005.

[25] Paravion web page: `http://www.paravion.com/products/ev-275-2/ev-275-2.htm`. 2004.

[26] Educational control products web page: `http://www.ecpsystems.com`. 2005.

Appendix A

Gyroscope Design

The design drawings of the three-degree-of-freedom gyroscope is shown in figures A.1 (left view) and A.2 (front and top views). The structure consist of three gimbals, with a flywheel mounted on the inner gimbal. The inner gimbal forms the platform to be stabilised. Each gimbal adds a degree of rotational freedom to allow the platform to manoeuvre in roll, pitch and yaw. Each gimbal is connected to the previous gimbal through a DC motor, which supply the torques for platform steering. In addition, a potentiometer is mounted to each gimbal to measure the gimbal angles. Without electronics and wires, the outer gimbal can rotate through 360° continuously for azimuth platform steering. The middle and inner gimbals can both rotate ±55° in platform roll and pitch. With electronics and wiring, the outer gimbal is restricted to ±165° of rotation and the inner gimbal to ±25°. The center of mass of each gimbal coincide with the center of mass of the flywheel, to eliminate disturbance torques due to gravity.

A.1 Gimbal Moment of Inertia Measurements

The moments of inertia for each gimbal was measured by applying a torque to the gimbal and measuring the resulting angular displacement which, after differentiating twice, gives the angular acceleration. The inertia about the axis of rotation can then be calculated by Newton's second law, $N = J_n\alpha$, where N is the applied torque, α is the angular acceleration of the gimbal and J_n is the moment of inertia. The torque is calculated as

$$N = k_m I, \tag{A.1}$$

where k_m is the current constant of the motor and I is the current through the motor.

The measured moment of inertia of each gimbal about its axis of rotation is given in Table A.1. The value given is taken as the average of three consecutive measurements. It should be noted that the measurements were influenced by the wires between the gimbals and were only used as a starting point to determine the parameters used in the model.

Table A.1: Physical properties of gimbals

Gimbal	Moment of Inertia $[\frac{kg}{m^2}]$
Outer (3)	1.39691×10^{-2}
Middle (2)	7.475×10^{-3}
Inner (1)	6.441×10^{-3}

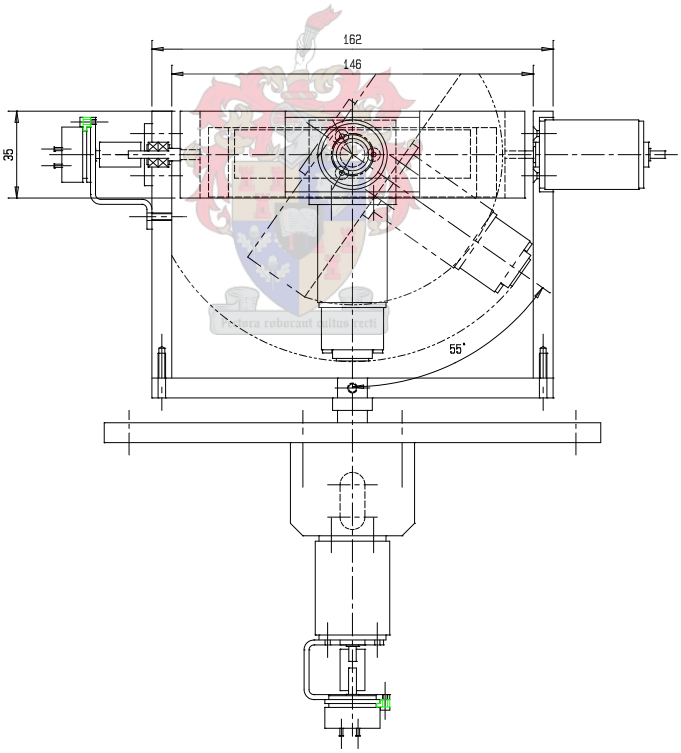

Figure A.1: Three-degree-of-freedom gyroscope design drawing, left view

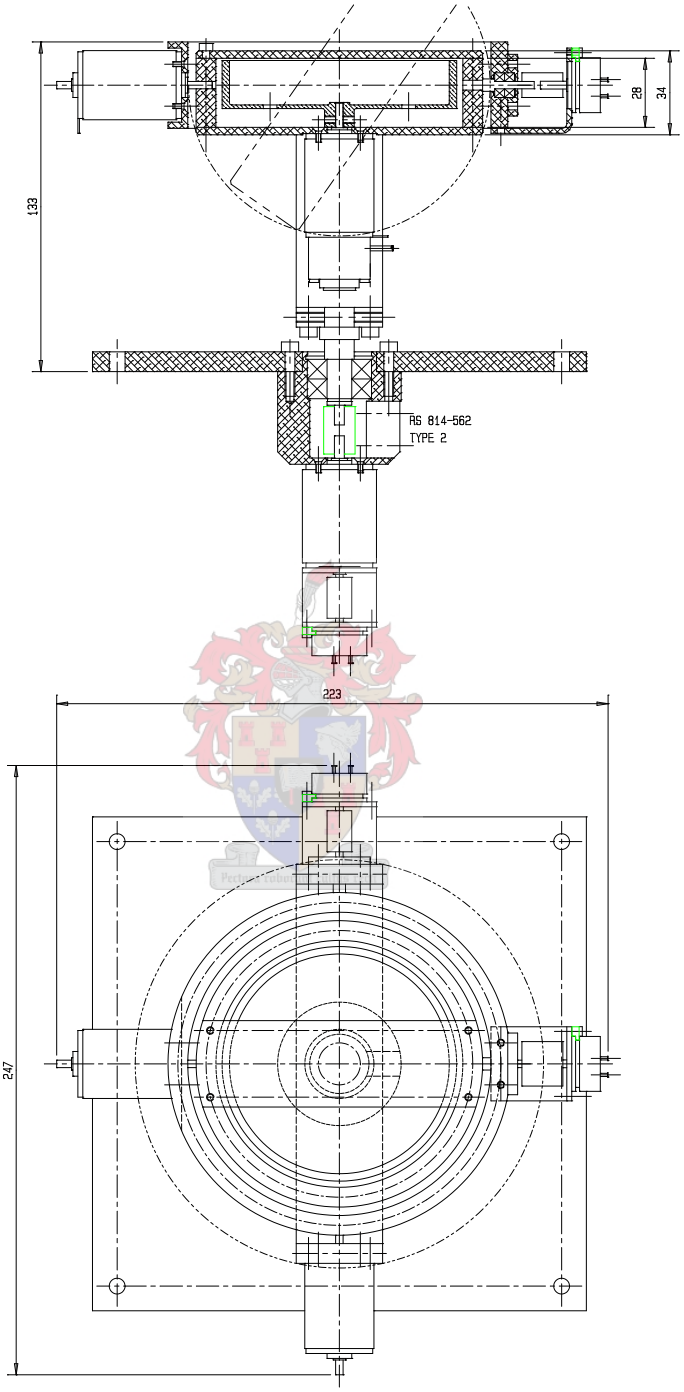

Figure A.2: Three-degree-of-freedom gyroscope design drawing, front and top views

Appendix B

PI Controller Analogue Implementation

Considering the control system of Fig. B.1, the summation block and controller with transfer function

$$H(s) = K_P\left(\frac{s + \frac{K_I}{K_P}}{s}\right) \tag{B.1}$$

can be realised with the analogue circuit illustrated in Fig. B.2.

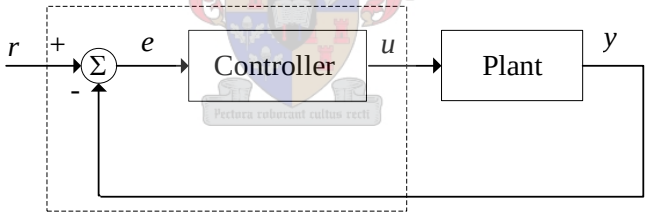

Figure B.1: A controller and plant feedback system

Combining R_2 and C to form Z_2 and realising that the resulting circuit resembles a difference amplifier [4], the output voltage V_u can be written in terms of the reference voltage V_r as

$$V_u = \left(1 + \frac{Z_2}{R_1}\right)\left(\frac{Z_2}{R_1 + Z_2}\right)V_r. \tag{B.2}$$

Substituting Z_2 with $(\frac{1}{sC} + R_2)$ in Eq. (B.2), where $\frac{1}{sC}$ is the Laplace transform of the capacitor, and simplifying, gives

$$\frac{V_y}{V_r} = \frac{R_2}{R_1}\left(\frac{s + \frac{1}{CR_2}}{s}\right). \tag{B.3}$$

Substituting

$$K_P = \frac{R_2}{R_1} \tag{B.4}$$

and

$$\frac{K_I}{K_P} = \frac{1}{CR_2} \tag{B.5}$$

in Eq. (B.3), yield Eq. (B.1), which is the transfer function of the PI controller.

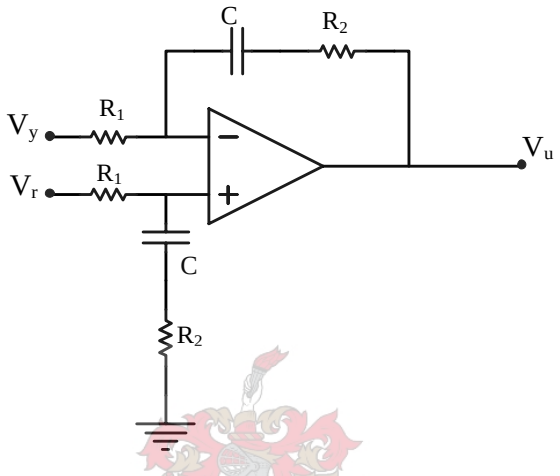

Figure B.2: Analogue implementation of PI controller

Appendix C

Hardware Detail

This chapter details the design of the electronic hardware developed for the stabilised platform. A photo of the electronics stack is shown in Fig. C.1. The IMU, with its signal conditioning electronics is situated on the top stack. The middle stack hosts the servodrive electronics. The electronic layout was designed to fit on the Cygnal C8051F020 development board, situated at the bottom. The IMU and servodrive electronics interface with the microcontroller through a 96-pin expansion connector.

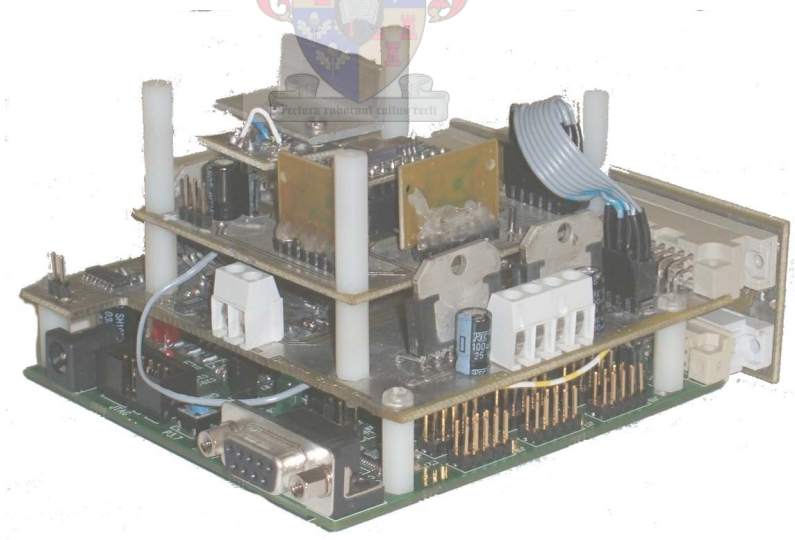

Figure C.1: Electronics developed for the stabilised platform

C.1 Motor Drives

Fig. C.2 shows the circuit diagram of the servodrives and torque and speed control systems. The servodrive components and analogue control systems are detailed in the following sections.

C.1.1 LMD18200

The LMD18200 can be operated in one of two modes, Locked Anti-phase Control (amplitude and direction of motor current is encoded in the PWM signal) or Sign/Magnitude Control (only amplitude of motor current is encoded in the PWM signal). The latter is implimented because better resolution in the commanded output torque can be obtained. The LMD18200 has three input pins, a brake pin, a direction pin and a PWM input pin. The microcontroller provides the brake and direction signals while the UC3524A chip provides the PWM signal.

The maximum voltage that can be commanded by the microcontroller is 3.3 V. Designing for currents of up to 0.5 A for motors 1 and 2 and to 0.86 A for motor 3, the current sense resistors are calculated using Eq. (3.1) with $I = \frac{N}{k_m}$, as

$$\begin{aligned} R_{sense1} = R_{sense2} &= \frac{3}{0.5 \cdot 377 \times 10^{-6}} = 15.915\text{k}\Omega \\ R_{sense3} &= \frac{3}{0.86 \cdot 377 \times 10^{-6}} = 9.253\text{k}\Omega \end{aligned} \tag{C.1}$$

C.1.2 UC3524A

The UC3524A chip is used to generate the PWM signal. The PWM duty cycle is proportional to the voltage applied to pin 9. The output is generated by two transistors, each capable of deliviring half cycle duty cycles up to 50 %. The output of each transistor are tied together to obtain a PWM signal with a duty cycle that can vary from 0 % to 100 %. The PWM signal is inverted before used as an input to the H-bridge.

The frequency of the PWM signal is determined by an external resistor and capacitor to ground at pin 6 and pin 7 respectively. The frequency was chosen as 30 kHz. Using the design equation

$$f_{osc} \approx \frac{1}{R_T C_T}, \tag{C.2}$$

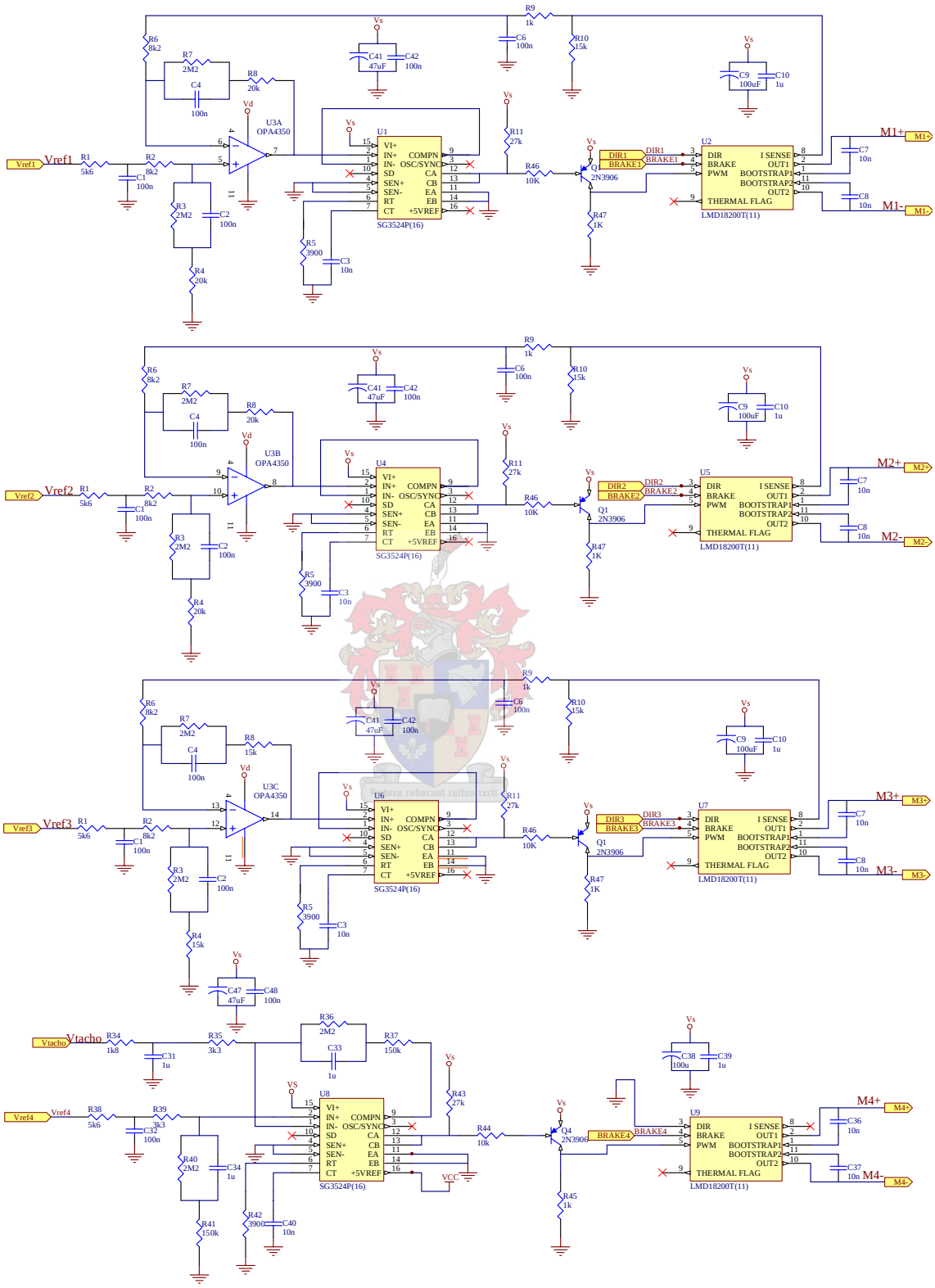

Figure C.2: Schematic diagram of servodrives.

the values of C_T and R_T were selected as

$$\begin{aligned} C_T &= 10\text{nF} \\ R_T &= 3300\Omega. \end{aligned}$$

The UC3524A has an onchip error amp, which was used as the op-amp for the analogue PI controller in the speed control loop of the flywheel. The limited common mode input voltage range of the error amp forced the use of external op-amps in the implementation of the PI controllers for the torque control loops, where the error amps were used as buffers.

C.1.3 Analoque Controllers

Gimbal Motor 1 and 2

To impliment the transfer fuction of Eq. (3.9), the values of the resistors and capacitors of Eq. (B.3) were chosen as

$$\begin{aligned} R_1 &= 8200\Omega \\ R_2 &= 20000\Omega \\ C &= 100\text{nF}. \end{aligned} \tag{C.3}$$

Gimbal Motor 3

To impliment the transfer fuction of Eq. (3.10), the values of the resistors and capacitors of Eq. (B.3) were chosen as

$$\begin{aligned} R_1 &= 8200\Omega \\ R_2 &= 15000\Omega \\ C &= 100\text{nF}. \end{aligned} \tag{C.4}$$

Flywheel

To implement the transfer fuction of Eq. (3.14), the values of the resistors and capacitors of Eq. (B.3) were chosen as

$$\begin{aligned} R_1 &= 3300\Omega \\ R_2 &= 150000\Omega \\ C &= 1\text{uF}. \end{aligned} \tag{C.5}$$

C.2 Potentiometers

Fig. C.3 illustrates the circuit diagram of the potentiometer as an angle sensor. The output voltage of each potensiometer, by voltage division, is

$$\begin{aligned} V_o &= \frac{2.4 \times R_-}{R_+ + R_-} \\ &= 0.00024 R_-. \end{aligned} \tag{C.6}$$

The ouput is filtered by a second order Butterworth low-pass filter [5], illustrated in Fig. C.4. The transfer function of the normalised filter is

$$\begin{aligned} H_B = \frac{V_o}{V_i} &= \frac{1}{s^2 + \sqrt{2} + 1} \\ &= \frac{\frac{1}{R^2 C_1 C_2}}{s^2 + \frac{2}{RC_1} s + \frac{1}{R^2 C_1 C_2}}. \end{aligned} \tag{C.7}$$

The cut-off frequency of 25 Hz is realised with the following component values:

$$\begin{aligned} C_1 &= 0.9 \times 10^{-6} \\ C_2 &= 0.45 \times 10^{-6} \\ R &= 10000. \end{aligned}$$

The implemented values are $C_1 = 1\mu\text{F}$, $C_2 = 0.47\mu\text{F}$ and $R = 10\text{k}\Omega$.

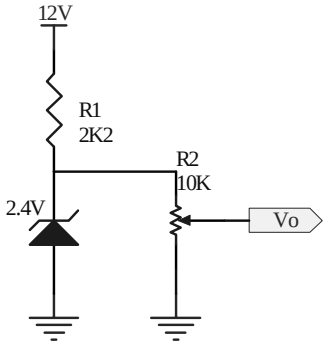

Figure C.3: Schematic diagram of potensiometers

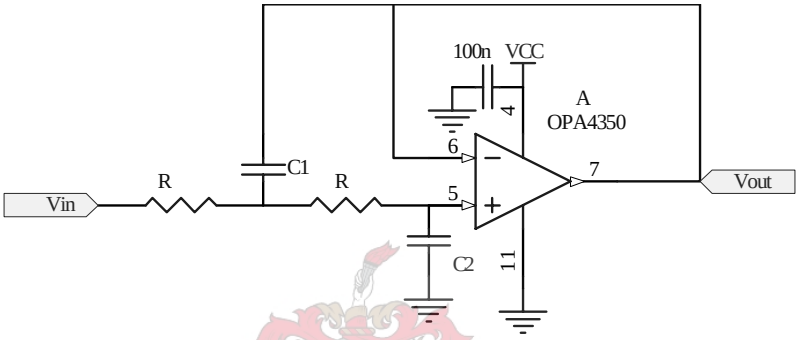

Figure C.4: Schematic diagram of second-order low-pass Butterworth filter circuit

C.3 Inertial Measurement Unit

The schematic diagram of the IMU is illustrated in Fig. C.5. Each IMU output signal is buffered before adjusted from a 2.5 V bias to a 1.2 V bias and low-pass filtered (25 Hz cut-off) with similar Butterworth filters as in Fig. C.4.

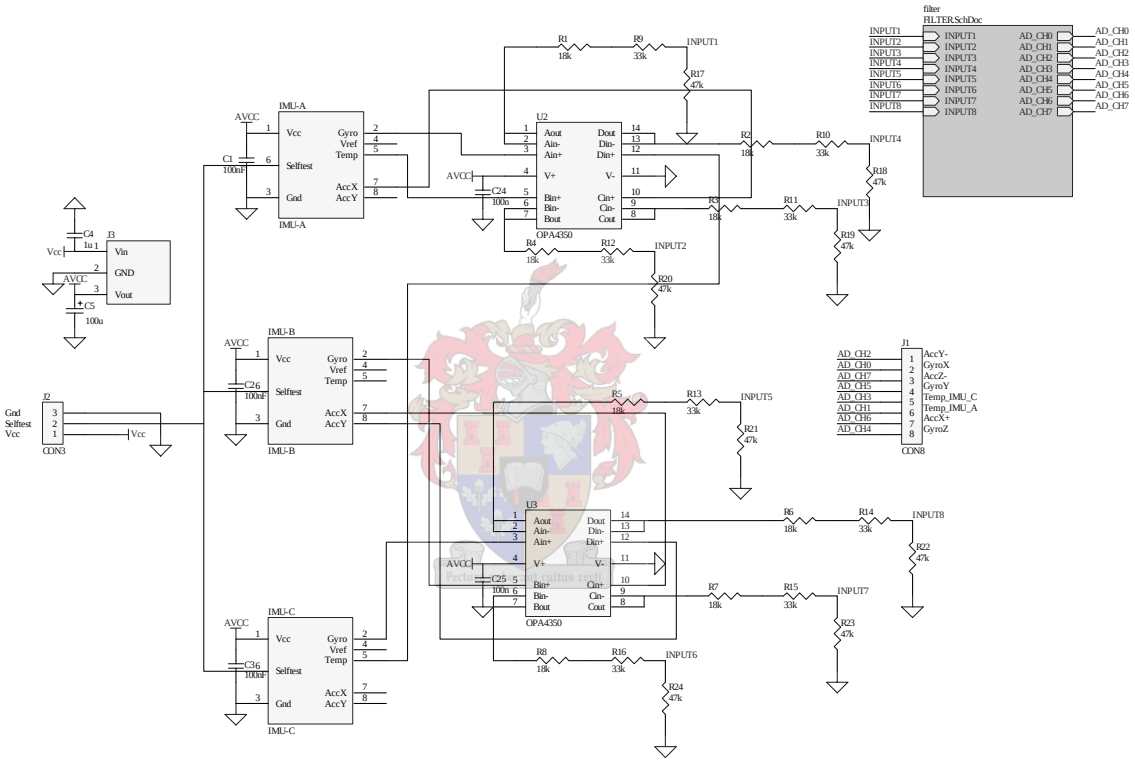

Figure C.5: Schematic diagram of IMU